TABLE DES MATIERES

1. SCOPE

This document is part of the TN3 submitted in fulfilment of WP 2120 of the Next Generation Gravity Mission (NGGM) study. Its purpose is:

- to review the state-of-art of the measurement technologies involved in the reference observing techniques of the NGGM and recommended the most appropriate technologies;
- to define acceleration sensor concepts potentially capable to meet the performance requirements;
- to compare the various acceleration sensor concepts and make recommendations on the reference acceleration sensor concept for the NGGM;
- to outline the calibration approach of the recommended reference acceleration sensor concept;
- to give the mathematical formulation of the performance of the acceleration sensor measurement.

2. APPLICABLE AND REFERENCE DOCUMENT

2.1. Applicable document

[AD1]	Assessment of a Next Generation Gravity Mission for monitoring the variations of earth's gravity field - TN3 instrument concepts, Thales Alenia Report, SD-TN-AI-1289, July 2010

2.2. Reference document

[RD1]	John Wahr, *Geodesy and Gravity*, Department of Physics, University of Colorado, Boulder, CO 80309
[RD2]	*Satellite Laser Ranging and Earth Science*, NASA Internal Laser Ranging Service. http://ilrs.gsfc.nasa.gov/docs/slrover.pdf. 2009-06-23
[RD3]	C.N. Man, *Journées Scientifiques de l'OCA- Virgo*, ARTEMIS UMR6162, CNRS OCA (Nice)
[RD4]	*Iliade à l'OCA* : http://www-g.oca.eu/iliade/ 1.5 micron, f_{rep}=100 Mhz, pulse=100 fs (frequency combs)
[RD5]	Mueller & Zerbini, *The Interdisciplinary Role of Space Geodesy*, Lunar ranging 3.10-12 (1989), Springer-Verlag Berlin
[RD6]	*Measurement Requirements Flowdown Guide*, Laser Interferometer Space Antenna (LISA)
[RD7]	*LISA, Laser Interferometer Space Antenna for the detection and observation of gravitational waves*, Pre-Phase A Report, Second Edition, July 1998
[RD8]	Peter de Groot and Stanley Kishner, *Synthetic wavelength stabilization for two-color laser-diode interferometry*, Applied Optics, **30** (1991), 28, 4026-4033
[RD9]	Y. Salvadé, *Distance measurement by multiple-wavelength interferometry*, Thèse de doctorat, Université de Neuchâtel, Institut de Microtechnique (1999)
[RD10]	R. Dändliker, R. Thalmann, D. Prongué, *Two-wavelength laser interferometry using superheterodyne detection*, Optics Letters, **13** (1988) 5, 339-341
[RD11]	B. Pécheux, *Optimisation d'un dispositif interférométrique de mesure de distance absolue utilisant une diode laser à cavité externe continûment syntonisable dans les bandes S et C*, Thèse de

	doctorat, Optronique et Systèmes, Strasbourg, Université Louis Pasteur (2002)
[RD12]	KOHERAS-NKT laser http://www.nktphotonics.com/Products
[RD13]	INNOLIGHT laser http://www.innolight.de/docs/scientific_lasers_all_products.html
[RD14]	*Développement d'une source laser pour senseur interférométrique de portée kilométrique*, ONERA study for CNES in the frame of 'Vol en Formation' program. R&T R-S05/VF-0001-022, (2006)
[RD15]	O. Turazza1 and al, *Towards an ultrastable Nd:YAG laser for space applications*, GPhyS conference, LesHouches (2009)
[RD16]	I Clifford, C. Hodge, Hugh A. Klein, David J.E. Knight and Lute Maleki, *Ultra-stable optical frequencies for space*, Joint Meeting EFTF - IEEE IFCS (1999)
[RD17]	T. W. Hänsch and al., *Subhertz linewidth diode lasers by stabilization to vibrationally and thermally compensated ultralow-expansion glass Fabry-Pérot cavities*, PRA **77** (2008) 053809
[RD18]	*Toptica laser locking*, AP_1012_laser_locking_2009_09.pdf on http://www.toptica.com
[RD19]	*Q-Flex® QA-3000 Accelerometer*, Datasheet Honeywell
[RD20]	Iafolla and al, *Italian Spring Accelerometer (ISA): A fundamental support to BepiColombo Radio Science Experiments*, Planetary and Space Science **58** (2010) 300-308
[RD21]	Iafolla and Nozzoli, *Italian spring accelerometer (ISA) a high sensitive accelerometer for "BepiColombo" ESA CORNERSTONE*, Planetary and Space Science **49** (2001) 1609-1617
[RD22]	Iafolla and al, *ISA accelerometer onboard the Mercury Planetary Orbiter: error budget*, Celestial Mech Dyn Astr **97** (2007):165–187
[RD23]	Iafolla, *ISA, an accelerometer to measure the inertial acceleration acting on MPO*, 3rd Bepi-Colombo Science Working Team Meeting, Padova, 26-28/09/2006
[RD24]	Le Traon and al, *The VIA vibrating beam accelerometer – Concept and performance*, ONERA TP-1998-44, Proceedings of PLAN'S 1998, Palm Springs (1998)
[RD25]	Le Traon and al, *The VIA vibrating beam accelerometer – A new quartz micro-machined sensor*, Joint Meeting EFTF – IEEE IFCS (1999)
[RD26]	Le Traon and al, *Preliminary results about GaPO4 vibrating inertial sensors*, J. Phys. IV France **126** (2005) 123–126
[RD27]	Lepage and al, *Thermoelastic damping in vibrating beam accelerometer: a new thermoelastic finite element approach*, Proceedings of CANEUS, Toulouse (2006)
[RD28]	Le Traon and al, *LGS and GaPO4 piezoelectric crystals: New results*, Solid State Sciences **12** (2010) 318–324
[RD29]	Le Traon and al, *Monolithic accelerometric Transducer*, US Patent 5,962,786 (1999)
[RD30]	Touboul and al, *In-orbit nano-g measurements, lessons for future space mission*, Aerospace Science and Technology **8** (2004) 431–441
[RD31]	Marque and al, *6 ultra-sensitive accelerometers for the GOCE mission*, Proceedings of IAC (2004)
[RD32]	Marque and al, *The Ultra-sensitive accelerometers of the ESA GOCE mission*, Proceedings of IAC, Glasgow (2008)
[RD33]	Christophe and al, *Accelerometers for the ESA GOCE Mission: one year of in-orbit results*, slides presented at EGU, Vienna (2010), available on ESA/GOCE website
[RD34]	Christophe and al, *Odyssey: a solar system mission*, Exp Astron **23** (2009):529–547
[RD35]	Christophe and al, *Gravity Advanced Package, an Accelerometer Package for Laplace or Tandem Missions*, Proceedings of SF2A (2008)
[RD36]	Sehnal and al, *MIMOSA—A satellite measuring orbital and attitudinal accelerations caused by non-gravitational forces*, Advances in Space Research, **23**, Issue 4 (1999) 705-714

[RD37]	Peresty, *MIMOSA satellite*, Acta Astronautica, **46** (2000) 345-349
[RD38]	Sehnal and al, *Dynamical Microaccelerometric Measurements on Board Space Shuttle*, Acta Astronautica **47**, No. 1 (2000) 27-34
[RD39]	Sehnal and al, *Space Project MIMOSA*, Publ. Astron. Obs. Belgrade No. 75 (2003), 195-208
[RD40]	*Swarm - The Earth's Magnetic Field and Environment Explorers Technical and Programmatic Annex*, Annex to ESA SP-1279(6) April 2004
[RD41]	MIMOSA, EO Portal http://www.eoportal.org/directory/pres_MIMOSAMicroaccelerometricMeasurementsofSatelliteAccelerations.html
[RD42]	*Three axial Accelerometer for SWARM*, 2nd ESA SWARM Science Meeting (2009)
[RD43]	Petrucha and al, *Tester for space micro-accelerometer*, Procedia Chemistry **1** (2009) 1 6 4 –167
[RD44]	Bortoluzzi and al, *Object injection in geodesic conditions: In-flight and on-ground testing issues*, Advances in Space Research **45** (2010) 1358–1379
[RD45]	Berger, *LISA Mission Formulation - Payload Preliminary Design Description*, EADS Astrium, LISA-ASD-DD-3001, July 2008
[RD46]	Vitale and al, *Science Requirements and Top-level Architecture Definition for the Lisa Technology Package (LTP) on Board LISA Pathfinder (SMART-2)*, LTPA-UTN-ScRD-Iss003-Rev1, June 2005
[RD47]	Jennrich, *LISA Technology and Instrumentation*, Class. Quantum Grav. **26** (2009)15 3001
[RD48]	Vitale and al, *LISA Pathfinder: Einstein's Geodesic Explorer - The Science Case for LISA Pathfinder*, ESA-SCI(2007)1
[RD49]	Mc Namara, Introduction to LISA Pathfinder, ESA report LISA-LPF-RP-0002, Issue 1.1 (2009)
[RD50]	Vitale and al, *The LISA Technology Package on board SMART-2*, Report Trento University n°Unitn-Int 10-2002/Rel. 1.3 (2002)

3. TOP-LEVEL MEASUREMENT REQUIREMENTS

The following requirements come from the system analysis deduced from the science requirements defined in [AD1].

3.1. Satellite-to-Satellite Distance Measurement Requirement

The requirement on the satellite-to-satellite distance measurement error spectral density can be therefore expressed in function of frequency as (see also Figure 1):

$$\delta\tilde{d}(f) < \begin{cases} 20\cdot 10^{-9} & \text{for } f \geq 0.01\,\text{Hz} \\ 20\cdot 10^{-9}\cdot\left(\dfrac{0.01}{f}\right) & \text{for } f < 0.01\,\text{Hz} \end{cases} \quad \frac{\text{m}}{\sqrt{\text{Hz}}} \qquad (3.2.1)$$

The requirement applies to a satellite-to-satellite distance d included between 50 km and 100 km.

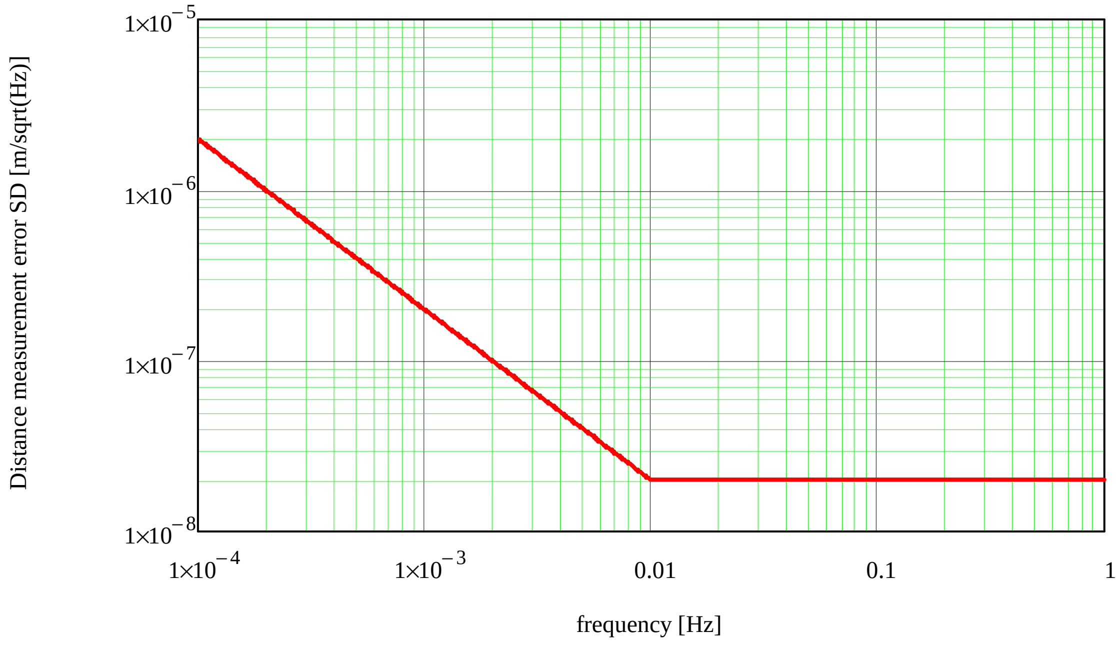

Figure 1: Upper limit to the measurement error spectral density of the satellite-to-satellite distance (applicable to a relative distance between 50 km and 100 km).

3.2. Non-Gravitational Acceleration Measurement Requirement

The accelerometers are used from one part for the measurement of the non-gravitational accelerations (or its residual in case of drag free), and for other part for the measurement of the angular acceleration for the attitude control of the spacecraft. This angular acceleration could be deduced either from the linear acceleration measurement of two accelerometers, either directly by the angular acceleration measurement of one accelerometer.

3.2.1. Accelerometer noise

The accelerometer noise specification (is more severe along the in-track axis, X (satellite to satellite line of view) than on the two other axes, Y (cross-track) and Z (radial).

$$\tilde{n}_{i,\mathrm{X}} \le \begin{cases} 3\cdot 10^{-12} & \text{for } f \ge 0.001 \text{ and } f \le 0.01\,\mathrm{Hz} \\ 3\cdot 10^{-12}\cdot\left(\dfrac{0.001}{f}\right)^2 & \text{for } f < 0.001\,\mathrm{Hz} \\ 3\cdot 10^{-12}\cdot\left(\dfrac{f}{0.01}\right)^2 & \text{for } f > 0.01\,\mathrm{Hz} \end{cases} \quad \frac{\mathrm{m}}{\mathrm{s}^2\sqrt{\mathrm{Hz}}} \qquad \tilde{n}_{i,\mathrm{Y,Z}} \le \begin{cases} 10^{-10} & \text{for } f \ge 0.001 \text{ and } f \le 0.01\,\mathrm{Hz} \\ 10^{-10}\cdot\left(\dfrac{0.001}{f}\right)^2 & \text{for } f < 0.001\,\mathrm{Hz} \\ 10^{-10}\cdot\left(\dfrac{f}{0.01}\right)^2 & \text{for } f > 0.01\,\mathrm{Hz} \end{cases} \quad \frac{\mathrm{m}}{\mathrm{s}^2\sqrt{\mathrm{Hz}}}$$

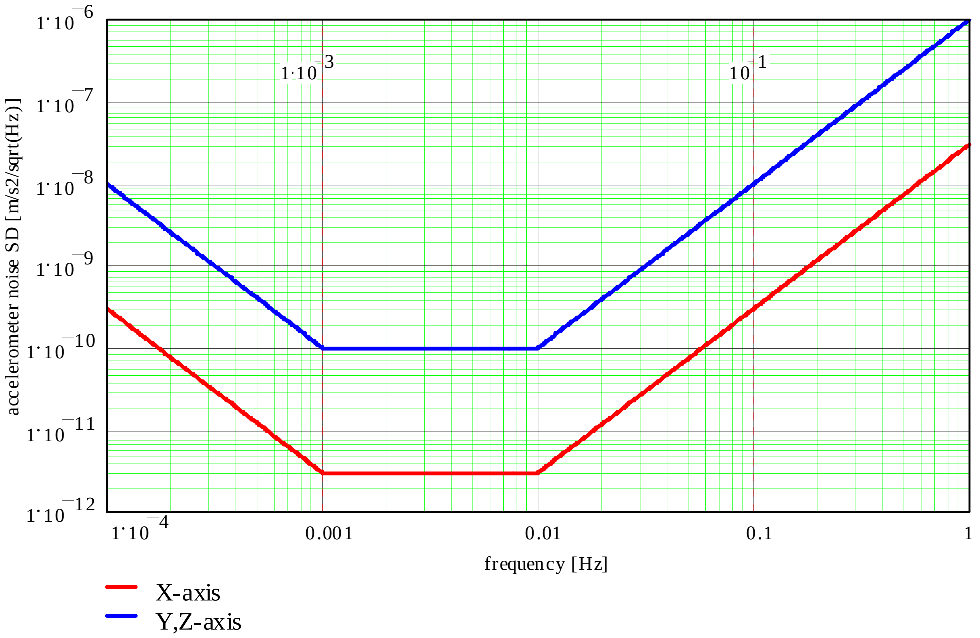

Figure 2: Level of noise along X and along Y and Z for the accelerometer

3.2.2. Accelerometer bias and scale factor

Specifications are also given for the bias level along the cross-track and radial axes and for the scale factor stability (Figure 3), with the same accuracy over the 3 axes.

- bias $b_{i,\mathrm{Y}}$, $b_{i,\mathrm{Z}} < 2\cdot 10^{-7}$ m/s^2
- scale factor stability: $$\tilde{K}_{i,\mathrm{X,Y,Z}} \leq \begin{cases} 10^{-6} \text{ for } \ f \geq 0.001 \ \text{ and } \ f \leq 0.01 \text{ Hz} \\ 10^{-6} \cdot \left(\dfrac{0.001}{f}\right)^2 \quad \text{for } \ f < 0.001 \text{ Hz} \\ 10^{-6} \cdot \left(\dfrac{f}{0.01}\right)^2 \quad \text{for } \ f > 0.01 \text{ Hz} \end{cases} \quad \frac{1}{\sqrt{Hz}}$$

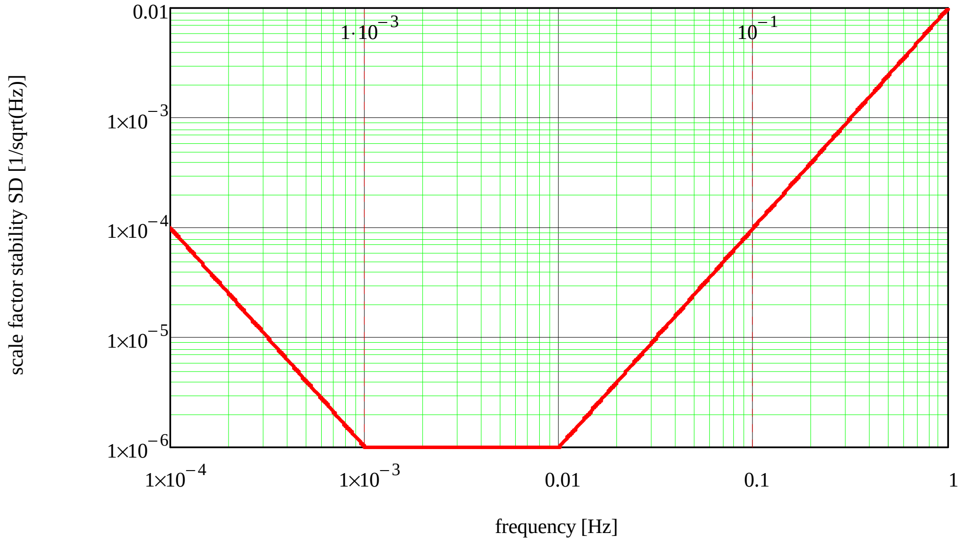

Figure 3: Level of noise for the scale factor of the accelerometer

3.2.3. Angular acceleration

The accelerometer shall help for the reconstruction of spacecraft attitude, in complement of the star tracker. The angular acceleration can be measured either from the differential linear acceleration measurement of two accelerometers, either directly by the outputs of one accelerometer corresponding to the control of the proof-mass angular motion. A preliminary requirements on the accelerometer intrinsic noise for the measurement of the angular acceleration around the Y axis was given in Figure 4. It is supposed that there is the same requirement for the 2 other axes.

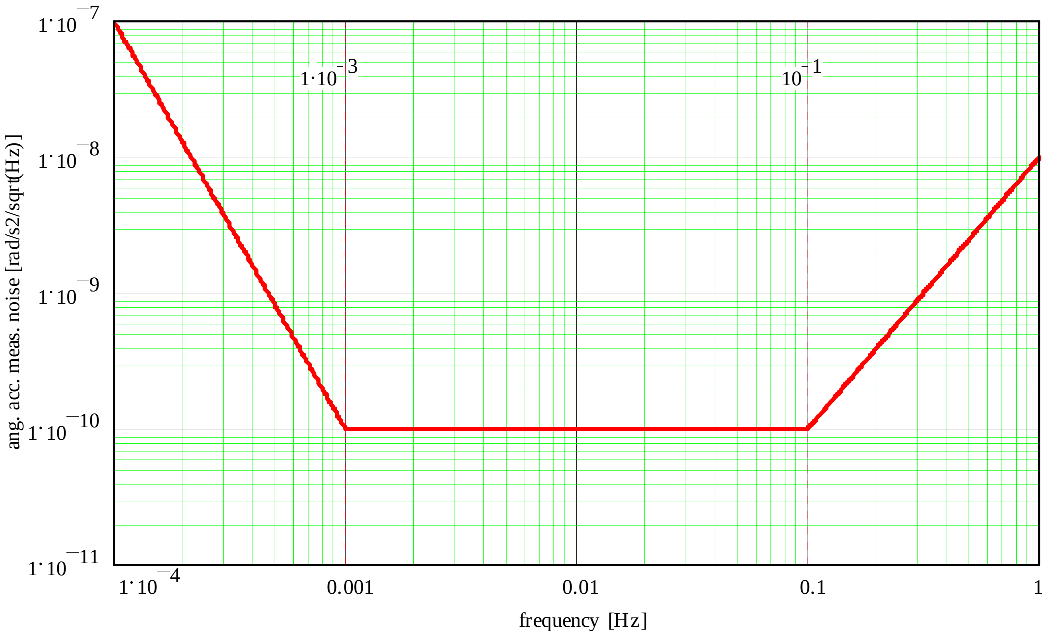

Figure 4: Requirement of the angular acceleration noise around Y axis

4. REVIEW AND RECOMMENDATION OF THE MEASUREMENT TECHNOLOGIES

4.1. Distance Optical Metrology Technologies Review

4.1.1. Introduction

This chapter will briefly review and analyse the state of the art concerning laser ranging for long distance measurement. For an absolute (or relative) distance determination, the absolute (or relative) stability of the laser used in these techniques is the major key element. Some usual techniques which fulfil requirement are presented.

Technologies for distance-measuring instruments have been constantly developed after the Second World War. Old tapes have been replaced by instruments which send and receive electro-magnetic radiation (microwave or more usually light). In these cases, the ruler for the measurement could be:

- a defined pattern of the beam (for instance: temporal intensity modulation for time of flight measurement) or
- directly the wavelength of the used radiation.

The method is quite simple: the source shines a continuous beam of radiation toward a target, and the reflected (or diffused) beam comes back to the source and is compared with the initial emission using time-counter or interference techniques.

For interferometer methods, the phase difference ϕ tells you something about twice the distance L, you want to measure:

$$\phi = \frac{2\pi}{\lambda} 2 \cdot L \cdot n$$

with λ the wavelength of the laser, and n the refractive index of the propagation medium.

And the measured intensity signal S received by the detector is simply related with ϕ by

$$S = \frac{S_0}{2}\left(1 + C\sin(\phi)\right),$$

with C a parameter called contrast.

The sinusoidal relation produces fringes and leads to a 2π ambiguity on measurement, if the phase (and/or the distance L) must be retrieved. The ambiguity can be overcome, if something in the experiment is modulated (often the wavelength).

In general, for a simple scheme (Figure 5), the distance resolution is related to the wavelength λ and the signal to noise ratio N:

$$\delta L = \frac{\lambda}{2N}$$

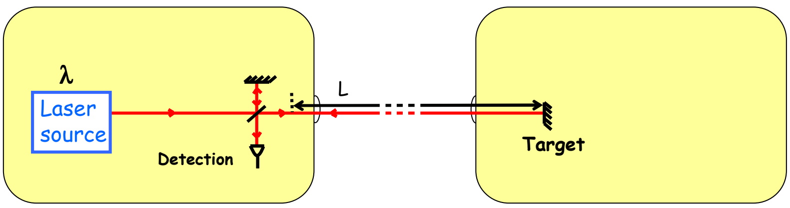

Figure 5: simple Michelson interferometer scheme for distance measurement, the incident laser light is reflected toward the source and then mixed. The measured intensity on a detector depends on L.

As reported in (3.2.1), goals to achieve are in the range of 2.10^{-8} m/Hz$^{1/2}$ for distance in the range of 50 to 100 km. That is equivalent to a relative very good stability of about 10^{-13} /Hz$^{1/2}$. Only high resolution method compatible with this requirement will be further described in details.

4.1.2. Radio/Microwave vs Laser measurements

In telemetry system, the current tendency is to change microwaves by optical frequency (RADAR to LIDAR). Advantages are numerous but for an increased complexity due to the utilization of optical sources and laser beams. For optical source, the electrical emission efficiency is much lower, and the electrical cost is higher.

The optical carrier frequency is much higher (10^{14}~10^{15} Hz compared to 10^{6}~10^{10} Hz) and will permits better resolution because:

- A large bandwidth and high modulation rate can be obtained: the carrier frequency is higher and allows a bandwidth which can be in the range of 10^{10}~10^{12} Hz.
- The resolution is intrinsically better, because de wavelength is much smaller: $\delta L = \lambda/2N$. With typical N>10^3, λ~1μm, sub nanometre can theoretically be achieved for δL.
- The propagation of light is more immune to the environment: in space n=1 is a well verified approximation. On the contrary, microwave interacts a lot with solar plasmas, ionized medium, and ionosphere.
- The directivity of the beam is increased for a the same 'antenna size' of D : $\theta \approx \lambda/D$,
- Some fundamental thermal limitation will be reduced because of the higher energy transported by one photon $hc/\lambda \approx 10^{-19} \rangle\rangle k_B T \approx 10^{-21}$

For resolution $\delta L/L$ not better than 10^{-10}, the microwave solution is well adapted because of the simplicity (GRACE: 10^{-4} m/√Hz at 0.1 Hz …). But for high demanding application, like here, the laser solution seems to be needed.

Often, both system are complementary, the microwave ranging technique is used as a first stage to measure or stabilized roughly the distance and/or the orientation. And the laser is in a second stage and deals with the high resolution. It should be also noticed that microwave alone is also well adapted to other positioning technique (cf. GPS) or velocity measurement of a target using Doppler Effect ([RD1]).

4.1.3. Laser ranging and distance measurement

Laser distance measurement, can be based either on the use of continuous (CW) or pulsed laser to make either interferometer or Time of Flight (ToF) measurements.

ToF techniques and all derived methods (Phase shift, intensity modulation pattern, …) are using the fact that high correlation between incident and returned beams occurs for time delay corresponding with the transit time of laser between the two satellites : $\tau = 2 \cdot L \cdot n/c$. These techniques are employed in various domains: for short distance measurement in common portable system (laser distance meter), for long distance measurement (ex: LAGEOS with ToF technique leading to cm range measurement [RD2]), or for longer distance (like Lunar Laser Ranging at mm scale range with long scale integration [RD5]).

For interferometer measurements, various geometries and setups can be employed; majority of them are derived from Michelson interferometer. For improved performance, symmetry for common mode rejection is used to reject effect like polarisation, unbalanced power, long distance losses… The system can use two lasers to have redundancies and to increase the received. The reflector is usually a corner cube reflector to have a larger angular tolerance to misalignments. On earth or through the atmosphere the method is limited because of atmospheric instability. The key element in the system is the laser source, all instability of the laser source directly impact the performance of the overall system.

For instance, if the distance measurement is relative (just to follow variations of $\delta L(t)$, without a precise determination of the mean L), a relative stabilisation of the frequency of the laser is needed. If the measurement is absolute (distance L(t) need to be measured), the stabilisation of the laser must be absolute. Good laser performance is really the most difficult key point to obtain in this kind of metrology, because it always implies the use of non conventional laser with an increased complexity. Figure 6 illustrates roughly the order of magnitude of requirements for specified performance and technologies.

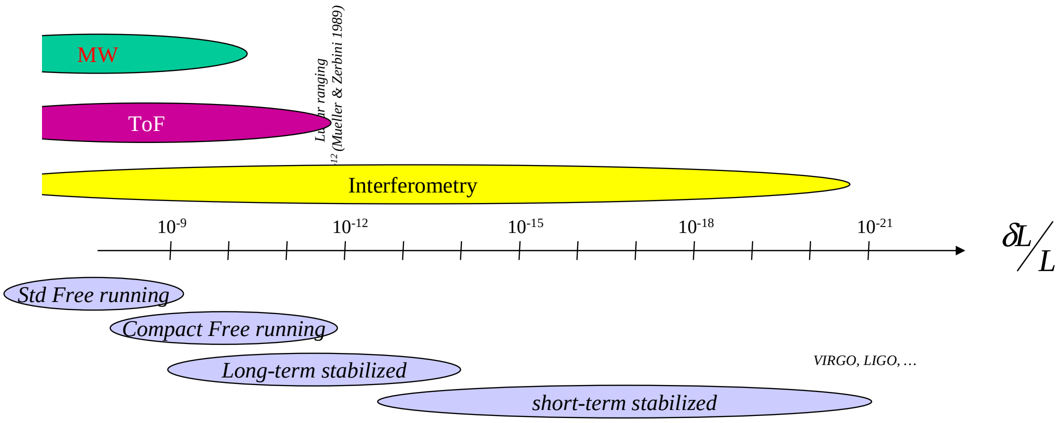

Figure 6: (up) technologies versus distance measurement performance: MW for microwave, ToF for Time of Flight. (bottom) laser technologies to achieved the required stability in abscissa [RD3].

Gravitational wave astronomy instruments (LISA, LIGO, VIRGO …) are based on the use of a gravitational wave detector which is composed of a very large Michelson interferometer. For these measurements, high stability lasers are also required. All the developments and researches made today around these ambitious projects could benefit for inter-satellite measurement in the 100 km range ([RD6], [RD7]).

4.1.4. Laser requirements for distance measurements

This part presents some general requirements for the laser system in order to achieve the performance (3.2.1). For numerical application, we fixed L=100 km, and λ_0=1 µm.

4.1.4.1. Quantum shot noise limit

The first fundamental limit concerning the laser is dealing the quantum limit. In a perfect world, without other technical limits, the minimum laser intensity fluctuation is determined by the measured photon number N_{ph} :

$$\frac{\delta S}{S} = \frac{1}{\sqrt{N_{ph}}}.$$

N_{ph} can be known from the input optical power P, the integrating time τ, and the optical transmission η of the transmission line:

$$N_{ph} = \tau . \frac{\eta P}{h \dfrac{c}{\lambda_0}} .$$

But sinusoidal evolution of S with the phase, gives $\delta\phi = \frac{1}{C}\frac{\delta S}{S}$ which is obtained for the maximum sensibility at ϕ near 0 [2π]:

$$\frac{\delta L}{L} = \frac{\delta\phi}{\phi} = \frac{\frac{1}{C}\frac{\delta S}{S}}{\phi} = \frac{\frac{1}{\sqrt{N}}}{\frac{2\pi}{\lambda_0} C 2L} .$$

For a Gaussian laser beam ([RD6]), the beam divergence caused by diffraction on optics of size D gives a first estimation of losses along the light line:

$$\eta = \eta_0 \frac{1}{8} \frac{D^4}{\lambda^2 L^2}$$

with η_0 transmission limited by others losses (for instance: detector quantum efficiency, absorption in optics, beam quality, …).

The power received is then ηP .

All previous relations lead to

$$\boxed{\frac{\delta L}{L} = \frac{\lambda_0^{3/2}}{C\pi D^2 \sqrt{\eta_0 P}} \frac{\sqrt{2hc}}{2} . \tau^{-1/2}}$$

The initial requirement (δL/L=2.10^{-13} Hz$^{-1/2}$) for reasonable value of the diameter of optics D=0.1m, transmission of $\eta_0 = 5\%$, contrast of C=0.5 and a power of P=1 mW seems to be largely respected.

4.1.4.2. Linewidth of the laser source

The contrast C in the interferometer will dramatically decreased if the coherence of the laser source is not good enough. This represents the fact that for a certain delay of time the laser, the delayed laser wave is not coherent with itself; and interference fringes disappear. In the case of the Michelson interferometer the phase difference will be huge: $\phi = \frac{2\pi}{\lambda} 2 \cdot L \cdot n$ because L corresponds to a long distance ~ 100 km.

With simple consideration, we can approximate the contrast with

$$C = \frac{\sin\left(\pi \frac{2L}{c} \Delta\nu\right)}{\pi \frac{2L}{c} \Delta\nu}$$

which depends of the linewidth of the laser Δν.

To keep a good contrast we absolutely need:

$$\boxed{\Delta\nu \langle\langle \frac{c}{2L} \approx 1500 Hz}$$

This last specification is not easy to obtain. Solid state laser with difficulties obtain this order of magnitude of linewidth. For example, fiber Er-DFB laser are naturally in this range around 1 kHz. External cavity diode laser can be narrowed with very efficient locking techniques (Pound-Drever-Hall for example [RD18]) in order to obtained linewidth below 10 kHz.

4.1.4.3. Laser wavelength stability

Due to the measurement relation $\phi = \frac{2\pi}{\lambda} 2 \cdot L \cdot n$, all laser wavelength fluctuations will limit the sensibility:

$$\boxed{\frac{\delta L}{L} = \frac{\delta \upsilon}{\upsilon}}.$$

The requirement in term of distance must be directly applied to the laser stability requirement.

For λ_0=1 µm, (3.2.1) relation is traduced to the following:

$$\delta\tilde{\upsilon}(f) < \begin{cases} 60 & \text{for } f \geq 0.01\,\text{Hz} \\ 60 \cdot \left(\frac{0.01}{f}\right) & \text{for } f < 0.01\,\text{Hz} \end{cases} \quad in\ \frac{\text{Hz}}{\sqrt{\text{Hz}}}$$

The level near 60 $Hz/Hz^{-1/2}$ must be achieved. This requirement is severe, and cannot be fulfilled with the use of standard or compact free-running laser. Their wavelength largely drift with time due to internal fluctuant parameters like temperature, acoustic noise, current, non-linearity, fundamental instability, internal noise, …

An active locking technique must be used to achieve this level. The laser is a resonator with a characteristic length. The output wavelength is related to this dimension. Controlling the laser wavelength is equivalent to control precisely the internal active length of the amplifier cavity inside the laser. This corresponds to the etalon of length that will be used for the measurement. To achieve that, an optical frequency reference is needed and will allow the synthesis of a locking error signal to retroact on the laser (Figure 7).

Usually, we can distinguish two kinds of locking timescale:

- For long timescale: an absolute spectroscopic reference can be used, narrow absorption lines can be observed with various molecular (C_2H_2, I_2 …) or atomic species (H, Cs, Rb …). Limitation due to line broadening (like Doppler effects, pressure, transit time, or saturation) could be overcome with particular setup or geometry (like 2-photons or saturated absorption). The major inconvenient is that references are not present on demand everywhere in the optical spectrum: the wavelength often must be chosen by a compromise between laser performance and available reference.
- For short timescale: a mechanical system is often used (Fabry-Perot cavities for instance). This will give a relative good short term reference of length. Due to thermal drift or aging effect, long term stabilization generally cannot be achieved above 1000 s.

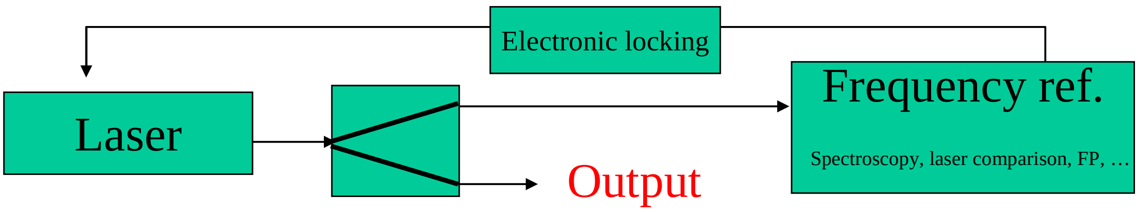

Figure 7: laser locking set-up to achieved wavelength control in order to enhance wavelength stability and/or exactitude.

<u>Remark</u>: The specification ($\delta L/L=\delta\nu/\nu$ =2.10^{-13} Hz$^{-1/2}$) gives also a linewidth specification. If we suppose lorentzian spectrum for the laser, we have $\delta\nu=2\pi S_\nu$, with S_ν the frequency power spectral density. That is giving for the linewidth $\delta\nu$ a specification around 6 kHz, which is less demanding than $\Delta\nu \langle\langle c/2L$ (see 4.1.4.2).

4.1.4.4. Laser power stability

Laser power instability will directly impact the Michelson signal:

$$\boxed{\delta L = \frac{\delta S}{S}\frac{\lambda_0}{4\pi C}},$$

that's corresponding to a signal to noise ratio

$$N = \frac{2\pi C}{\left(\frac{\delta S}{S}\right)}.$$

For λ_0=1 µm, and C=0.5; (3.2.1) relation is traduced to the following:

$$\frac{\delta\tilde{S}}{S}(f) < \begin{cases} 0.1 & \text{for } f \geq 0.01\,\text{Hz} \\ 0.1\cdot\left(\frac{0.01}{f}\right) & \text{for } f < 0.01\,\text{Hz} \end{cases} \quad \overline{\sqrt{\text{Hz}}}$$

This requirement seems to be obtained with either stable free-running laser (for short time scale) or with an appropriate intensity locking system (for long time scale).

4.1.4.5. For absolute distance measurement

Firstly, for an absolute distance measurement, the previous stability requirement for the laser is needed also for the absolute knowledge of the wavelength:

$$\frac{\Delta L}{L} = \frac{\Delta \upsilon}{\upsilon}.$$

And secondly, the 2π ambiguity must be solved using a modulation of 'something' in the instrument ([RD8],[RD9],[RD10],[RD11]). The laser wavelength can be often changed, modulated or swept over a range $\Delta\nu_{synth}$ as wide as possible to eliminate the ambiguity. Recorded interference fringes will be able to increase the length ambiguity to a level than can be completely eliminated by another system or by dimensional consideration.

4.1.5. Some Examples of laser

4.1.5.1. Free running laser

This kind of laser is commercially available for various purposes including telemetry. The wavelength is not locked on a reference, and is determined by the intrinsic stability of the laser cavity. They are either compact solid state laser (Nd:YVO4, Nd:YAG , …), fiber laser (Er, Yb, …), or directly laser diode (GaAs or derived and others semiconductors, …). We can mention well-known society like INNOLIGHT, KOHERAS NKT, IPG … ([RD12],[RD13])

Commercial product have high output power (~ 1W), for a moderate size (100 cm^3 for 1 kg), and with line width compatible for distance measurement of 1 km only. The stability of the wavelength is limited by a drift in the range of 1 MHz/min (Figure 8).

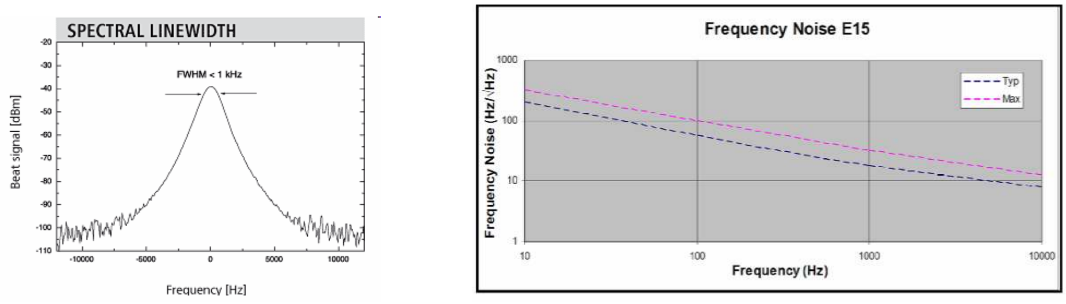

Figure 8: typical obtained linewith around 1 MHz (left) and wavelength stability (right) of an example of free running solid state Nd:Yag laser [RD13]

Femtosecond mode-locked (cf. frequency combs) could also be an interesting alternatives to make high resolution distance measurements. Nowadays, developments are under progress in various laboratories ([RD4]).

4.1.5.2. Compact laser with a spectroscopic reference

The wavelength stability of previous free-running laser is not enough good to allow high resolution measurement. These commercial lasers can often be stabilized on molecular transition to obtain performance near 2.10^{-13} in relative at 10^2 s (which is corresponding to requirement) and even better near $10^{-15}\ \tau^{-1/2}$ ([RD15]) (which is corresponding to LISA requirements), as shown in Figure 9.

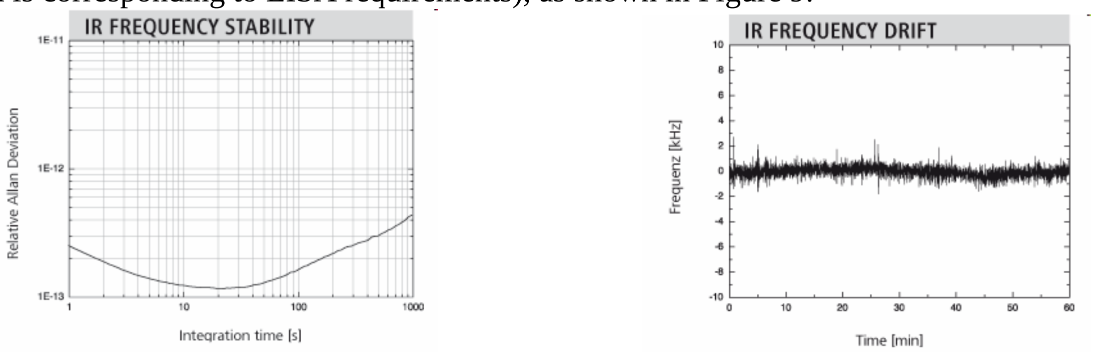

Figure 9: typical relative Allan deviation (left) and wavelength stability (right) of a sold state Nd:Yag laser locked on a Iodine transitions [RD13]

Unfortunately, these lasers seem to have too large linewidth (~ 1MHz). For a 100 km long distance to measure, that will induce a loss of contrast (C~ 10^{-4}) that is not compatible with requirements. The use of Er doped fiber DFB laser emitting at 1.5 µm have easily a narrow linewidth of few kHz. This laser can also be stabilized on an atomic transition to obtain good long term behaviour, as shown in Figure 10 ([RD14]).

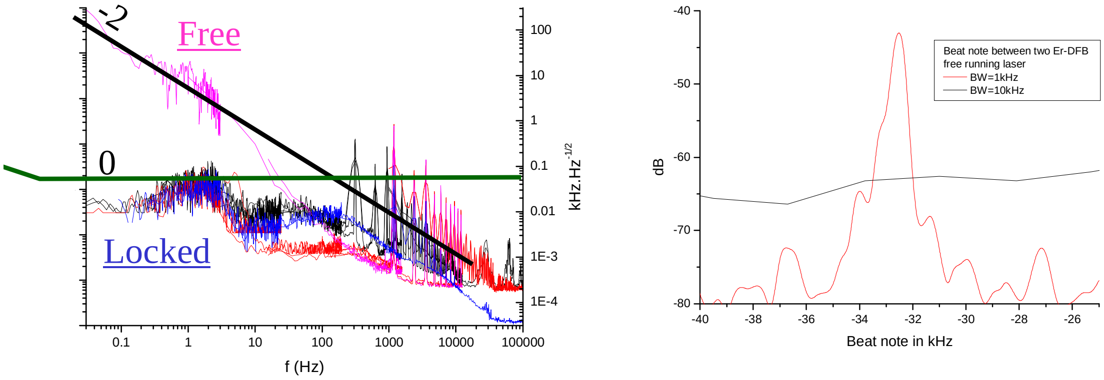

Figure 10: (left) example of wavelength stability of an Er-Doped DFB fiber laser locked on a Rb atomic line after a second harmonic generation stage, for various locking parameter (curves in blue, red, and black), compared with the same laser in a free-running mode (pink curve). Requirement (lines in green) is also printed on the graph as reference. [RD14]
(right) instantaneous beat note spectrum of two free running Er-Doped DFB fiber laser : few kHz linewidth is shown. [RD14]

4.1.6. Conclusion and synthesis

After a rapid analysis of the requirement for such a space mission, compared to the state of the art in the frame of distance measurement for long distance (L~100 km), we can conclude that :

- The laser linewidth is the key parameter to allow good contrast in fringes measurement $\Delta\nu \langle\langle c/2L$. Some lasers have naturally compatible linewidth (Er-Doped DFB, External Cavity diode laser, …) or others can be narrowed to fulfil requirement (Nd:Yag, diode laser, …) with advanced locking techniques like PDH ([RD17]).
- The long term goal frequency stability requires for sure a locking stage on a spectroscopic reference: $\delta\upsilon/\upsilon = \delta L/L$ (Iodine, Rubidium, others species could be used), this has an important impact on the laser system: complexity, volume/mass, reliability …
- Others parameters: high power, power stability, reduced size and mass is available with various technologies and system
- Space qualifications of theses kind of laser are, until now, not known by the author. Some works on this subject have been done concerning Nd:Yag systems ([RD16]).

4.2. Accelerometer Technology Review

4.2.1. Principle of accelerometer

The principle of accelerometer technology is a mass (often called proof-mass), in levitation with respect to a cage, rigidly fixed to the spacecraft. The motion of the proof-mass is “free” along at least one direction. Any acceleration applied to the spacecraft along this direction is seen by the accelerometer through the detection of the motion of the mass with respect to the cage, rigidly fixed to the spacecraft. Often the measurement of the external acceleration is deduced from a force applied on the proof-mass and not by the double integration of the proof-mass position: for example, in case of a proof-mass suspended by a spring, the position measurement of the proof-mass is translated into acceleration through the stiffness of the spring (see Figure 11).

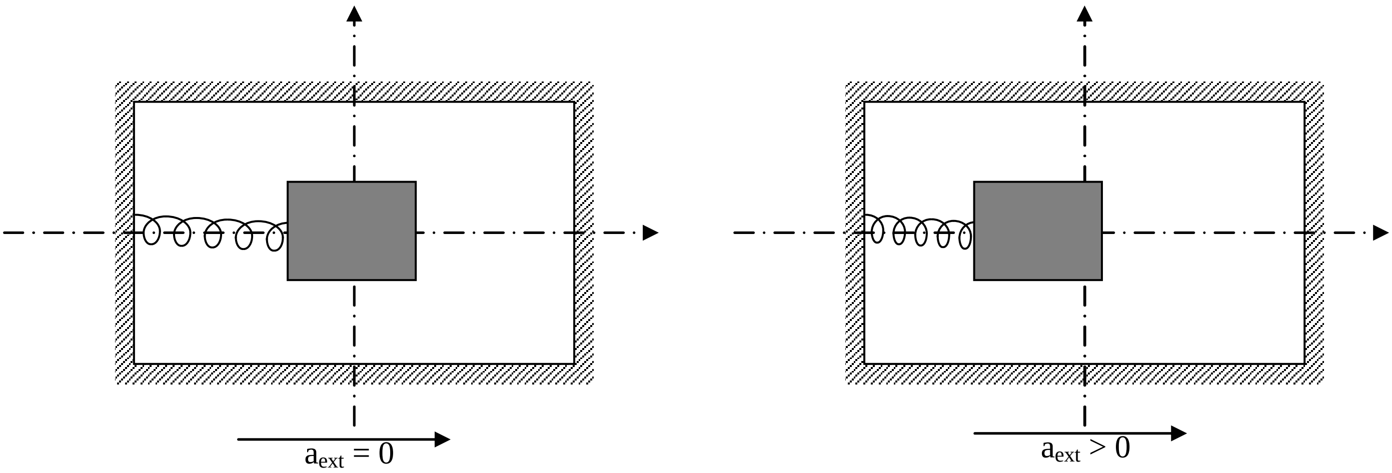

Figure 11: Principle of an accelerometer (case of spring suspension)

Sometime, the motion of the proof-mass is not really measured; for vibrating accelerometer, the motion of the proof-mass modifies the vibration of a beam; for atomic interferometer, the difference of free-fall of the atoms in different states modifies the figure of interference. In that cases, the relation of these modifications are directly related to the external acceleration.

Note: in a spacecraft, an accelerometer doesn't measure really the acceleration submitted to the spacecraft, but only the non-gravitational acceleration (the drag for example), as the spacecraft and the proof-mass are in free-fall and seen the same gravity acceleration (under the hypothesis of an accelerometer located at the centre of gravity of the spacecraft); when the accelerometer is not located at the centre of gravity of the spacecraft, the acceleration measurement contains additional terms: gravity gradient and inertial acceleration due to the rotation of the spacecraft with respect to the inertial reference frame.

4.2.2. Classification of the accelerometer technologies

The following review focuses on the accelerometers for space application. The differences between the technologies used for space accelerometer are on:

- the degree of freedom of the proof-mass: acceleration measured along one or three axes;
- the control or not of motion of the proof-mass : the proof-mass is free inside the cage or controlled to be kept at the center of the cage;
- the type of suspension : the proof-mass is let in free-fall (free suspension), the proof-mass is suspended to the cage through a mechanical hinge (pendular suspension) or the proof-mass is levitated through electrostatic forces (electrostatic suspension);
- the motion measurement: the motion is measured through variation of capacitance (capacitive detection) or is not measured due to direct relation of the external acceleration with another signal;
- the acceleration measurement: the acceleration is deduced through the relation between the motion and the stiffness force (stiffness force), the acceleration is deduced through the force needed to centered the proof-mass (electrostatic force or magnetic force), the acceleration is deduced through the modification of frequency of a beam (vibration of a beam), or the acceleration is deduced through the interference of atomic fringe (atomic interferometry).

The following table summarizes the technologies used in the different space accelerometer described in the following sections.

Accelerometer name / Mission (Supplier)	Degree of freedom	Control of proof-mass	Suspension	Motion measurement	Acceleration measurement
Q-Flex QA 3000 / - (Honeywell)	1	Yes	Pendular	Capacitive	Magnetic force
DIVA or AVAS / - (ONERA)	1	No	Pendular	No	Beam vibration
ISA / Bepi-Colombo (Thales Alenia Space)	3x1	No	Pendular	Capacitive	Stiffness
MAC / SWARM (-)	3	Yes	Electrostatic	Capacitive	Electrostatic force
SuperSTAR / GRACE (ONERA)	3	Yes	Electrostatic	Capacitive	Electrostatic force
GRADIO / GOCE (ONERA)	3	Yes	Electrostatic	Capacitive	Electrostatic force
MicroSTAR / - (ONERA)	3	Yes	Electrostatic	Capacitive	Electrostatic force
- / LISA PF (Thales Alenia Space)	3	No	Free	Capacitive	No
- / SAGAS (-)	3	No	Free	No	Integration of position

4.2.3. Q-Flex QA 3000 (Honeywell)

The accelerometer Q-Flex QA 3000 from Honeywell is a pendular accelerometer. Due to its dimension, it could be classified as a MEMS accelerometer (Figure 12).

Figure 12: Accelerometer Q-Flex QA 3000 from Honeywell

The proof-mass motion is detected through a capacitive measurement with a control of the proof-mass through magnetic suspension (Figure 13). The measurement of the current sent in the bobbin, through an external resistor provides the acceleration measurement along the direction perpendicular to the proof-mass. By properly scale this output resistor, it is possible to modify the range of the accelerometer, allowing to work on ground under ±20g or in space with less range but better resolution.

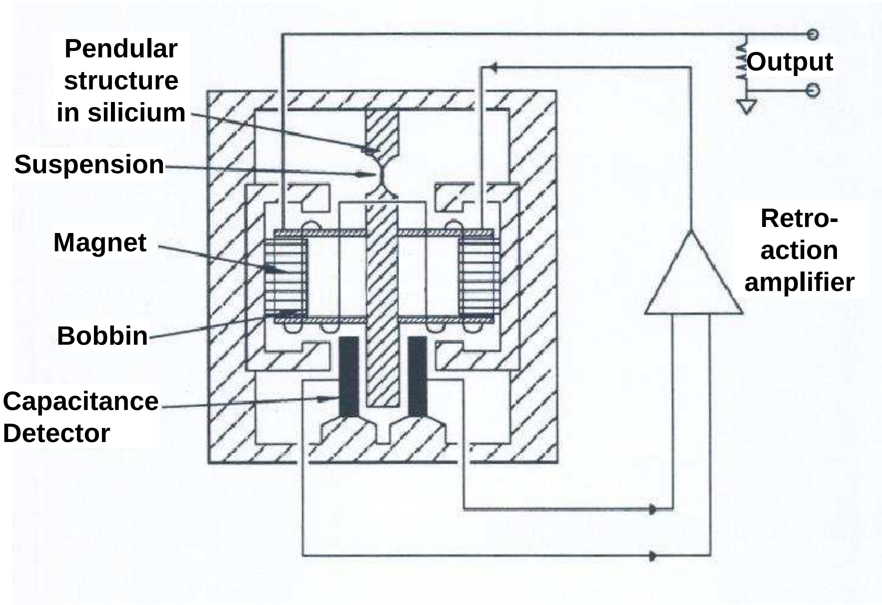

Figure 13: Schematic of theQ-Flex control loop

The suspension is done through a patented etched quartz flexible hinge, with a proof-mass in anomorphous quartz, procuring a high stability. The bobbin is supported by the proof-mass on its two faces, with 2 semi-magnetic circuits (Figure 14).

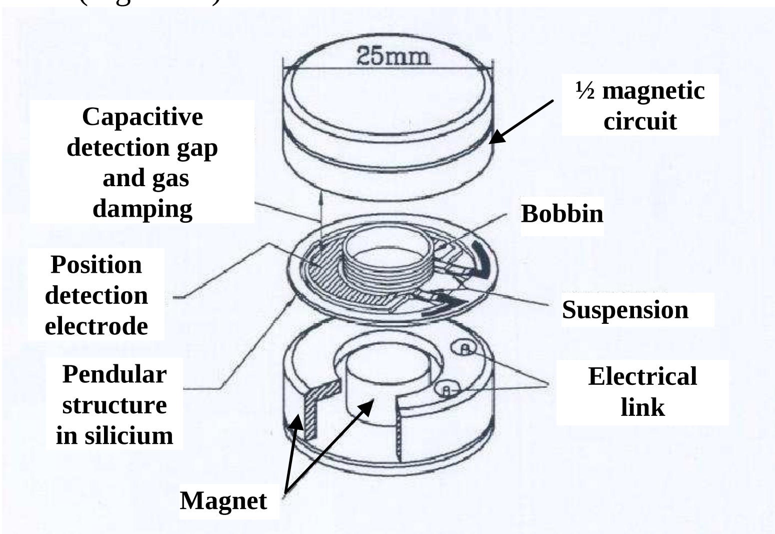

Figure 14: Exploded view of the Q-Flex accelerometer

3-axes accelerometer is obtained by fixing 3 QA-300 accelerometers on a reference structure, as in the Space Accelerometer Measurement Systems (SAMS) on the Shuttle (Figure 15).

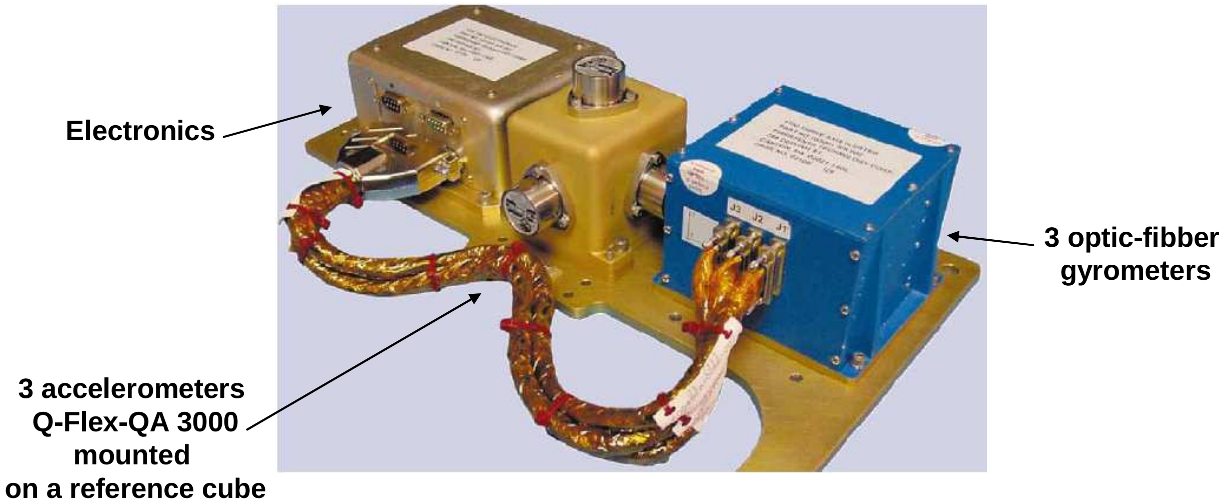

Figure 15: Space Accelerometer Measurement System on the Shuttle

In the frame of the procurement of the ONERA ASTRE accelerometer (electrostatic accelerometer similar to SuperSTAR accelerometer in the design, with less performance) for the Shuttle, the performance of the QA-3000 has been compared to ASTRE on the anti-seismic pendulum at ONERA (Figure 16).

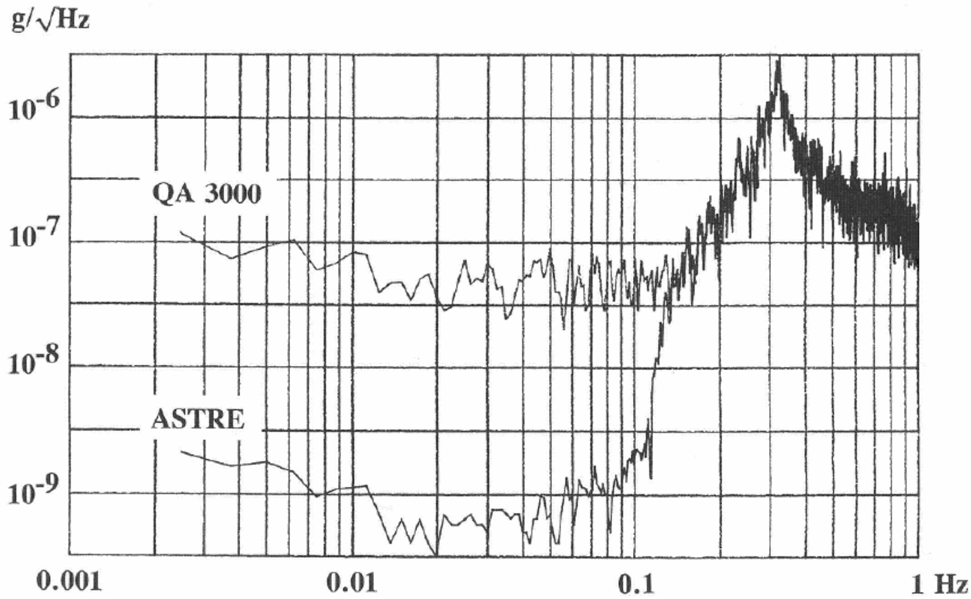

Figure 16: Comparison of QA-3000 noise with ONERA accelerometer ASTRE, on ONERA pendulum (1995)

The following table gives the main budget of the accelerometer QA-3000, scaled for a space application (from [RD19] and ONERA measurement). The mass, size and consumption are for the QA-3000 sensor without the readout electronic.

Mass	71 g (1-axis, Mec)
Consumption	0.5 W (quiescent power)
Size	Ø25 x 15 mm (Mec)
Range	$3\ 10^{-3}\ m/s^2$
Noise	$5\ 10^{-7}\ m/s^2/Hz^{1/2}$
MBW	> 300 Hz

Bias	< 4 10^{-2} m/s^2
Bias Thermal sensitivity	< 15 10^{-5} m/s^2/°C
Scale factor thermal sensitivity	< 120 ppm/°C
Misalignment	< 1000 µrad

4.2.4. Italian Spring Accelerometer (ISA) on Bepi-Colombo

The Italian Spring Accelerometer (ISA) was designed by IFSI (Istituto di Fisica delle Spazio Interplanetario) in Rome and build by Thales Alenia Space for the mission Bepi-Colombo towards Mercury. The accelerometer ISA is associated to the radio-tracking instrument (Radio-Science Experiment) in order to determine, through the precise determination of the MPO (Mercury Planetary Orbiter) orbit, the gravity field of Mercury and Post Newtonian parameters of the General Relativity ([RD20]). The scientific requirement for the acceleration measurement is an accuracy of 10^{-8} m/s^2/Hz$^{1/2}$ between 10^{-4} and 0.1 Hz.

The ISA accelerometer is a pendular accelerometer, in open-loop. The motion of the proof-mass is measured by capactive detection. With respect to the classical pendular accelerometer like Q-Flex, the particularity of the ISA accelerometer is the use of heavy proof-mass of 0.2 kg in Aluminium Al5056. The rigid frame and the sensing mass are manufactured inside one block of Aluminium (Figure 17). The suspension is a crank-shaped spring, leading to a frequency of this resonator at 3.5 Hz.

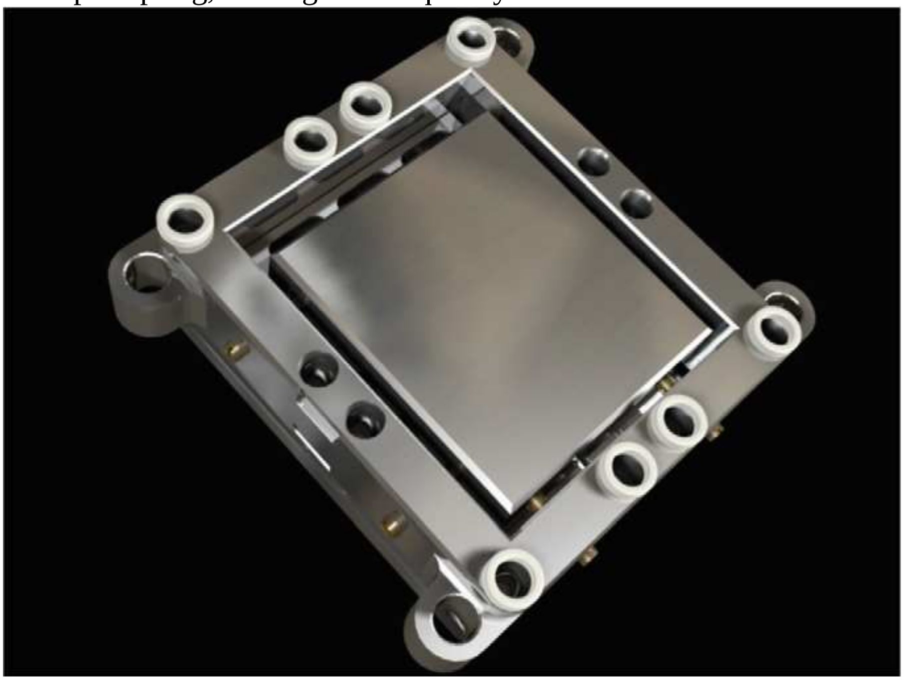

Figure 17: Sensing mass of ISA accelerometer in Aluminium, with the rigid frame and the crank-shaped spring (from [RD20])

Two detection electrodes (with a capacitance of 300 pF) are used to detect the motion of the sensing mass along the normal direction to the mass, through a capacitance bridge transducers biased at 10 kHz (Figure 18). The action capacitances are used “to lower the electromechanical frequency of the oscillator by introducing an elastic negative constant; (ii) to obtain the capacitive bridge equilibrium by means of the application of constant voltage; and (iii) to excite the mechanical oscillator by electrically known signals (used as actuators)” ([RD21]). But these action capacitances are not used for controlling the proof-mass to be kept at the centre of the cage.

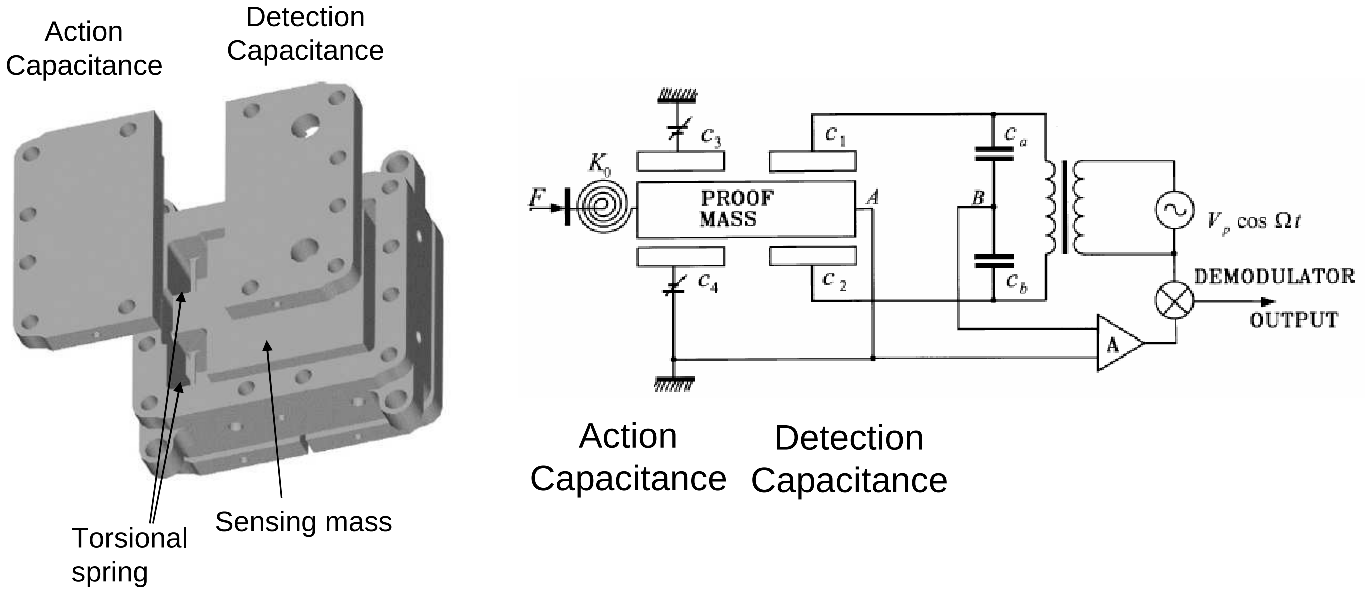

Figure 18: ISA accelerometer - Mechanical view of sensing mass and electrodes (left) and Electrical scheme of the measurement (right) from [RD21]

In order to have a 3-axes accelerometer, 3 of this pendular accelerometer are mounted together inside the spacecraft, aligned along the MPO rotation axis and co-located with the nominal centre of gravity of the spacecraft (see Figure 19). This configuration allows to minimize the effect of the rotation around the Z axis.

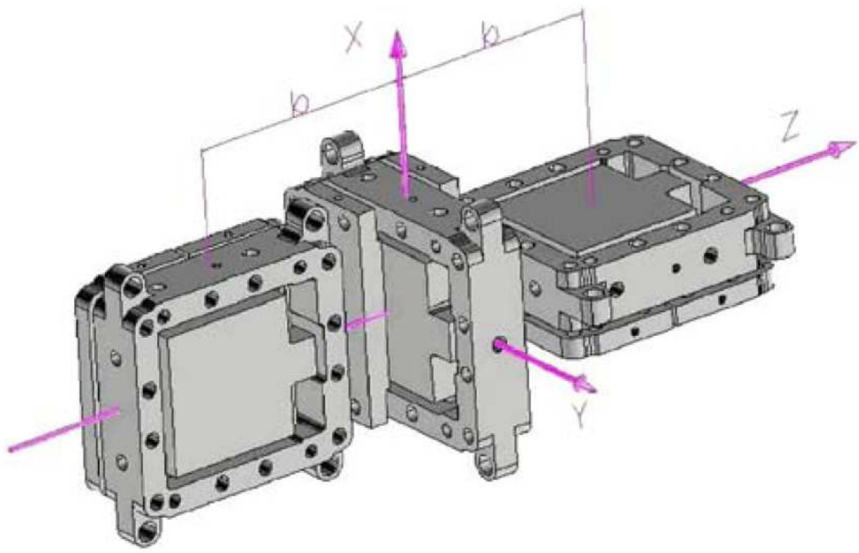

Figure 19: ISA geometrical configuration inside the MPO spacecraft from [RD22]

The announced performance of the accelerometer, in terms of intrinsic noise, is 10^{-9} m/s^2/Hz$^{1/2}$ over 3 10^{-5} Hz and 0.1 Hz: it includes the noise due to the capacitive detector and the Brownian noise of the mechanical oscillator, which is constant below the resonance frequency of 3.5 Hz ([RD21]). Some tests have been done on ground with two one-axis accelerometers in horizontal plane, along the same direction. This configuration allows to have the same seismic noise seen by the both accelerometers. The difference of their outputs gives the intrinsic noise of the accelerometer (Figure 20).

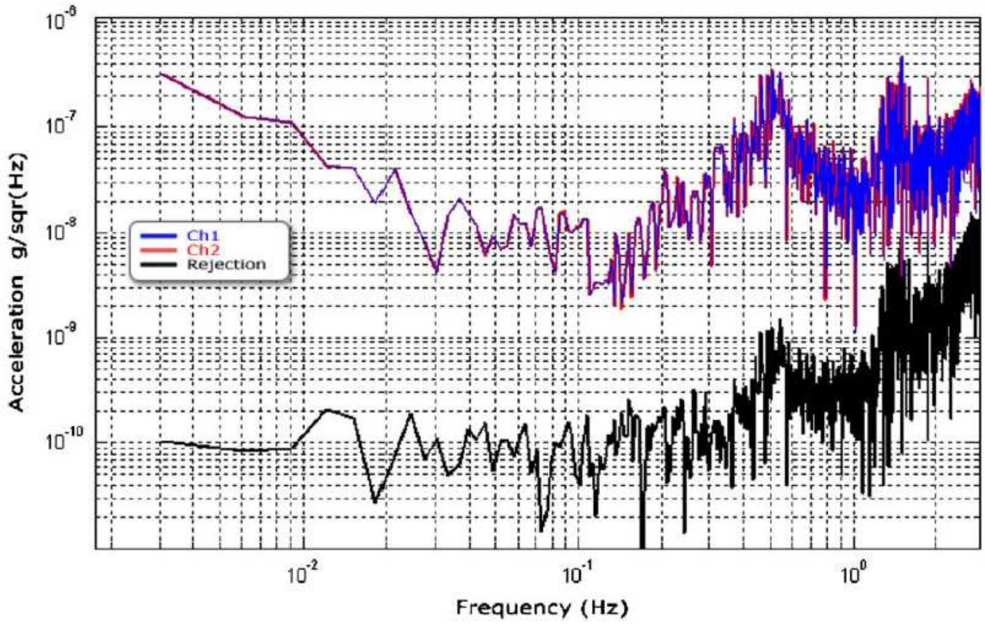

Figure 20: Differential noise of two identical pendular accelerometers in the horizontal plane from [RD20]

At low frequency, the noise is spoiled by the thermal sensitivity of the accelerometers (5 10^{-7} $m/s^2/°C$). The 3 pendular accelerometers are enclosed inside a thermal insulation box (Figure 21) and an active thermal control is used to decrease the natural temperature variation (4°C per orbit) by a factor of 700.

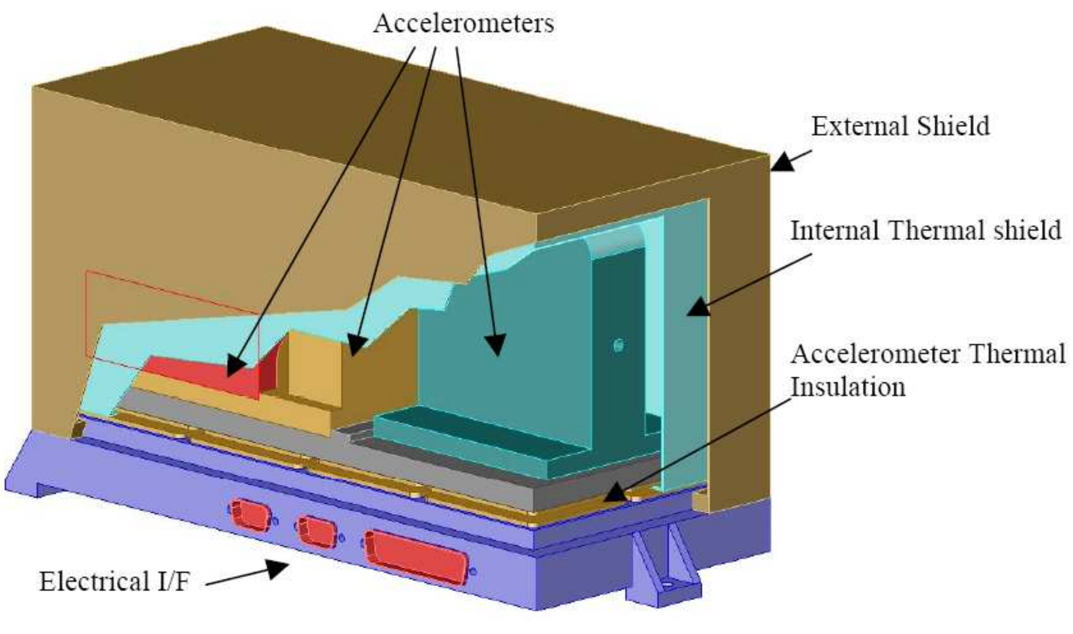

Figure 21: Thermal box around the 3 accelerometers of ISA (from [RD23])

The front-end electronics is located under the mechanical sensor, constituting the ISA Detector Assembly (IDA), and the ISA Control Electronics (ICE) unit manages the interface with the spacecraft, the thermal control (Figure 22).

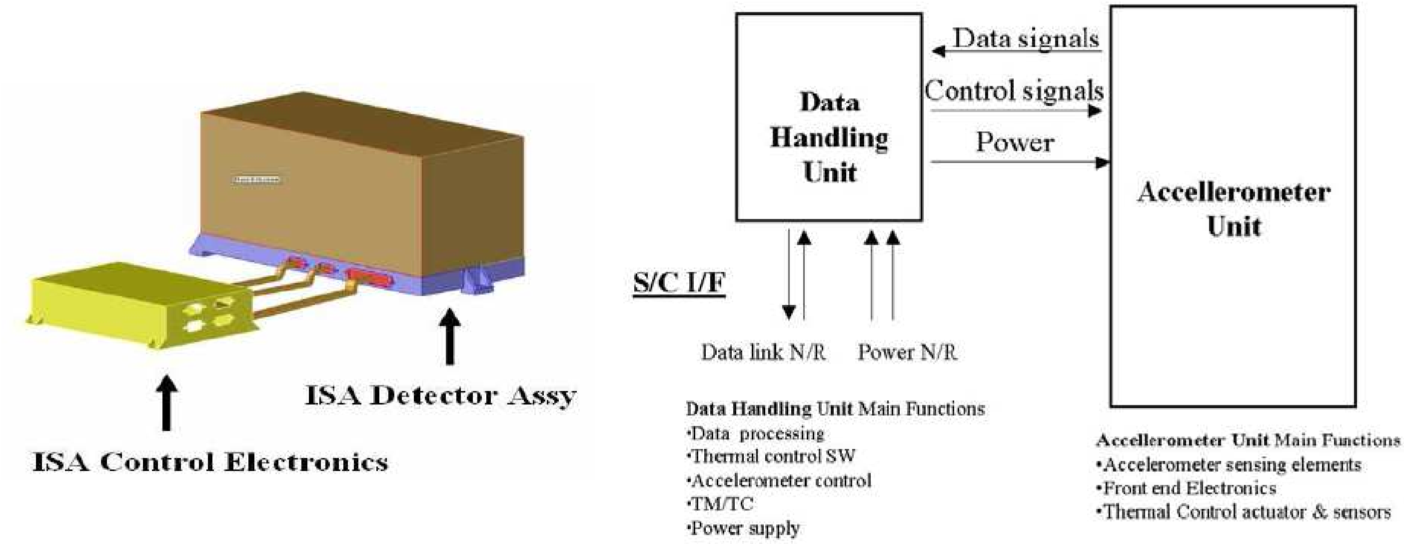

Figure 22: ISA Detector Assembly and ISA Control Electronics overview from [RD23]

The following table gives the main budget of the accelerometer ISA (from [RD20]).

Mass	5.8 kg
Size	300x170x180 mm (IDA) 170x130x86 mm (ICE)
Consumption	7.4 W (w/o heater) 10.1 W (with heater)
Range	$3\ 10^{-6}$ m/s^2
Noise	$5\ 10^{-9}$ m/s^2/Hz$^{1/2}$
MBW	$3\ 10^{-5}$ – 0.1 Hz
Bias Thermal sensitivity	$5\ 10^{-7}$ m/s^2/°C

4.2.5. Vibrating beam accelerometer DIVA and AVAS

The principle of the Vibrating Beam Accelerometer (VBA) is based on the variation of the natural frequency of a beam with respect to the tensile or compressive stress on it. The beam is fixed in one side on the rigid frame of the accelerometer and on other side on a proof-mass which have one degree of freedom thanks to its articulation. Any acceleration on the spacecraft along this direction leads to compressive or tensile stress on the beam and consequently a modification of its natural frequency (Figure 23).

Using “a piezoelectric material, it is possible to actuate and detect the oscillations of the beam by metallic electrodes which are deposited on it. An electronic oscillator, with gain and phase control, is used to excite the beam at its resonance. The output of VIA is thus the frequency of the oscillator signal, and its variations represent the applied acceleration.” ([RD27]). Since the development of quartz resonator in 1920, the quartz crystal is widely used for such vibrating beam accelerometer, thanks to their perfectly known properties. New piezo-electric materials, like LGS and GaPO4, have been also recently tested ([RD26], [RD28]).

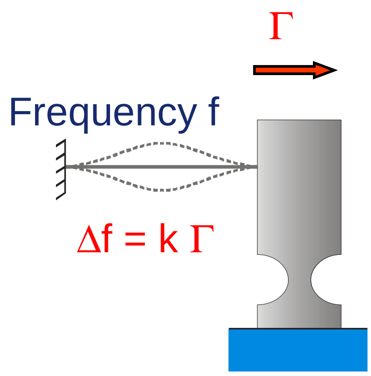

Figure 23: Principle of a vibrating beam accelerometer

One interest of the piezoelectric crystal like Quartz is the capability to realise the vibrating beam accelerometer with collective etching process on a quartz wafer. For example, it is possible to obtain 6 ONERA DIVA accelerometers on the same quartz wafer (see Figure 24) or 16 ONERA VIA accelerometers ([RD25]).

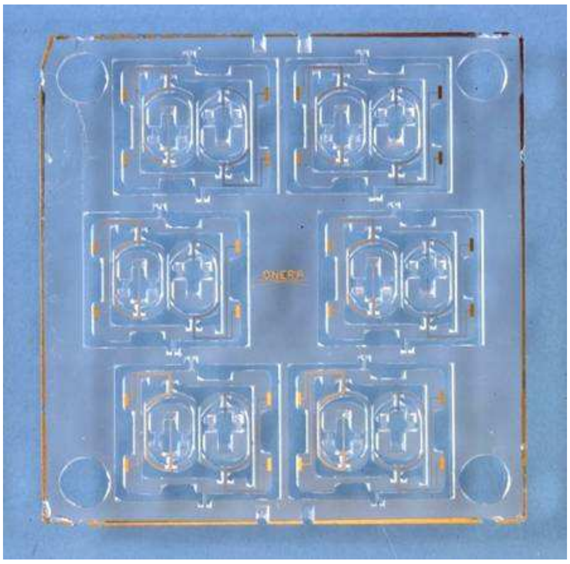

Figure 24: quartz wafer with 6 vibrating beam accelerometer DIVA from ONERA

The etching process is performed in one step, the etching depth being used to control the third dimensional structure of the sensor. The quartz wafer is metallised on each main face then, by photolithography technics, a mask of the final structure is obtained, with the possibility to have different mask for each face. Finally, the chemical etching is done in one step, and stops for an etching depth smaller than the wafer thickness. The difference corresponds to the thickness of the beam and of the articulation (Figure 25 and [RD25]).

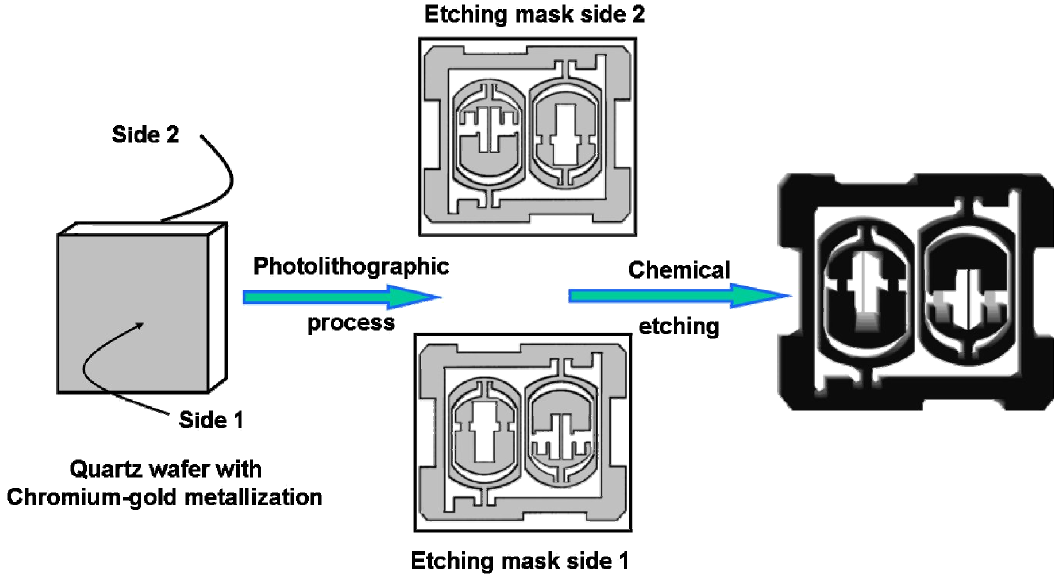

Figure 25: Chemical etching process for manufacturing Vibrating Beam Accelerometer

ONERA has developed such Vibrating Beam Accelerometer for military purpose, so for acceleration range of ± 100 g. DIVA accelerometer ([RD29]) is constituted by 2 vibrating beam accelerometers, in order to suppress the common thermal sensitivity. DIVA quartz structure is mounted on TO8 base, in a sensor case, allowing a miniature accelerometer of 35x30x20 mm^3 with its electronics (Figure 26).

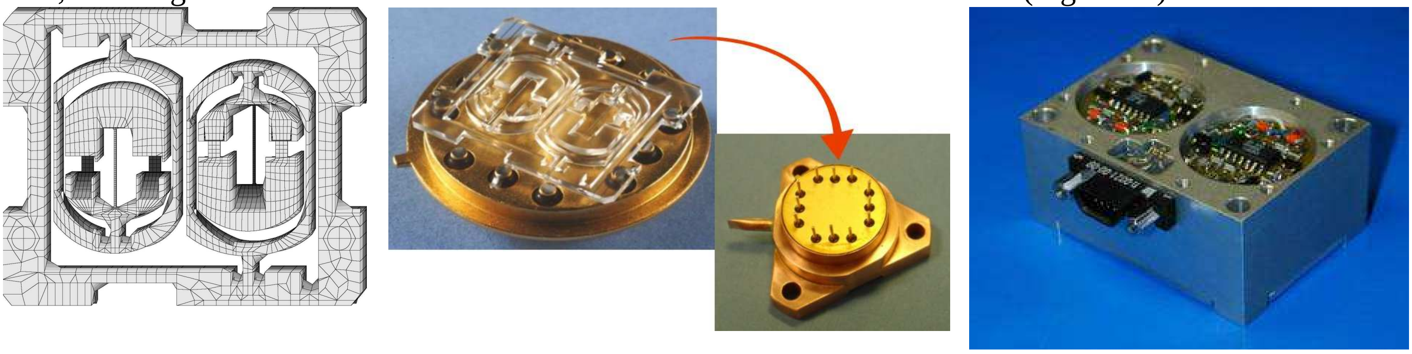

Figure 26: DIVA accelerometer, ONERA Patent

ONERA develop a new vibrating beam accelerometer, AVAS based on DIVA technology, with high resolution (10 ng), for spatial micro-propulsion applications.

The following table gives the main budget of the accelerometer DIVA and AVAS.

	DIVA	**AVAS**
Mass	< 50 g	
Size	35x30x20 mm^3	
Consumption	< 0.2 W	
Range	1000 m/s^2	10 m/s^2
Noise	10^{-5} m/s^2/Hz$^{1/2}$	10^{-7} m/s^2/Hz$^{1/2}$
MBW	> 1000 Hz	> 100 Hz
Bias	25 10^{-5} m/s^2	
Bias Thermal sensitivity	10^{-3} m/s^2/°C	
Scale factor Thermal sensitivity	2 ppm/°C	

4.2.6. SuperSTAR and GRADIO ONERA Electrostatic accelerometers

Currently, 9 ONERA electrostatic accelerometers fly in orbit around Earth: one on CHAMP mission, one on each GRACE spacecrafts ([RD30]), and 6 in the GOCE gradiometer ([RD31]). These accelerometers, with different performance, are based on the same design, at least for the mechanical sensor.

The ONERA's accelerometers are based on the electrostatic suspension of an inertial proof mass (PM) which is controlled to remain motionless at the centre of a cage by applying adequate voltages on the electrodes which are machined on the internal walls of the cage. The electrostatic forces applied on the PM compensate its relative acceleration with respect to the cage, and the control voltages are representative of the PM acceleration. As a standalone instrument, when placed at the S/C centre of gravity the voltages provide the measurement of the non gravitational acceleration.

The advantage of the electrostatic suspension for space applications is first the generation and control of very weak accelerations via well measured electric voltages applied on the electrode set mounted all around the mass. Furthermore, the operation does not need cryogenic temperatures and is managed by the accurate and steady geometry of the mass/electrodes configuration and by the use of materials with high conductivity. In these conditions, the stability of the operation characteristics is guaranteed and energy losses limited to the benefit of the instrument noise.

The proof mass is free to move within the cage as no blocking system is implemented. The cage is made of ULE plates on which 8 electrodes pairs are engraved and gold coated. The proof-mass is polarized with a thin gold wire of 5 to 7.5 µm of diameter avoiding charging of the proof-mass and variation of the patch effect in orbit (Figure 27).

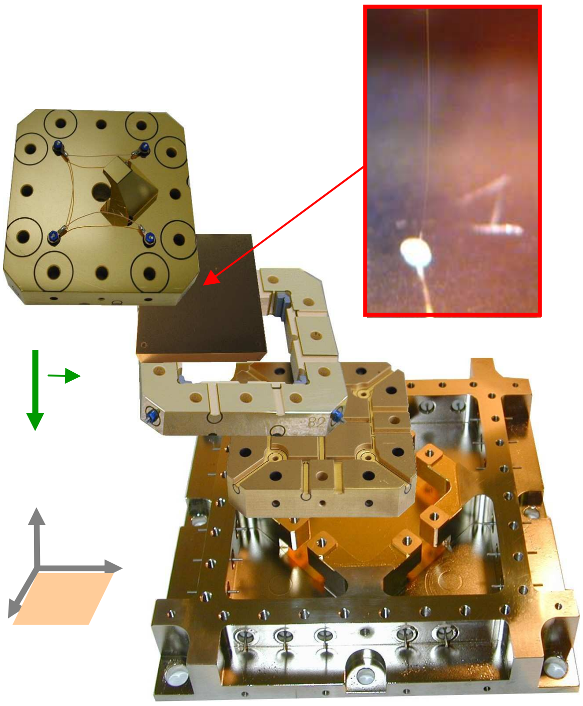

Figure 27: Split view of the accelerometer core of GOCE mission

The manufacturing of the ULE plates is based on Ultra-Sonic machining process developed at ONERA (Figure 28). It allows a soft machining of the ULE plate, avoiding any crack initiation in the material and allowing a perfect gold coating in a second step. Then, the integration of the accelerometer core, in particular the gluing of the gold wire, is done in a clean room of class 10 000, in order to avoid any dust or particle which can block the proof-mass (Figure 29).

Figure 28: Ultra-sonic machine for ULE plate manufacturing (ONERA patent)

Figure 29: Integration of the accelerometer core in clean room at ONERA

Between design of SuperSTAR accelerometer for GRACE mission and GRADIO accelerometer for GOCE mission, the differences are summarized on the following table. The choice of the material of the proof-mass and the gap and polarisation voltage explains partly the difference of performance.

	SuperSTAR (GRACE)	GRADIO (GOCE)
Proof-mass	Ta6V (72 g)	PtRh10 (320 g)
Gap (distance proof-mass / electrode)	175 µm	300 µm
Detection voltage	5 V rms	7.6 V rms
Polarisation voltage	10 V	7.5 V
Front End Electronics	Around Mechanical Sensor	In a separate unit, the FEEU, common to one pair
Control range	$5.\ 10^{-5}$ m/s^2	$3.\ 10^{-5}$ m/s^2
Measurement range	$5.\ 10^{-5}$ m/s^2	$6.6\ 10^{-6}$ m/s^2
Expected range	10^{-10} m/s^2/Hz$^{1/2}$	$2\ 10^{-12}$ m/s^2/Hz$^{1/2}$
Measurement bandwidth	0.1 – 40 mHz	5 – 100 m Hz
Gold wire diameter	7.5 µm	5 µm

The accelerometer control loops of SuperSTAR and GRADIO design present some slight differences due to the use of digital control for GOCE accelerometers (see Figure 30). The following list presents the new behaviour of the GRADIO accelerometers:

- Use of 4 electrodes pairs for YZ control and 4 electrodes for X control, allowing a reconfiguration of the electrodes, in the detection function as in the drive voltage amplifier (DVA);
- Capability to modify the combination matrices (transforming the 4 detector outputs in 3 degrees of freedom) and recombination matrices (inverse transformation), allowing to adjusting the detector and action gain to the real value;

- Presence of DAC and ADC inside the loop, for the digital PID, introducing higher level of noise and consumption in counterpart of the flexibility;
- Presence of 2 differents outputs: one for the drag-free control, at the output of the PID, with higher noise and higher range ; one after the DVA, in order to procure the science measurement with low noise but also smaller range;
- Capability to calibrate the quadratic factor by injecting in the loop at the PID output, a specific signal to shake the proof-mass;
- Capability to adjust in flight detector offset, in order to position correctly the proof-mass inside the cage : it allows in particular to correct in-flight the non linearity of the control loop

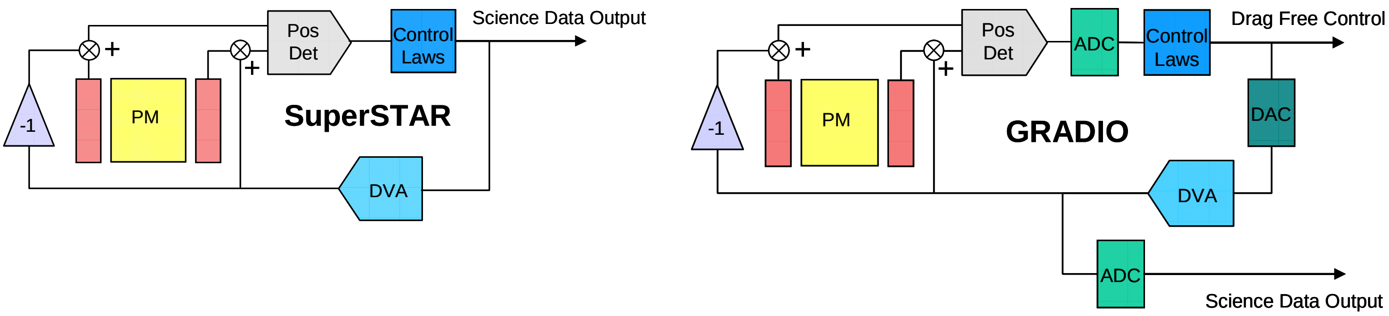

Figure 30: Simplified schematic of control loop for SuperSTAR (left) and GRADIO (right) accelerometers

In order to be tested on ground, where the PM must be levitated, the vertical axis is designed to sustain the gravity at a reasonable value of the electrode high voltages which are applied by specific ground support equipment (GSE). As a consequence, the vertical X axis is less performing than the two horizontal axes, Y and Z, which are the ultra-sensitive measurement axes.

Thanks this behaviour, several tests can be done on-ground on an anti-seismic pendulum ([RD32]):

- functional verification of the ultra-sensitive axes;
- verification of the differential scale factor inside a pair of accelerometers (Figure 31)
- verification of the non linearity of the accelerometer.

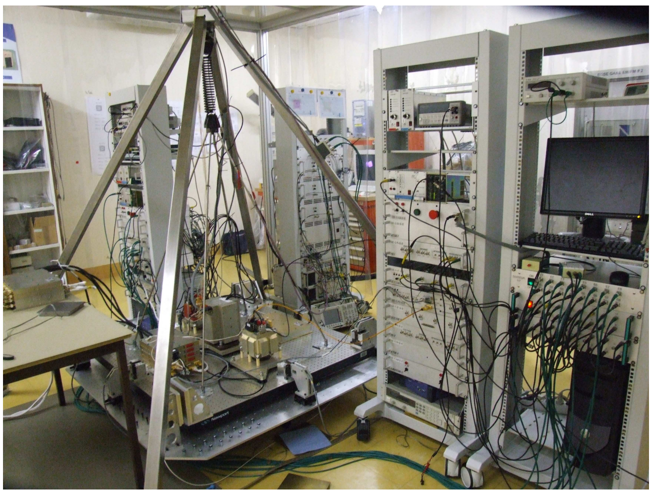

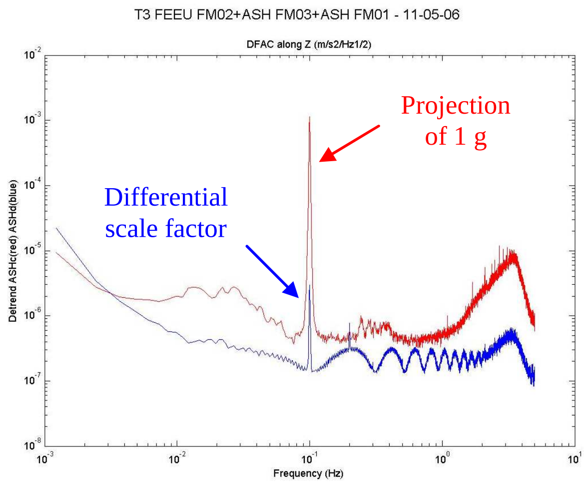

Figure 31: On ground test of the ONERA accelerometer on an anti-seismic pendulum (left) and verification of the differential scale factor (right)

During the on-ground verification on the anti-seismic pendulum, the vertical axis of the accelerometer is controlled by a specific EGSE. In order to verify the functioning of the accelerometer in the flight-condition, free-falls are performed in the ZARM tower in Bremen (Figure 32).

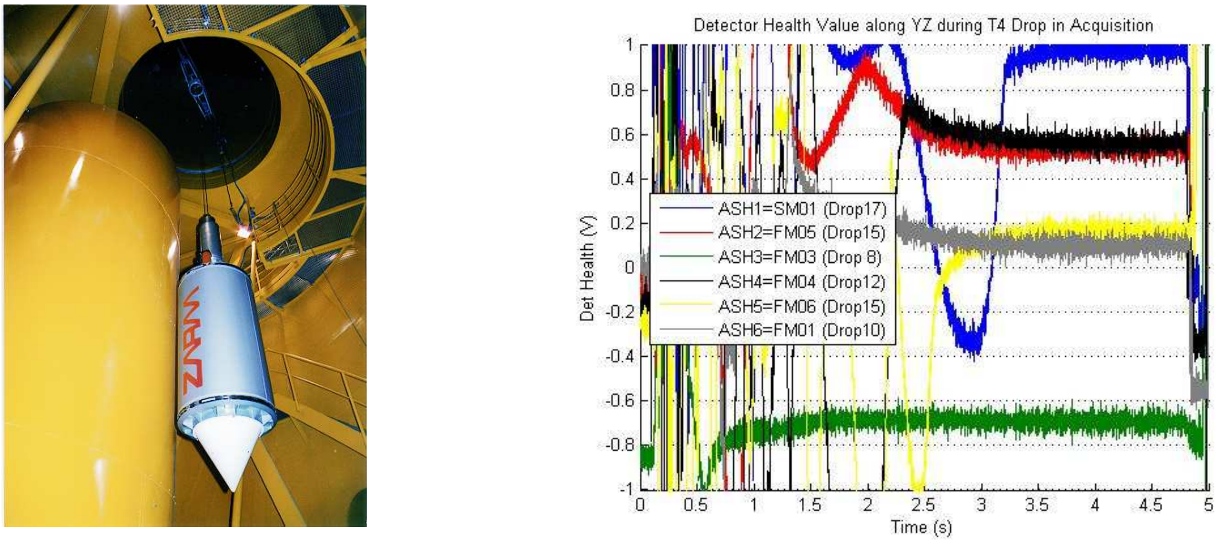

Figure 32: Free Fall test of ONERA accelerometers in the Zarm Tower(left) and verification of the acquisition of the proof-mass (right)

Thanks to the presence of 6 accelerometers on-board of GOCE accelerometers, the worst case performance of the accelerometer can be estimated through the spectral density of the gravity gradient along each arm with the hypothesis that all the error is due to the accelerometer. A performance of $3\ 10^{-12}\ m/s^2/Hz^{1/2}$ has been verified in-flight, see Figure 33, where the conversion factor from mE to m/s2 is about 2 x sqrt(2) ([RD33]).

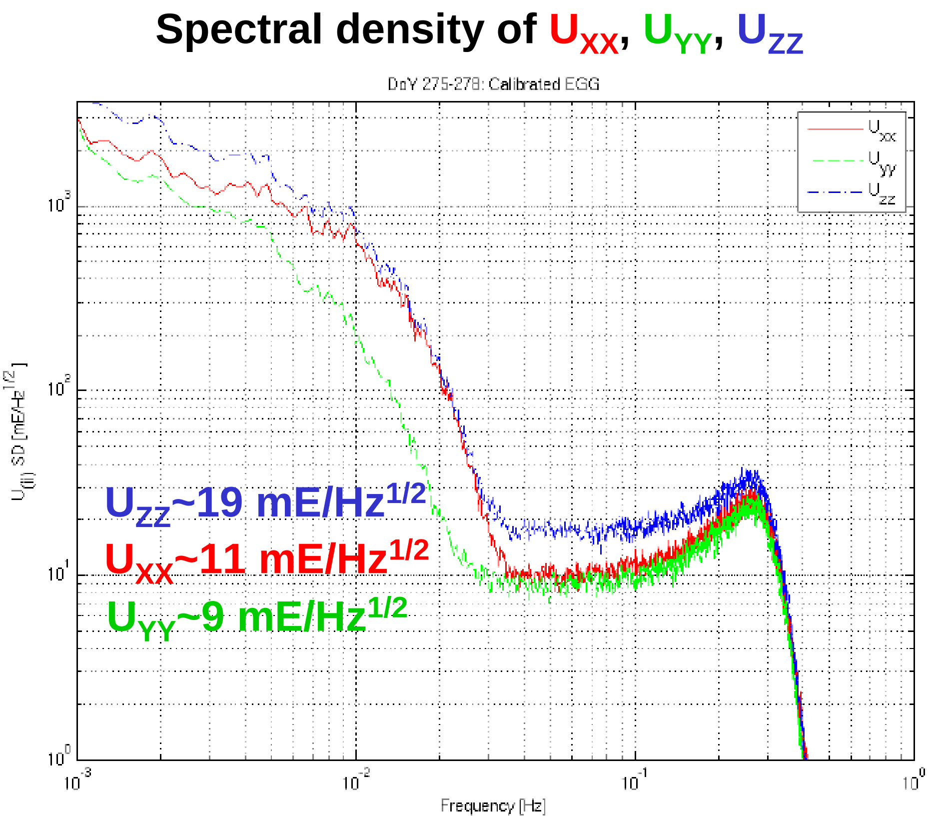

Figure 33: Spectral density of the diagonal coefficients of the gravity gradient by GOCE measurement. The level for frequency higher than 40 mHz is representative of the noise of the measurement (from courtesy of Thales Alenia Space Italy)s

The following table gives the main budget of the accelerometer SuperSTAR and GRADIO. For accelerometers of GOCE mission, the mass and consumption of the FEEU and GAIEU, have been divided by 2 (one FEEU for one pair), and 6 (one GAIEU for the 6 accelerometers).

	SuperSTAR (GRACE)	**GRADIO (GOCE)**
Mass	11.4 kg	9.4 kg
Size	13.7 litres	10.6 litres
Consumption	8 W	10.5 W
Range	$5\ 10^{-5}$ m/s^2	$6.6\ 10^{-6}$ m/s^2
Noise	10^{-10} m/s^2/Hz$^{1/2}$	$3\ 10^{-12}$ m/s^2/Hz$^{1/2}$
MBW	0.1 – 40 mHz	5 – 100 mHz
Bias	$1.6\ 10^{-5}$ m/s^2	$1.3\ 10^{-7}$ m/s^2
Bias Thermal sensitivity	$5.7\ 10^{-9}$ m/s^2/°C	$7.9\ 10^{-11}$ m/s^2/°C
Scale factor Thermal sensitivity	$2.11\ 10^{-3}$/°C	18 ppm/°C

4.2.7. MicroSTAR electrostatic accelerometer

For interplanetary mission, ONERA develop a new electrostatic accelerometer, with lower mass and consumption, with an objective of an accelerometer sensor with its front-end electronics of 1 kg and 1.4 W. The principle of the accelerometer is based on the one which has done the success of the ONERA accelerometer for geodesy missions: US machining of the silicate glass electrode plates, gold wire for polarising the proof-mass, low-noise front-end electronics … But several evolution have been applied:

- cubic proof-mass to have similar performance for the 3 linear accelerations and to obtain the 3 angular accelerations
- similar silicate glass electrodes plates, to facilitate the cost of production, with nevertheless a very good accuracy of manufacturing
- 2 gold wires to simplify the capacitive detectors.

The consequence of these choices is that this accelerometer is no more testable on-ground on an anti-seismic pendulum, except for low-performance version of the accelerometer.

The mechanical core of the accelerometer is composed of a silicate glass cubic proof-mass of 18 g, with 3 pairs of similar electrode plates, each pair controlling two degrees of freedom (Figure 34).

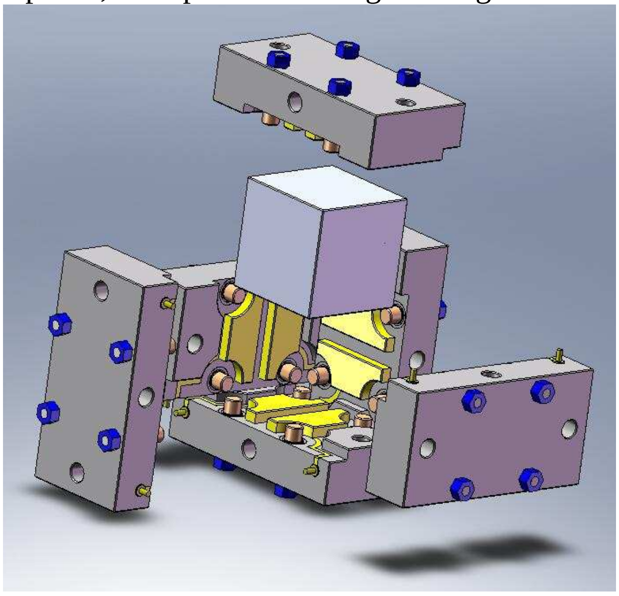

Figure 34: Core of MicroSTAR accelerometer with the cubic proof-mass and the 6 identical electrodes plates

The mechanical core is screwed on a sole plate, inside the tight housing ensuring the vacuum for a perfect functioning of the accelerometer (Figure 35). The front end electronic boards are implemented around the housing. The outputs of the accelerometer, which are the applied voltages on the electrodes to control the proof-mass, are sent to an Interface Control Unit.

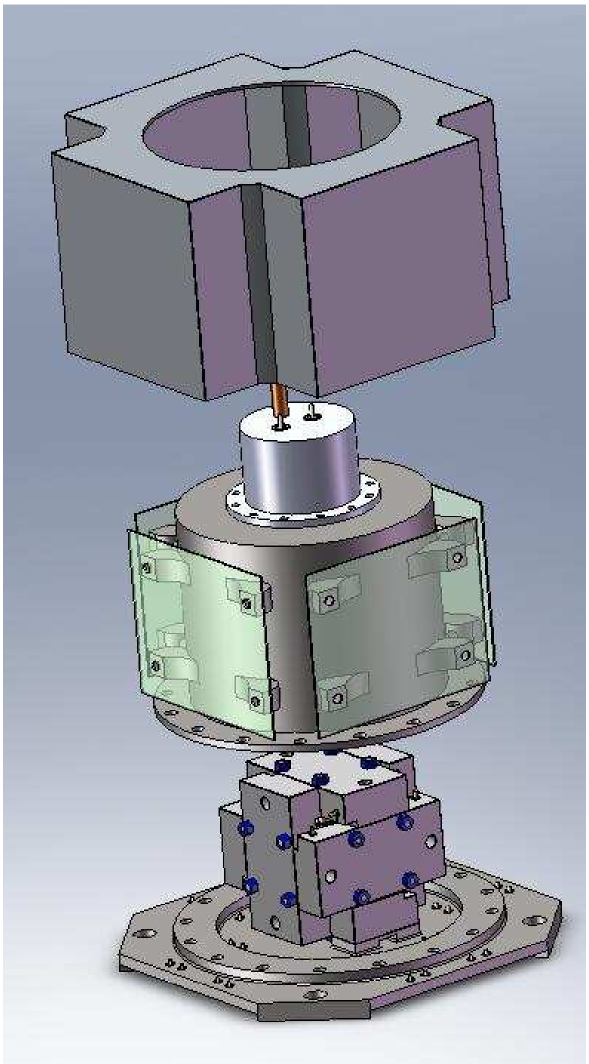

Figure 35: MicroSTAR accelerometer, with the core fixed on the sole-plate, the hermitic housing and the electronic boards fixed around it

For fundamental physics objectives, MicroSTAR accelerometer can be associated to a bias rejection system, consisting mainly in a rotating stage. This new instrument, called Gravity Advanced Package (GAP), has been proposed for the next outer planet mission ([RD35]) and for the dedicated fundamental physics mission Odyssey ([RD34]).

The principle of the bias rejection is to modulate the external acceleration by flipping regularly the accelerometer around one axis. Then, by post-processing on ground, it is possible to separate the bias from the external acceleration, with a performance of 10 pm/s^2 in the DC domain 0 to 0.1 mHz.

The following table gives the main budget of the accelerometers MicroSTAR and GAP.

	MicroSTAR	**GAP**
Mass	1 kg	3 kg
Size	1 litres	3 litres
Consumption	1.4 W	3 W
Range	2 10^{-5} m/s^2	2 10^{-5} m/s^2

Noise	10^{-10} m/s^2/Hz$^{1/2}$	10^{-11} m/s^2
MBW	1 – 100 mHz	0 – 0.1 mHz
Bias	1. 10^{-5} m/s^2	10^{-11} m/s^2
Bias Thermal sensitivity	6 10^{-9} m/s^2/°C	6 10^{-9} m/s^2/°C

4.2.8. MAC Electrostatic accelerometer on SWARM

The accelerometer MAC has been chosen to fly on the mission SWARM of ESA ([RD40]). 3 flight models have to be build. This accelerometer is an electrostatic accelerometer which inherits of the MACEK accelerometer, built by the same institute and which has flown on the Atlantis Shuttle STS 79 in September 1996 ([RD38]) and on the Russian satellite Resource 1F ([RD39]). MACEK accelerometer was also on the MIMOSA satellite, launch in June 2003 by Rokot, but, due to technical difficulties, the proof mass is freely moving in two axes only instead of three ([RD41]).

As for the ONERA electrostatic accelerometers, the proof-mass is let motionless inside the electrode cage through capacitive detection and electrostatic action. The proof-mass is cubic in fused quartz. The cage is constituted by 6 plates in gold coated quartz, where 2 electrodes are engraved (see Figure 36). There is no gold wire to polarise the proof-mass. So, it is foreseen in orbit to hit regularly the stops in order to discharge the proof-mass.

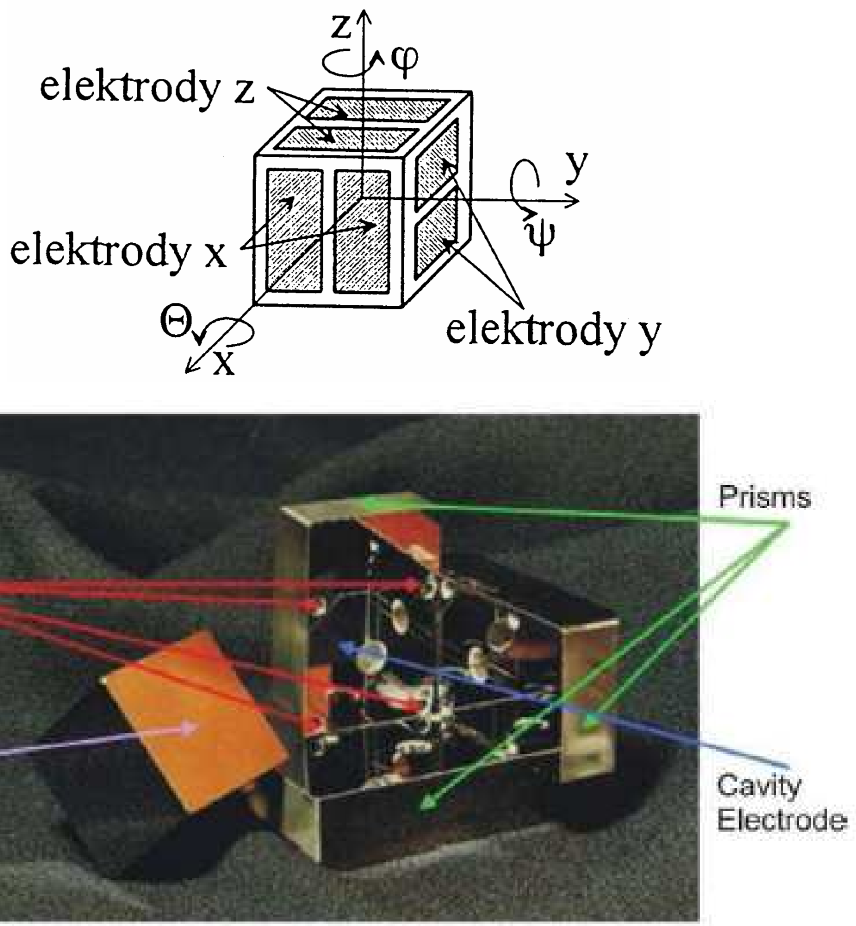

Figure 36: Fused quartz proof-mass (30x30x30 mm) and quartz electrode plates of SWARM accelerometer (from [RD40])

A complex structure allows to maintain the core aligned (Figure 37), with a need of a blocking system to maintain the proof-mass during the launch.

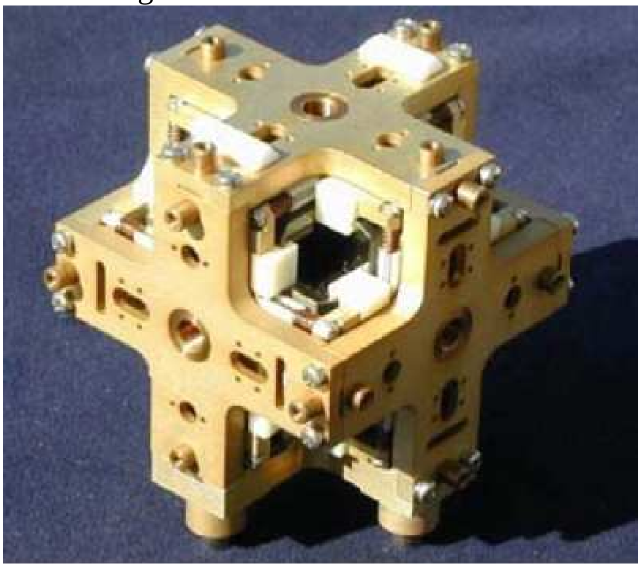

Figure 37: The accelerometer core assembly (from [RD40])

The front-end electronics is located around the mechanical sensor and on boards on the side on the instrument box (Figure 38). The 3 axes have similar performance, so it is not possible to levitate the proof-mass under 1g. According to discussion with ESA people, it seems that only free fall tests are foreseen to verify the functionality of the accelerometer. Nevertheless, there is a development of an accelerometer tester for testing the electronics board in closed loop ([RD43]).

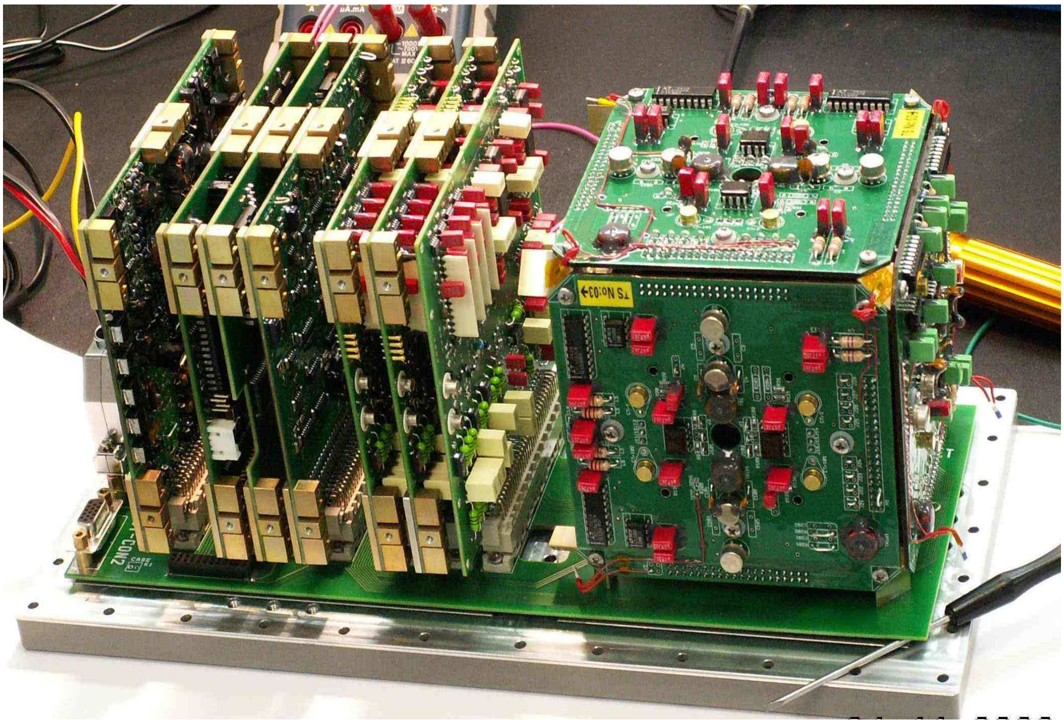

Figure 38: Opened MAC accelerometer, with the mechanical sensor on the right (surrounded by detector board) and the front-end electronics boards on the left (from [RD42])

The following table gives the main budget of the accelerometer MAC04 for the SWARM mission (from [RD42]).

Mass	6.06 kg
Consumption	3.8 W (8.0 W)
Size	177x204x360 mm
Range	2 10^{-4} m/s^2
Noise	6.3 10^{-10} m/s^2/Hz$^{1/2}$
MBW	0.1 – 100 mHz
Bias Thermal sensitivity	9.7 10^{-7} m/s^2/°C

4.2.9. Inertial Reference Sensor for LISA and LISA Pathfinder missions

The proof-masses in LISA mission are situated at the end of each interferometer arm and act as end mirrors of the interferometer. In order to detect the gravitational waves through the variation of the distance between 2 spacecrafts, it is necessary that the test masses are kept drag free in the LISA measurement band along this direction. The specification of the accelerometer noise along the sensitive axis is 2 10^{-15} m/s^2/Hz$^{1/2}$ ([RD46]). For the other directions, the test masses are controlled to stay in the centre of the Inertial Reference Sensor (IRS) thanks to capacitive position sensors and electrostatic actuators. The level of noise along these insensitive directions is specified at 3 10^{-14} m/s^2/Hz$^{1/2}$ ([RD47]).

LISA Pathfinder has the objective to test some technologies used for LISA, in particular the inertial sensor. The performance objective of LISA Pathfinder is one order of magnitude less than LISA, but the design of the instrument is totally similar.

It is important to note that intrinsically, the IRS of LISA is not an accelerometer, as the objective is not to measure the acceleration but to enable the proof-mass to move in a undisturbed free fall, so submitted only to the external gravitational forces ([RD48]). Nevertheless, some characteristics are near of the ones of an accelerometer and some technologies develop for LISA can be used for an accelerometer.

To achieve the high performance along the sensitive axis, the following elements are necessary (Figure 39):

- A heavy proof-mass of 1.96 kg;
- A caging mechanism to block this heavy proof-mass during the launch;
- Injection electrode to polarise the proof-mass with ac bias voltage;
- A charge management system;
- A vacuum enclosure ensuring 10^{-7} mbar.

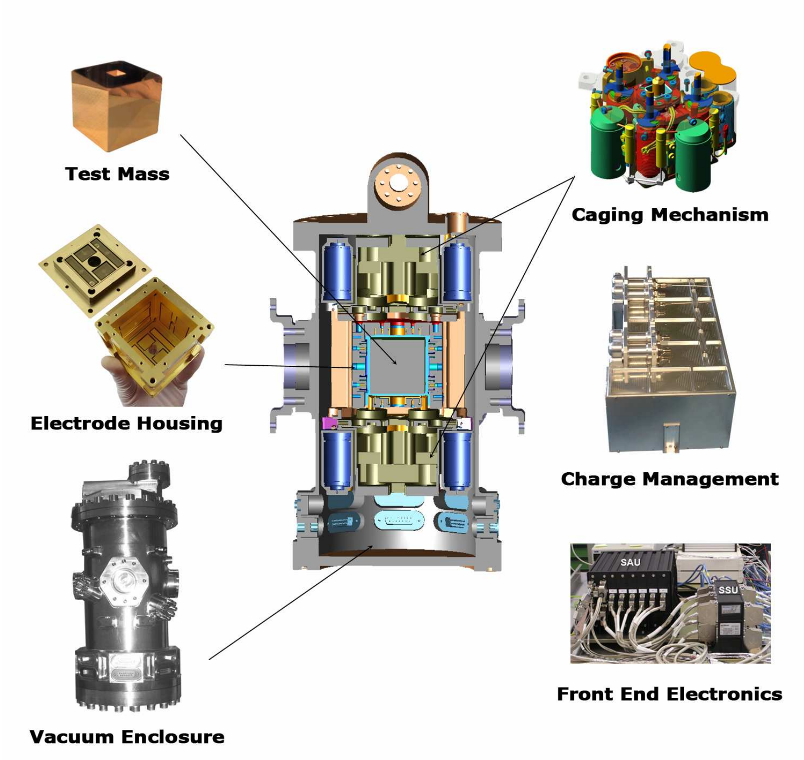

Figure 39: the different elements of the inertial sensor of the LISA mission

The cubic proof-mass is has a size of 46x46x46 mm and is done in of an alloy of about 75% of gold and 25% of Platinum (Figure 40). This alloy has been chosen for its very low magnetic susceptibility. The pyramidal wedges machined on two opposite faces of the test mass receive the plungers of the cage mechanism (Figure 41). One difficulty related to the caging mechanism is the liberation of the proof-mass in a geodesic trajectory in space. Firstly, the large gap reduces the force authority to control the proof-mass. Secondly, the gold coating of the proof-mass and of the caging device can lead to adhesive process, like van der Waals or electrostatic forces or cold welding adhesion ([RD44]).

Figure 40: 1.96 kg cubic proof-mass in gold-platinum, with the hole for the blocking mechanism, manufactured by Heraeus

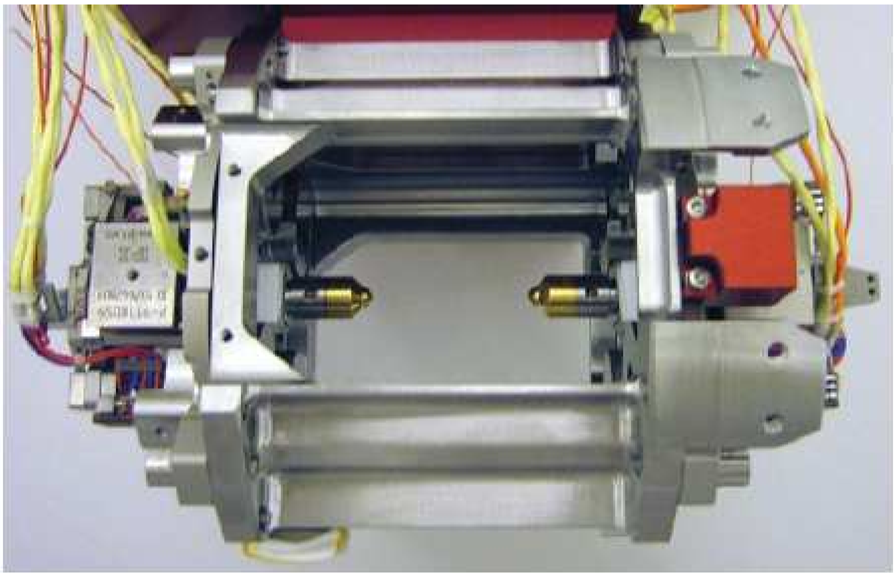

Figure 41: Flight model of the caging mechanism (side view, courtesy of Thales Alenia Space) with both plungers visible (from [RD47]).

The proof-mass is enclosed in a cage which contains 6 detection/actuation electrodes and 6 injection electrodes (Figure 42). The gap between electrodes and the proof-mass is between 3 and 4 mm, in order to minimise the patch field effect and the out-gassing pressure. The electrode housing admits the fingers and the plungers of the cage mechanism in the Z surfaces and the laser of the test mass through a hole in the X surface. The electrodes are made from a gold-coated sapphire substrate, surrounded by a molybdenum guard ring; the electrode housing structure is made from molybdenum (Figure 43).

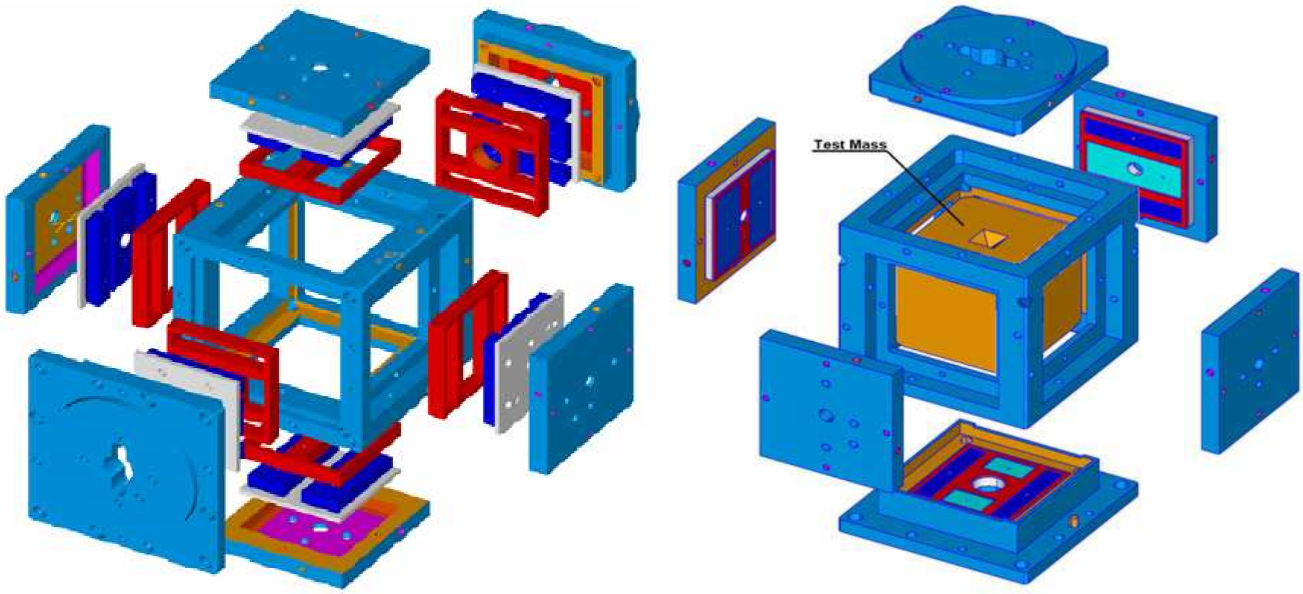

Figure 42: The mechanical core of the LISA accelerometer, with the proof-mass surrounded by 6 electrodes plates fixed on a structure. On left, the actuation electrodes for the control of the proof-mass in blue navy and the injection electrodes in light blue.

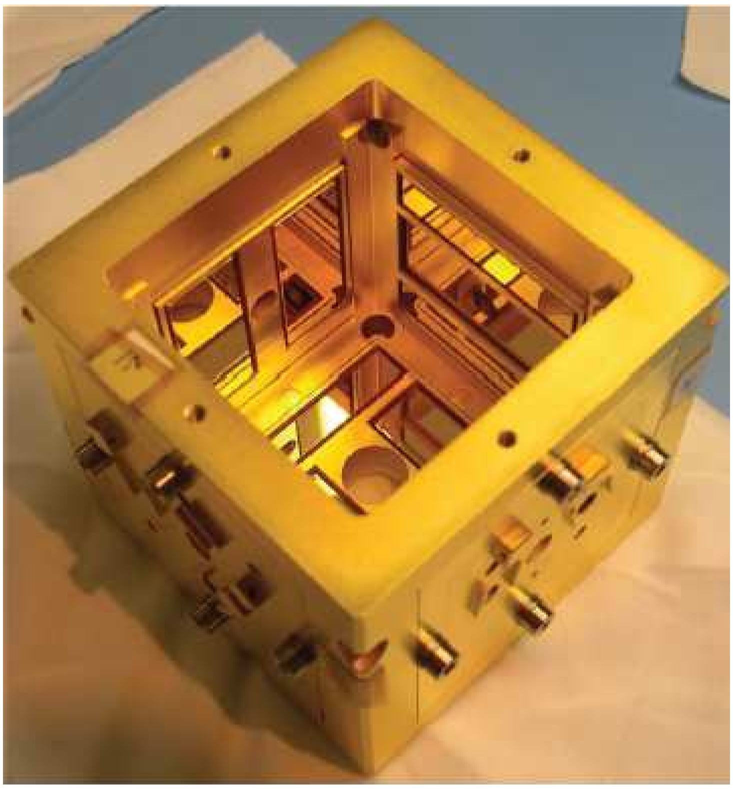

Figure 43: Electrode housing with the molybdenum and conducting ceramics gold coated sapphire electrodes (from [RD47])

To avoid the charge of the proof-mass due to the cosmic rays, a UV charge management system is used instead of a gold wire which introduces parasitic noise. The charges are removed by photo-electric effect through UV light which radiates the proof-mass and the electrodes. The UV charge management system inherits of the one which flaw in Gravity Probe B. The charges are measured by the application of an AC voltage bias on the electrodes and the detection of the induced proof-mass motion ([RD47]).

Figure 44 shows the electronic schematic for the sensitive axis. The 2 pairs of electrodes measure the linear motion of the proof-mass along X and the angular motion f through a capacitive bridge working at 100 kHz, the frequency of the AC bias injected on the upper electrodes. The Drive amplifiers supply the sensitive electrodes with an AC bias allowing to detect the charge of the proof-mass, not for the control of the proof-mass motion

The insensitive axes are controlled motionless by the accelerometer itself through electrostatic forces. But, contrarily to current electrostatic accelerometers, the actuation is not done through DC voltage bias, but with AC voltage bias, as the electrostatic forces act with the square of the electrode voltage. Any DC voltage can produce low-frequency fluctuating forces by coupling with the low-frequency noise.

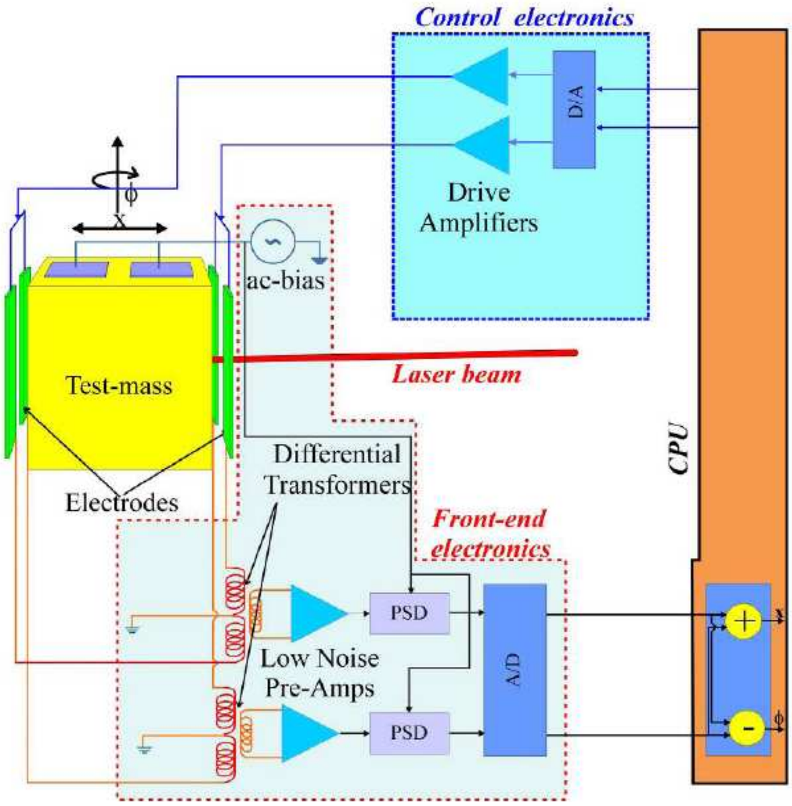

Figure 44: Accelerometer electronic scheme for sensitive axis

As IRS of LISA is not an accelerometer, it is useless to compare its performance to other accelerometers. But, the objective of the LISA mission is not so far than the one of the next gravity mission: measuring the variation of distance between two test masses on different spacecraft induced by the gravity field or gravitational waves. So, it could be nevertheless interesting to present the ultimate performance achievable for pure drag free system. The noise performance of the following table is the one of LISA IRS along the insensitive axes. The mass and consumption come from [RD50].

Mass	28.4 kg
Consumption, typical (max)	14.1 W (49.9 W)
Size	
Range (max DC acceleration)	$3\ 10^{-9}$ m/s^2
Noise	$3\ 10^{-14}$ m/s^2/Hz$^{1/2}$
MBW	0.1 – 30 mHz
Bias Thermal sensitivity	$9.7\ 10^{-7}$ m/s^2/°C

The mass budget includes the inertial sensor (for 17.74 kg including housing, electrodes, test mass, vacuum enclosure, front-end electronics SAU, harness, gravitational compensation mass), the electronics PCU, the caging mechanisms with its electronics and the charge management system. The typical consumption takes into account the inertial sensor, the Electronics PCU and the charge management system. For the maximal consumption, the caging mechanism is taken into account.

4.2.10. Inertial atomic accelerometer

The inertial atomic sensor is based on novel techniques of the mater wave emerging at the end of the last century. This technique is very similar to the optic interferometry, using mater wave instead of optic beam.

[To be completed]

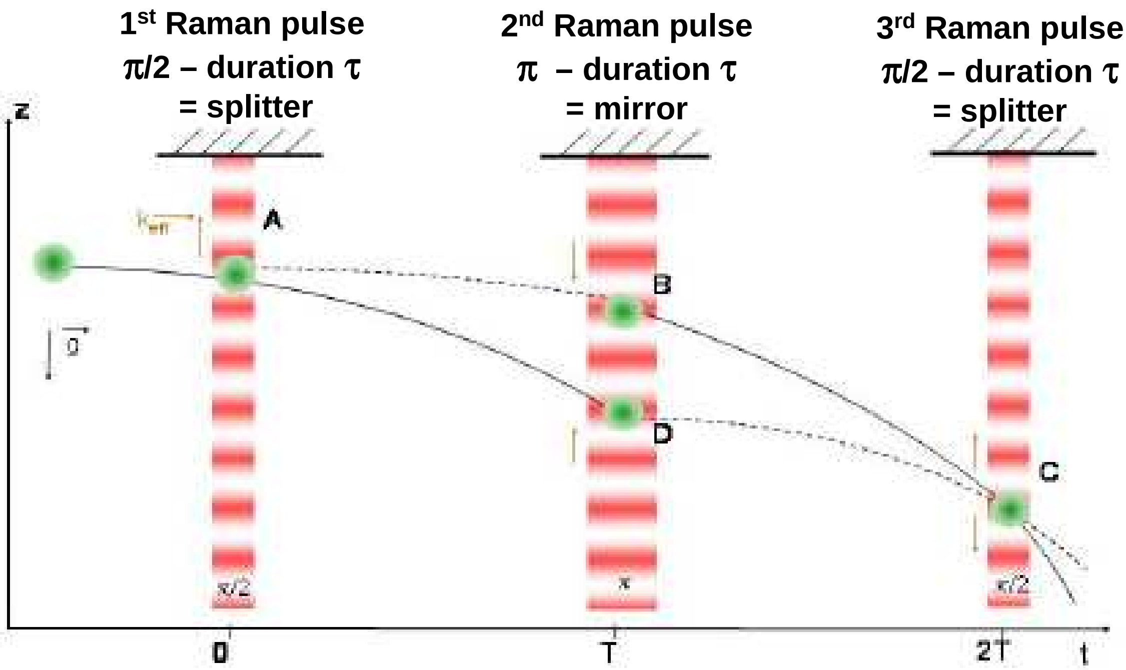

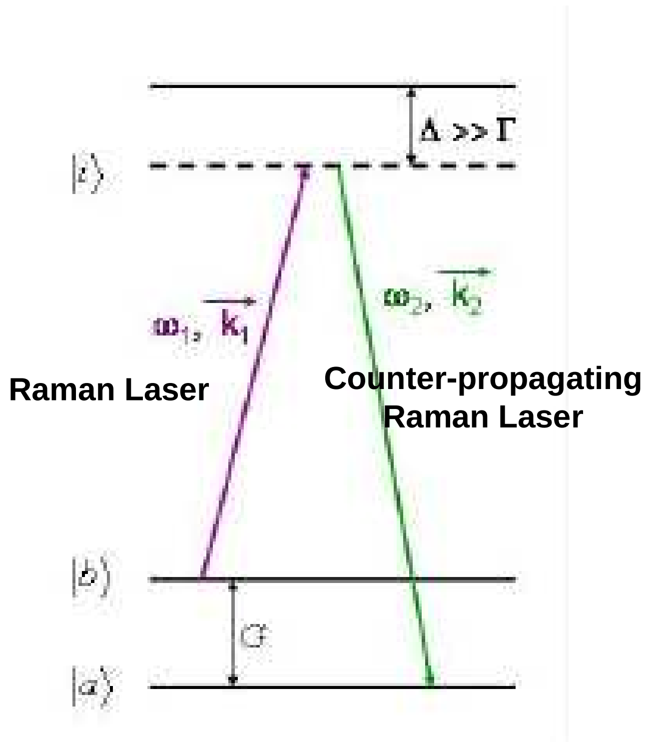

2 Hyperfine ground-states of the atoms

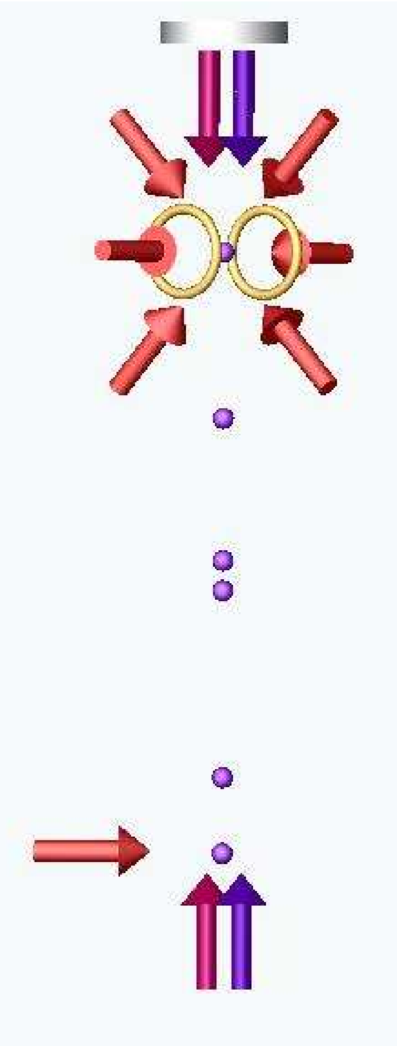

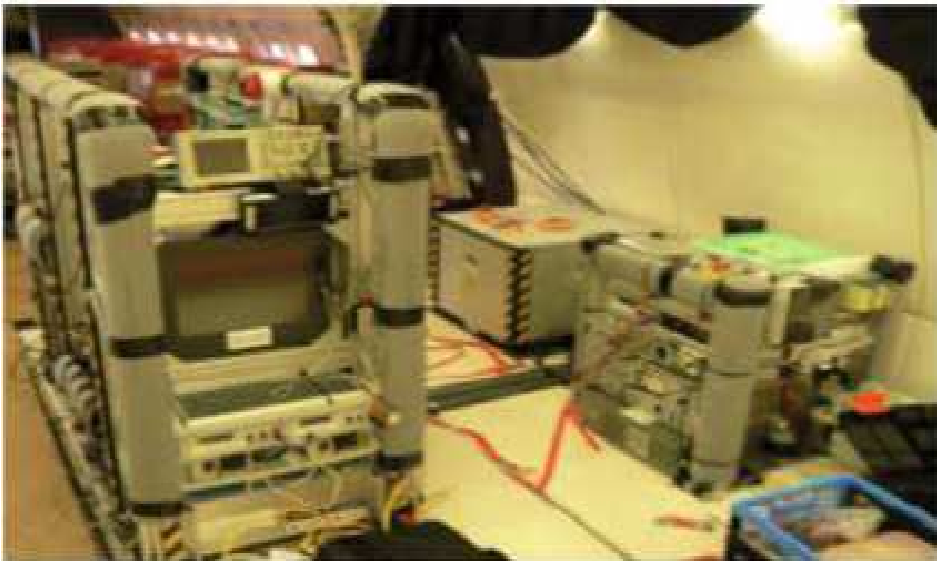

4.2.11. Comparison

The following table gives the comparison on the different accelerometer previously described. This list of accelerometers is not exhaustive but reflects the different technologies used for space accelerometers. The technology readiness level (TRL) is given by a code of colours:

- in green, the accelerometers which have already flown, so with a TRL of 9
- in orange, the accelerometers currently in development phase in the frame of a selected mission, so with a TRL between 5 and 8
- in white, the accelerometers not yet chosen in a selected mission, so considered with a TRL less than 5.

	Q-FLEX QA 3000	DIVA (AVAS)	ISA	MAC	Super STAR	GRADIO (1 ASH)	Micro STAR	LISA PF	SAGAS
Type	MEMS Pend.	MEMS Vib.	Pend.	Electro -static	Electro -static	Electro-static	Electro-static	Electro -static	Atom Interf
Nb Axis	1	1	3	3	3	3	3	3	3
Ang. Meas.	No	No	No	Yes	Yes	Yes	Yes	Yes	No
Mass (kg)	0.070	< 0.05	4.6	6.2	11.4	~9.4	3	~25	54
Cons. (W)		<0.2	7.4	4.5	8	~10.5	3	~15	68
Size (litres)	< 0.1 (Mec)	<0.02	8	7.9	13.7	~10.6	3	~10	125
Noise ($m/s^2/Hz^{1/2}$)	$5\ 10^{-7}$	10^{-5} (10^{-7})	10^{-8}	$2\ 10^{-10}$	10^{-10}	$2\ 10^{-12}$	10^{-10}	$3\ 10^{-14}$	$5\ 10^{-12}$ m/s^2
MBW (Hz) f_{min} f_{max}	> 300	> 1000	$3\ 10^{-5}$ 0.1	10^{-4} 0.1	10^{-4} 0.1	$5\ 10^{-3}$ 0.1	10^{-3} 0.1	10^{-4} $3\ 10^{-2}$	DC $3\ 10^{-5}$
Range (m/s^2)	$3\ 10^{-3}$	1000 (10)	$3\ 10^{-5}$	$2\ 10^{-4}$	$5\ 10^{-5}$	$6\ 10^{-6}$	$2\ 10^{-5}$		

Considering only the level of noise as a criterion for the choice of the accelerometer, the requirement given in §3.2.1 corresponds to the electrostatic accelerometer GRADIO of the GOCE mission. The performance of the LISA accelerometer, better than the one of GRADIO accelerometer, comes from the fact that the LISA instrument is a position sensor.

The GOCE accelerometer has also a TRL of 9, even if some improvements are necessary to achieve all the requirements:

- need to increase the measurement bandwidth toward the low-frequency;
- verification of the angular acceleration performance,
- verification of the scale factor stability,
- verification of the bias level.

These different parameters will be verified in the following chapter.

5. INSTRUMENT CONCEPTS DEFINITON AND TRADE-OFF

5.1. Concepts for the Acceleration Measurement

In this section, the different requirements of NGGM accelerometer will be reviewed with respect to the GRADIO accelerometer of the GOCE mission. The limitation of the performance will be pointed and the improvement to be done highlight.

5.1.1. Linear acceleration noise

Figure 45 presents the comparison of the performance of the GRADIO accelerometer with respect to the NGGM requirement for the ultra-sensitive axis

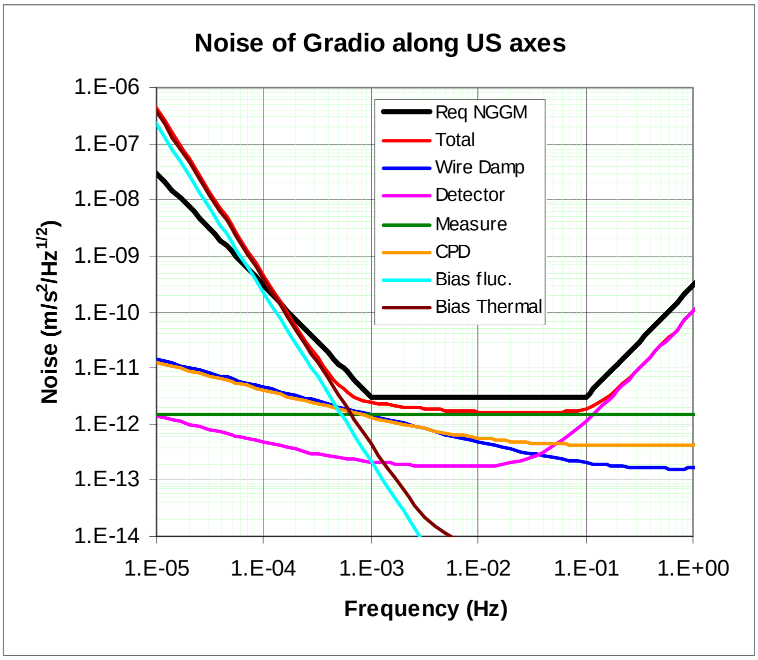

Figure 45: Comparison of the GRADIO linear acceleration noise along the ultra-sensitive axis with the NGGM requirement.

For the ultra-sensitive axis of GRADIO accelerometer, the discrepancy is only at low-frequency, due to the thermal stability. From the in-flight measurement of the GRADIO accelerometer, it is also possible to determine the worst case performance of the accelerometers, considering that all the error of the gravity gradient measurement between 40 and 100 mHz comes from the accelerometers (Figure 33). From these measurements, the in-flight proven performance is between, 3.1 and 6.7 10^{-12} $m/s^2/Hz^{1/2}$. The reason of the discrepancy is not known, but the in-flight verification proves that it doesn't come from the electronic functions of the accelerometer.

Nevertheless; it shall be necessary to continue to analyse the GOCE measurement in order to find the source of this discrepancy, in order to improve, if necessary, the future accelerometer for NGGM mission.

Figure 46 presents the comparison of the performance of the GRADIO accelerometer with respect to the NGGM requirement for the less-sensitive axis.

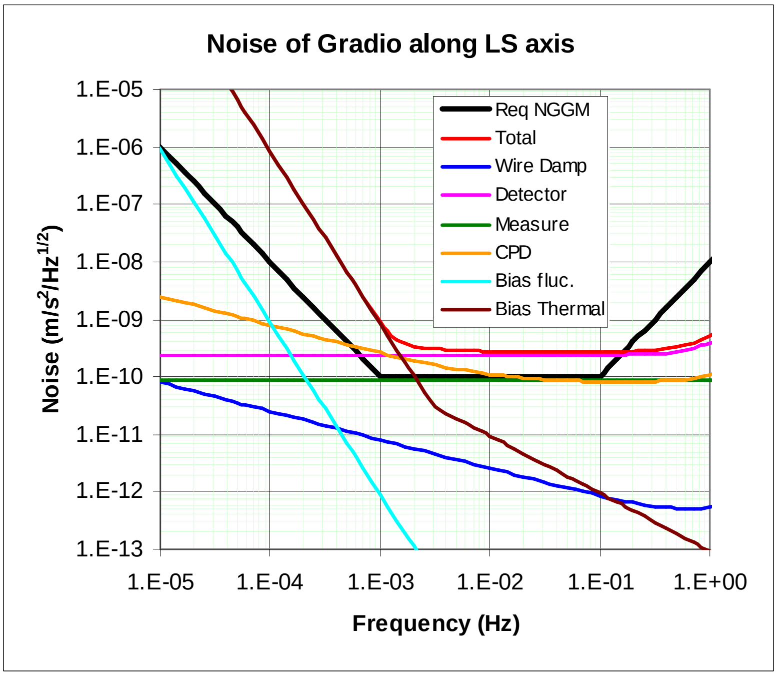

Figure 46: Comparison of the GRADIO linear acceleration noise along less-sensitive axis with the the NGGM requirement

For the less-sensitive axis, the discrepancies are at low frequency, due to the thermal stability, but also in the measurement bandwidth. To improve the performance in the measurement bandwidth, it shall be necessary to improve the detector noise, the level of contact potential difference noise and the level of the measurement noise.

For the detector noise, the main contributor is the noise of the ADC1. The ADC1 is an AD7712 Sigma-Delta, 24 bits. The different possibilities to improve the performance are:

- to find a better ADC, but currently it doesn't exist on the market,
- to increase the gain of the detector, but it will impact the capability to acquire or control the proof-mass :in the current configuration, only about 2 µm over 16 µm are observable in science mode (8-14 µm over 16 µm in acquisition mode),
- to have an analog loop instead a digital one, but with less flexibility in the operation (for the calibration or correction of the quadratic factor – but which is very low for less-sensitive axis – , for the recovery of detector failure …),
- to have 3 ultra-sensitive axes, but with the disadvantage to not be able to perform levitation on ground
- to use several accelerometers in order to have ultra-sensitive axis along all the directions.

5.1.2. Angular acceleration noise

Figure 47 compares the current performance of the angular acceleration noise around the less-sensitive axis with the requirement for NGGM. The contributors of the angular acceleration noise have nee, deduced from those of the linear acceleration noise, taking into account the level arm of the electrodes. If it is perfectly correct for all the electronic noises, it is perhaps a worst case for the parasitic acceleration noise. Nevertheless, the current performance is perfectly in-line with the requirement.

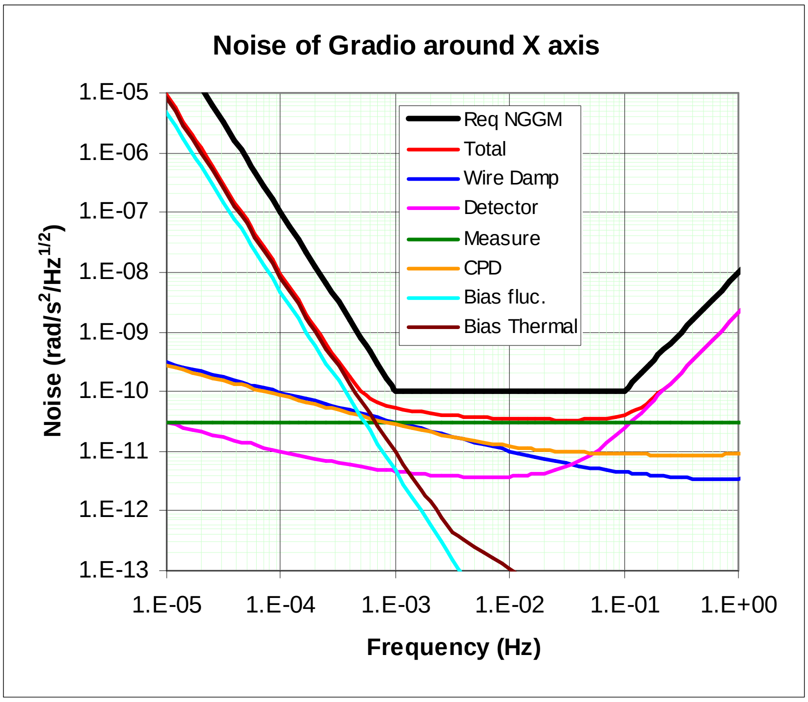

Figure 47: Comparison of the GRADIO angular acceleration noise around the less-sensitive axis with the NGGM requirement

Figure 48 presents the performance of the angular acceleration noise of GRADIO accelerometer around the ultra-sensitive axis with respect to the NGGM performance.

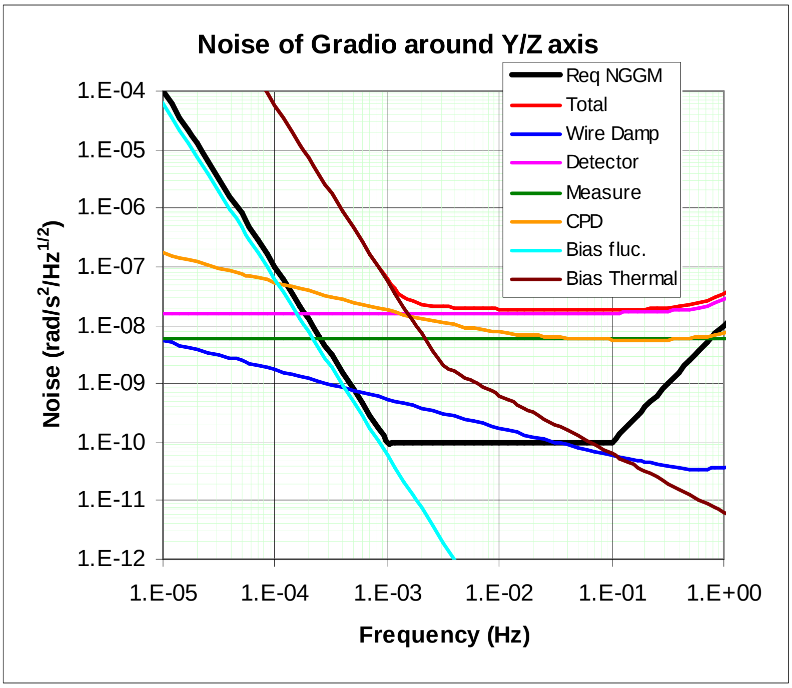

Figure 48: Comparison of the GRADIO angular acceleration noise around the ultra-sensitive axis with the NGGM requirement

The control of these angular motions is done with the less-sensitive electrodes explaining the higher level of noise, with about 2 orders of magnitude with respect to the requirement. Moreover, due to the shape of the proof-mass, the electrostatic moments applied to the proof-mass to control its motion are not proportional to the angular accelerations of the spacecraft for these 2 degrees of freedom, as it appears in the following equations:

$$\dot{\omega}_{X,el} = \dot{\omega}_X + \frac{I_Z - I_Y}{I_X}\omega_Y\omega_Z \approx \dot{\omega}_X$$

$$\dot{\omega}_{Y,el} = \dot{\omega}_Y + \frac{I_X - I_Y}{I_Y}\omega_X\omega_Z \approx \dot{\omega}_Y + \omega_X\omega_Z$$

$$\dot{\omega}_{Z,el} = \dot{\omega}_Z + \frac{I_Y - I_X}{I_Z}\omega_X\omega_Y \approx \dot{\omega}_Z - \omega_X\omega_Y$$

where I_Y and I_Z are the inertia moments around the ultra-sensitive axes (I_Y=I_Z=4.5 10^{-5} kg.m^2) and I_X is the inertia moment around the less-sensitive axis (I_X=8.5 10^{-5} kg.m^2).

To overcome this discrepancy for the angular acceleration noise, several solutions are possible:

- to use a cubic proof-mass, which implies a modification of the design of the electrode cages : either with 6 electrode plates like in the MicroSTAR, MAC or LISA accelerometers, either by increasing the hight of the ring-plate of the GRADIO accelerometer,
- to use several accelerometers in order to deduce the angular acceleration with combination of the linear accelerations or with the angular outputs of the accelerometer with different orientation.

5.1.3. Scale factor stability

Figure 49 and Figure 50 show the figure of noise of the scale factor stability along less- and ultra-sensitive axes of the GRADIO accelerometer, with respect to the requirement for NGGM.

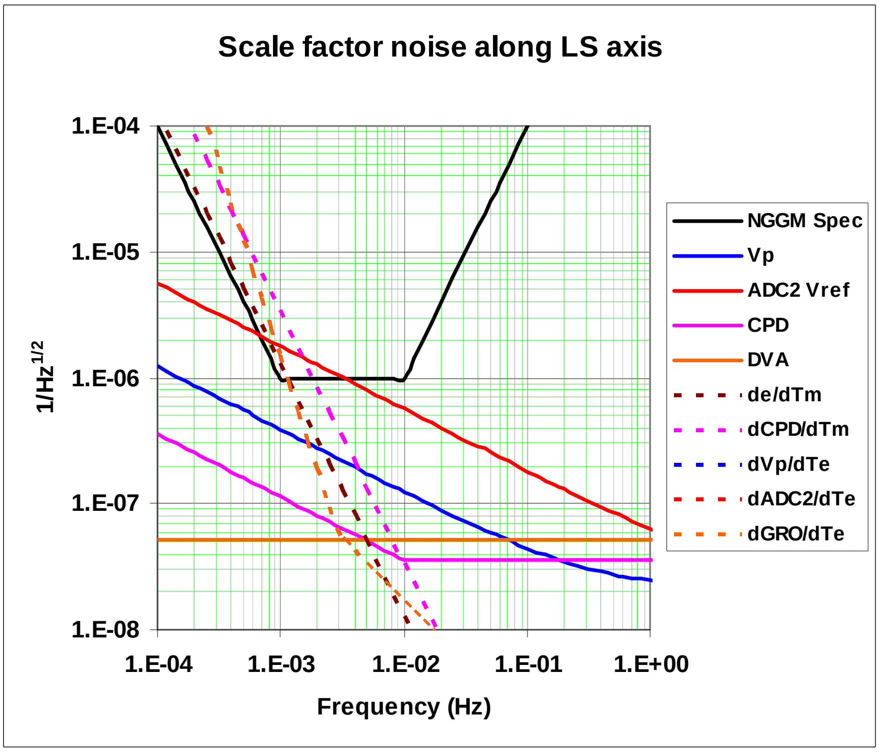

Figure 49: Comparison of the GRADIO scale factor noise along the less-sensitive axis with the NGGM requirement

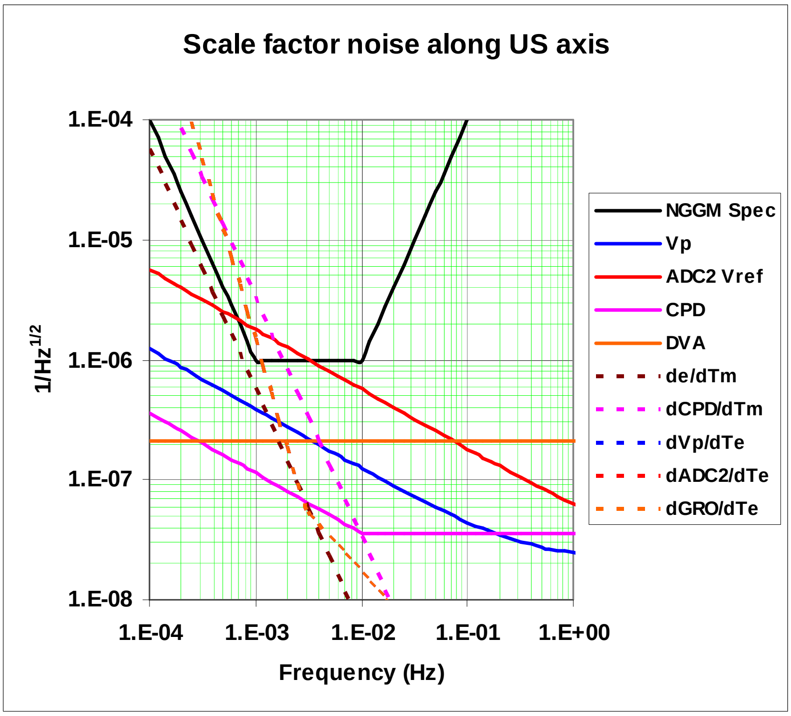

Figure 50: Comparison of the GRADIO scale factor noise along the ultra-sensitive axis with the NGGM requirement

At low-frequency, the limitation is due to the thermal stability of the contact potential difference and of the thermal stability of the electronics (polarisation voltage, ADC2 reference voltage and read-out gain, the 3 curves being superimposed). The thermal sensitivities of the electronics have been already optimised for the GOCE mission, and it seems difficult to achieve better performance. The other solution is to improve the thermal stability around the mechanical sensor (for the contact potential difference) and around the electronics.

Another limitation is due to the reference voltage noise of the ADC2. This contributor could be improved at the level of the polarisation voltage (Vp curve), by using several voltage generators in parallel to reduce the noise (for polarisation voltage, 4 reference generators are used) and by a better choice of the generators.

5.1.4. Accelerometer bias

The requirement for the bias level is given only for the cross-track and radial axes. For GRADIO accelerometer, the expected bias level is given in Figure 51.

Bias along ultra-sensitive axis : $1.2\ 10^{-5}\ m/s^2$ (due to gold wire stiffness)

Bias along ultra-sensitive axis : $1.3\ 10^{-7}\ m/s^2$ (due to gold wire stiffness)

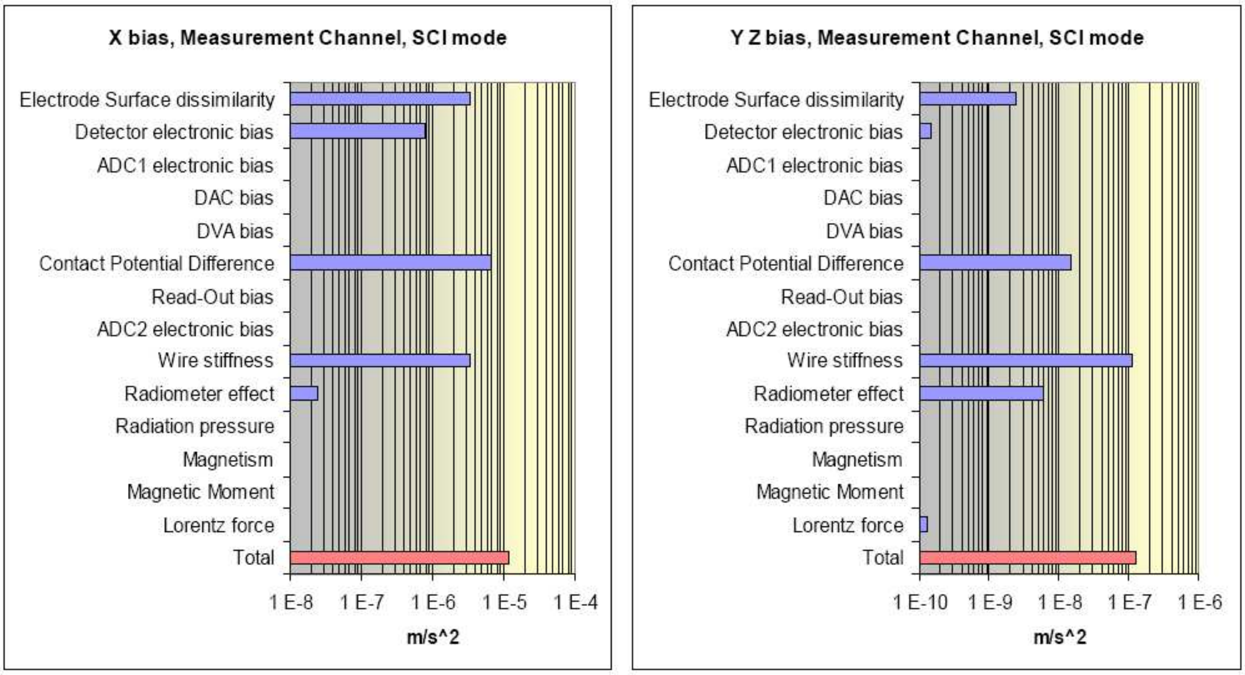

Figure 51: GRADIO acceleration level of bias for less-sensitive axis (left) and ultra-sensitive axes (right)

The main contributor for the ultra-sensitive axis is the gold wire stiffness, but the level is lower than the NGGM specification. For the less-sensitive axis, the level of bias is higher by 2 orders of magnitude, due to the electrode surface dissimilarity, the detector bias, the contact potential difference and the gold wire stiffness. The difference between less- and ultra-sensitive axes is mainly due to the difference of gap and electrode surface, needed for a ground levitation of the proof-mass for testing.

As the less-sensitive axis will not be along the track (for the noise level required), it is necessary to find solution to achieve the requirement:

- by having 3 ultra-sensitive axes, with the disadvantage to not be able to test the proof-mass on ground,
- by calibrating in flight the bias (see Annex 1)
- by using several accelerometers with different orientation in order to measure the linear acceleration along the 3 directions with ultra-sensitive axes.

5.1.5. *Trade-offs*

From the review of the NGGM requirements and the limitation of GRADIO accelerometers, it appears that several improvements could be done. Some characteristics of the GRADIO accelerometers appear also as limitation and shall be discussed more deeply (gold wire, less-sensitive axis).

5.1.5.1. Thermal contributor to the low-frequency noise

The first improvement concerns the thermal stability of the accelerometer environment in order to decrease the noise at low-frequency of the linear output as the one of the scale factor.

It is important to note that the thermal stability has been added in the figure of noise of the accelerometer, but it is often not a stochastic noise, in particular at low frequency where it is related to the evolution of the temperature along the orbit. Consequently, it could be possible to decrease the impact of the thermal stability by a calibration of the thermal sensitivity of the accelerometer and by a measurement of the temperature around the accelerometer for correcting its effect in the measurement. The calibration of the thermal sensitivity could be done through the calibration of the bias at different temperature, for example with the principle presented in Annex 1.

Another way to decrease the low frequency noise is to decrease the thermal stability. As an example, Figure 52 presents the figure of noise of the GRADIO accelerometer along the ultra-sensitive axis when the temperature stability is divided by a factor 100.

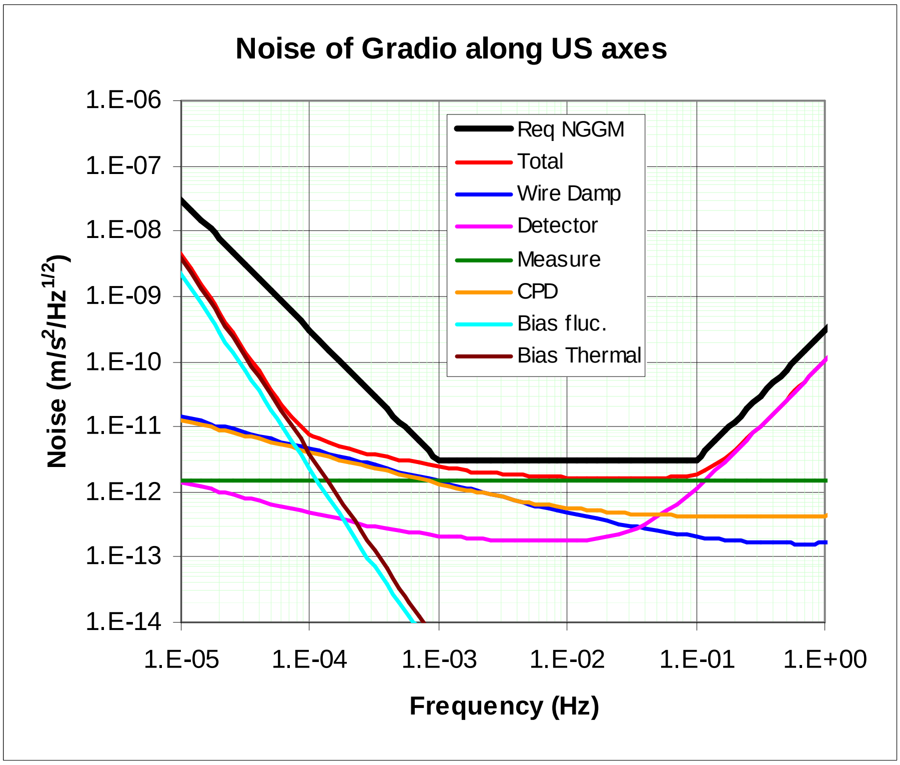

Figure 52: GRADIO accelerometer noise with the temperature fluctuation divided by 100 with respect to the GOCE environment

The Annex 2 presents a deeper analysis of the contributors of the thermal drift of the accelerometer bias, and the preliminary in-flight verification of the temperature stability. It appears that the temperature stability has a slope in 1/f in the FEEU and on the external face of the gradiometer canister, instead a slope of $1/f^2$ as expected. It justifies specifying a slope in $1/f^2$ for the accelerometer, taking into account the transfer function of the accelerometer.

5.1.5.2. Less-sensitive axis or not

The presence of a less-sensitive axis on the GRADIO accelerometer is due to the capability to perform levitation on ground. In the current configuration with a gap of 30 µm between less-sensitive electrodes and the proof-mass, it is needed to apply about 1000 volts on the upper electrodes to levitate the proof-mass. For a gap of 300 µm as for the ultra-sensitive axes, a voltage of 100 000 volts will be necessary.

When the proof-mass is heavier, it is no more possible to levitate, as the electric field needed to levitate is above the Paschen limit, causing the creation of electric arc between the proof-mass and the electrodes. It is for example the case for the Microscrope accelerometer designed by ONERA, the MAC accelerometer, or the LISA inertial sensor, which are not levitated on ground (for LISA, the proof-mass is suspended with a thin wire of tungsten). For Microscope accelerometer and MAC accelerometer, only free-fall in the Zarm drop tower will be done to verify the functioning of the accelerometer.

Such a choice could be done for the next NGGM accelerometers, if it is decided to limit to have only one accelerometer by spacecraft. Nevertheless, we shall be conscious that the ground levitation allows a better verification of the accelerometer:

- the cleanliness of the accelerometer core can be verified by the verification of the stiffness (for GOCE accelerometer ,the first models have been dismounted after the verification of the presence of a parasitic stiffness);
- the differential scale factor and quadratic factor can be estimated on ground on the anti-seismic pendulum (for GOCE accelerometers, the estimation of the quadratic factor shows a greater value than expected),

5.1.5.3. Gold wire or not

The low-frequency noise is mainly due to the damping of the gold wire, if the thermal drift of the bias is not taken into account. This gold wire seems a intrinsic limitation for the low-frequency noise. In order to decrease its contribution, a thinner or longer gold wire could be chosen, but the current diameter of 5 µm is already very thin. It also possible to increase the mass of the proof-mass. But it implies to use a caging mechanism to block the proof-mass during the launch, as on LISA or Microscope accelerometers.

If the gold wire is suppressed, the charge of the proof-mass shall be controlled in-flight: in MAC accelerometer, it was chosen to hit regularly the stops, in LISA accelerometer, a UV discharge system is used. The gold wire is also used to polarise the proof-mass with the detection (at 100k Hz) and the polarisation voltage. In LISA, injection electrodes are used to play this role.

Taking into account the level of noise required by the NGGM, it doesn't seem useful to suppress the gold wire.

5.1.5.4. Angular acceleration

With the current configuration of the GRADIO accelerometer, the angular acceleration is correctly measured only around the less-sensitive axis. To measure it around another axis, it is necessary to have a cubic proof-mass, as in MAC, MicroSTAR or LISA accelerometers. For these accelerometers, the electrode configuration is 2 electrodes in regards of each face of the proof-mass. This configuration is not compliant with a ground levitation: the ground levitation necessitates to control not only the vertical motion, but also the rotation around the horizontal axes which are sensitive to the presence of 1 g on ground. Consequently, with the configuration with 2 electrodes pairs by axis, only one axis could be ultra-sensitive if the ground levitation is required.

It is also possible to keep the GRADIO configuration of electrodes (less-sensitive electrodes on the upper and lower ULE plates to control the vertical motion and the angular motion around horizontal axis), but with an increase of the height of the ring plate, in order to have a cubic proof-mass. In Figure 53, two ring-plates are used to increase the height. It is not sufficient for having a cubic proof-mass and the height of the ring-plates shall be also increased. With a cubic proof-mass and the same dimension of the electrode cage, the material of the proof-mass shall be changed in order to limit the weight and allow a ground levitation. With this new configuration, it is also possible to imagine a way to use the electrodes along the ultra-sensitive axes to control the angular acceleration around the horizontal axes without suppressing the possibility of levitate on ground. This new configuration shall be deeply analysed to evaluate correctly the cost of such modification, in terms of performance or realisation.

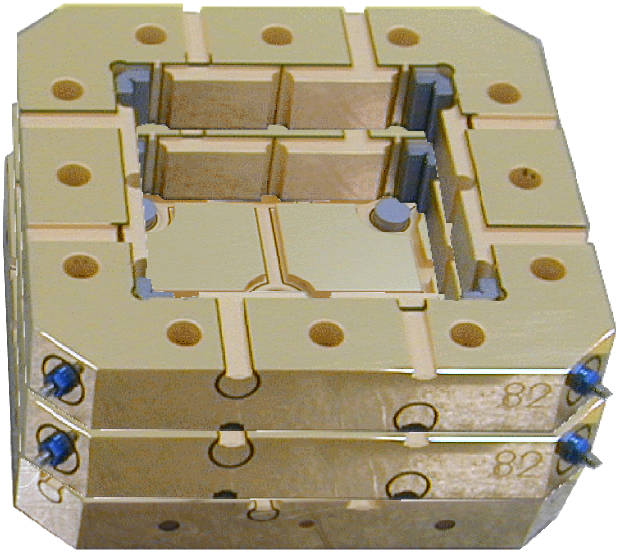

Figure 53: New concept of accelerometer with GRADIO heritage and cubic proof-mass

5.1.5.5. One or several accelerometers

With respect to the NGGM requirements, the solution with only one accelerometer implies some modifications of the GRADIO configuration:

- cubic proof-mass in order to have an angular acceleration measurement for the 3 angular motion,
- no ground levitation to have 3 ultra-sensitive axes.

Moreover, with only one accelerometer, the calibration of the scale factor or the misalignment is more difficult. It is necessary to find a external reference of linear acceleration. With several accelerometers, it is possible to calibrate the common scale factor of the linear acceleration measurement with the comparison with the star tracker by using the differential measurement as in the GOCE mission.

Finally, a solution with several accelerometers gives some redundancy in case of failure of one accelerometer and allows to have a gradiometer measurement in direction orthogonal to the in-line axis between spacecrafts which can be useful with respect to the aliasing problem of he GRACE-type measurement.

5.2. Recommended Reference Payload of the NGGM

Taking into the different trade-offs presented in the previous section, it appears that the solution with the highest level of technological readiness is with several accelerometers and the capability to levitate on-ground.

The proposed concept by Thales Alenia Space and ONERA is presented in Figure 54.

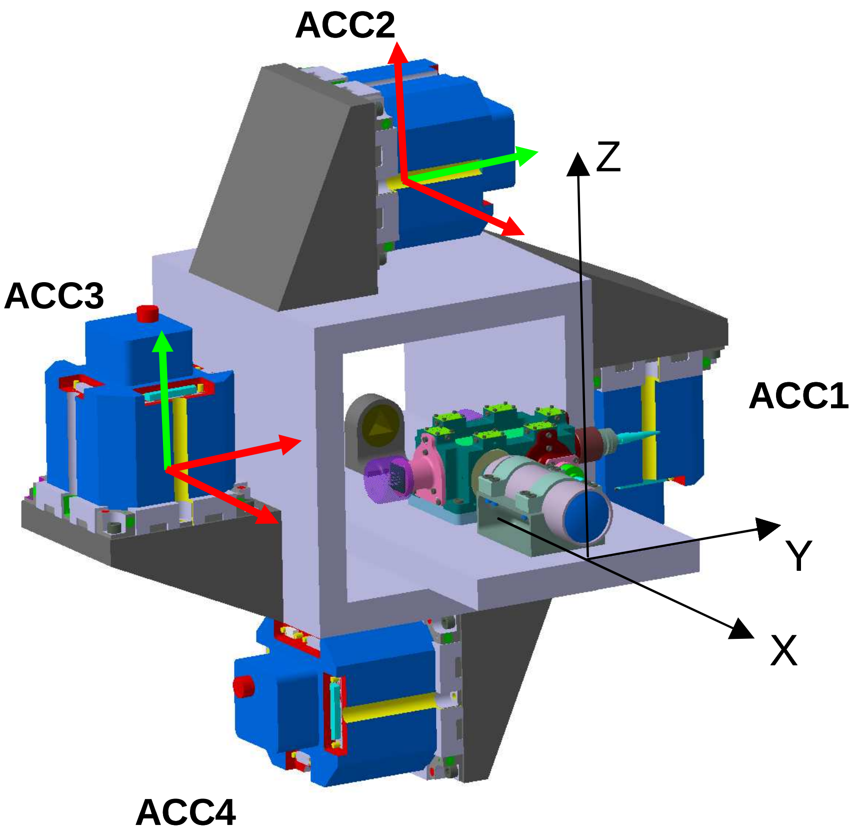

Figure 54: Concept of NGGM acceleration instrument with 4 accelerometers around the distance measurement instrument

5.2.1. Linear acceleration noise

The linear accelerations along the 3 axes are given by different combinations of the accelerometers ultra-sensitive outputs:

$$\begin{cases} a_X = \frac{1}{4}(a_{X1} + a_{X2} + a_{X3} + a_{X4}) \\ a_Y = \frac{1}{2}(a_{Y1} + a_{Y3}) \\ a_Z = \frac{1}{2}(a_{Z2} + a_{Z4}) \end{cases}$$

The level of noise of an ultra-sensitive axis is deduced from the one of GRADIO accelerometer with an improvement of the temperature stability (detailed in §5.2.3) and is presented in Figure 55. From this level of noise for one accelerometer, it is possible to deduce the level of noise for the global acceleration instrument, taking into account the previous combination. The level of noise for the 3 axes is presented in Figure 56. For the cross-track and radial axes, the level of noise is largely better than the requirements.

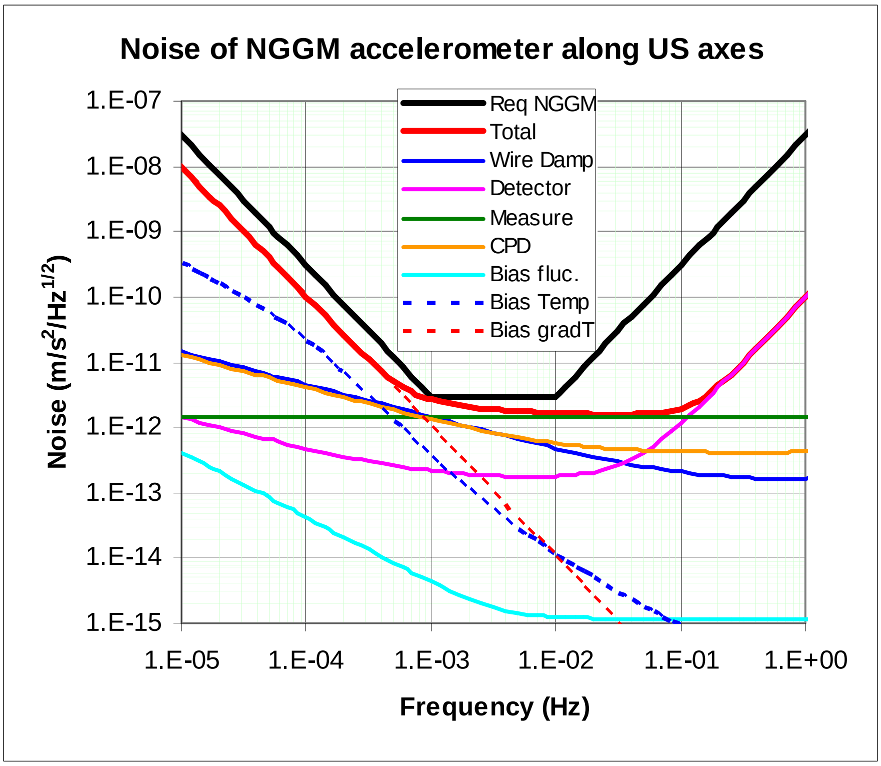

Figure 55: Ultra-sensitive axis linear acceleration noise for NGGM accelerometers

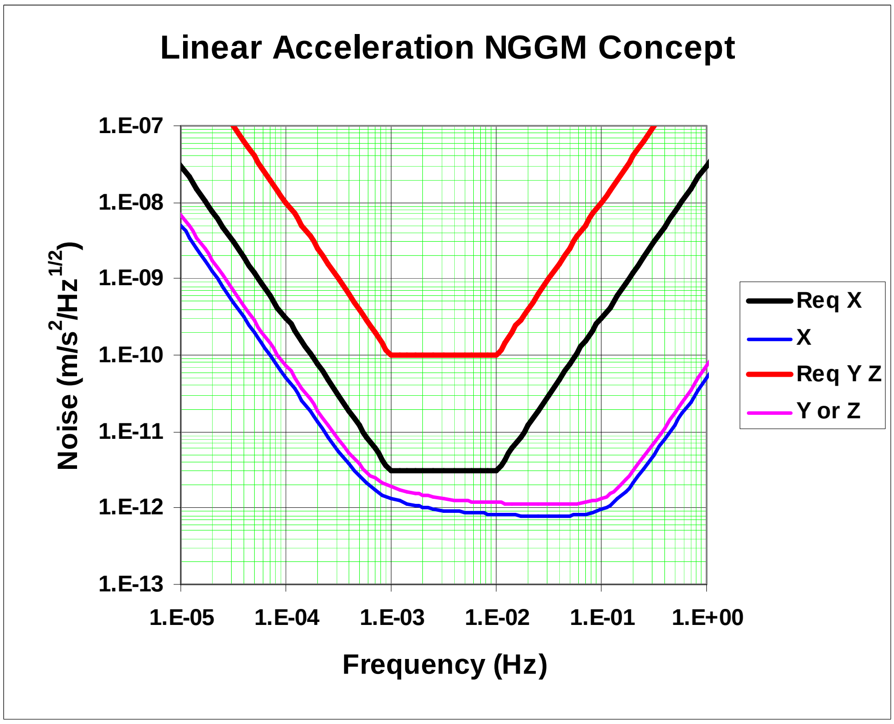

Figure 56: Linear acceleration noise for NGGM acceleration instrument

In case of failure of one accelerometer, it is possible to use the less-sensitive axis of the two accelerometers along the other direction to obtain the linear acceleration, but with a slightly degraded noise.

Figure 57 presents the level of noise for NGGM accelerometer along the less-sensitive axis deduced from the GRADIO performance with the following improvement:

- improvement of the temperature stability,
- use of analog loop for this axis only (in order to suppress the noise due to ADC1),
- decrease of the measurement range in order to decrease the level of the measure noise.

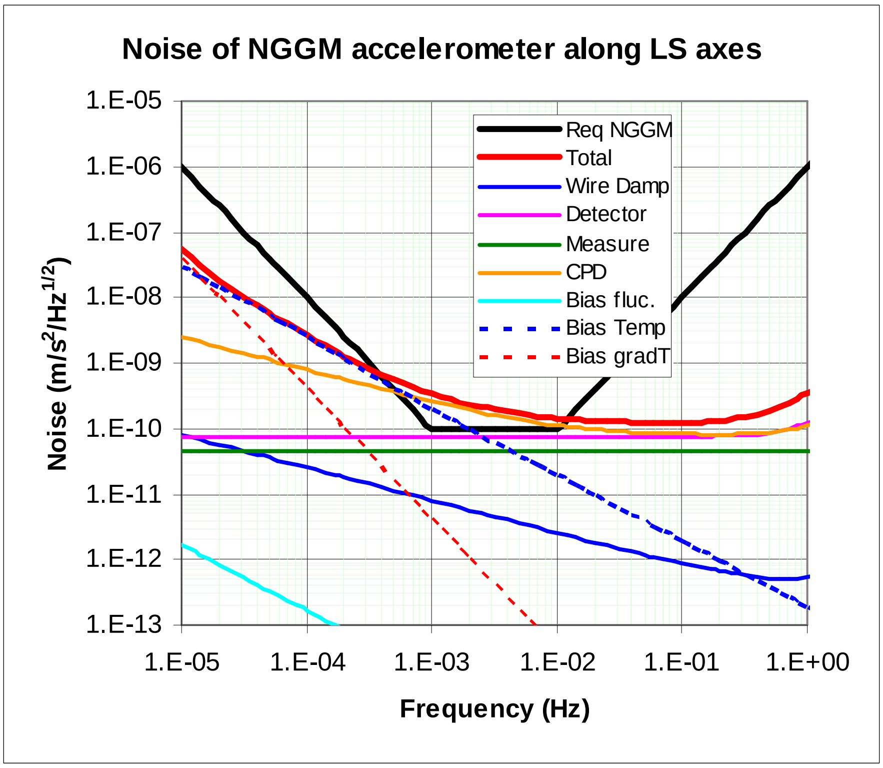

Figure 57: Noise of the NGGM accelerometer along less-sensitive axis

The main contributor of the less-sensitive axis is now the contact potential difference. Further analysis and new experiments shall be necessary to have a better assessment on this noise.

5.2.2. Angular acceleration noise

From the differential accelerations, it is possible to deduce the angular acceleration around the 3 axes:

$$\dot{\omega}_X = -\frac{a_{d,24,Y}}{L_Z} + \frac{a_{d,13,Z}}{L_Y}$$

$$\dot{\omega}_Y = 2\frac{a_{d,24,X}}{L_Z} + U_{XZ} - \omega_X \omega_Z$$

$$\dot{\omega}_Z = -2\frac{a_{d,13,X}}{L_Y} - U_{XY} + \omega_X \omega_Y$$

But, only the angular acceleration measurement around the along-track axis is directly usable. For the 3 other angular acceleration measurement, the measures shall be corrected from the gravity gradient and from the centrifugal acceleration.

It is why it is proposed to use the angular acceleration deduced from angular outputs of the accelerometer around the less-sensitive axis:

$$\dot{\omega}_Y = \dot{\omega}'_{c,13,Y}$$

$$\dot{\omega}_Z = \dot{\omega}'_{c,24,Z}$$

The angular acceleration noise around the less-sensitive axis of the proposed NGGM accelerometer is presented in Figure 58. It is deduced from the GRADIO level of noise with the improvement of the temperature stability.

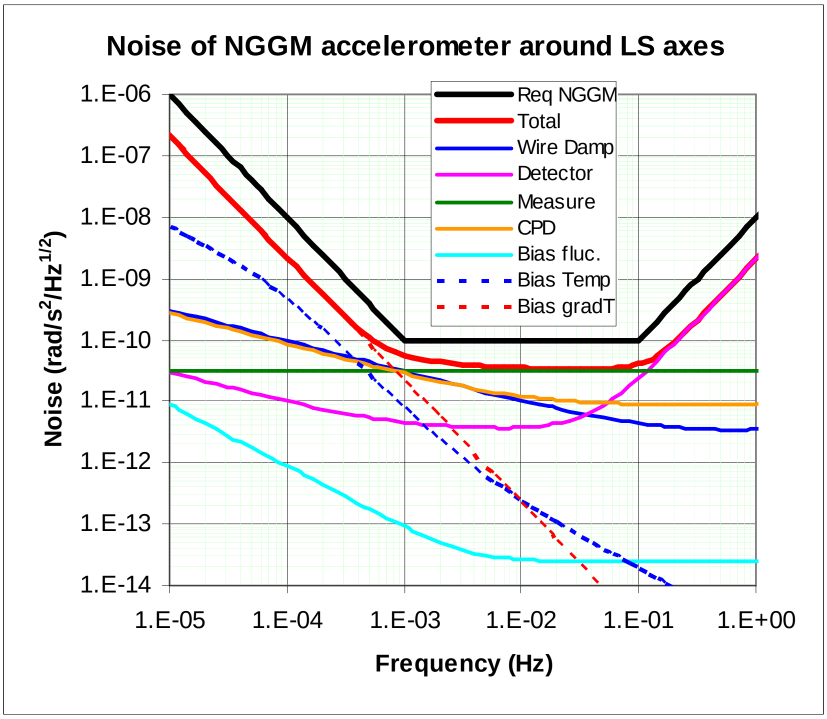

Figure 58: Noise of the angular acceleration around the less-sensitive axis for the NGGM accelerometer

From the level of noise of the linear acceleration along the less-sensitive axis and of the angular acceleration around the less-sensitive axis, the level of angular acceleration noise of the global acceleration instrument for NGGM is deduced and showed in Figure 59.

The requirement is achieved for the angular acceleration around the cross-track and the radial, but not around the along-track axis. The discrepancy is a factor 6.7 at 1 mHz and a factor 2.4 at 100 mHz. The only way to improve the performance will be to suppress the less-sensitive axis, and so to suppress the capability to test the accelerometer on ground.

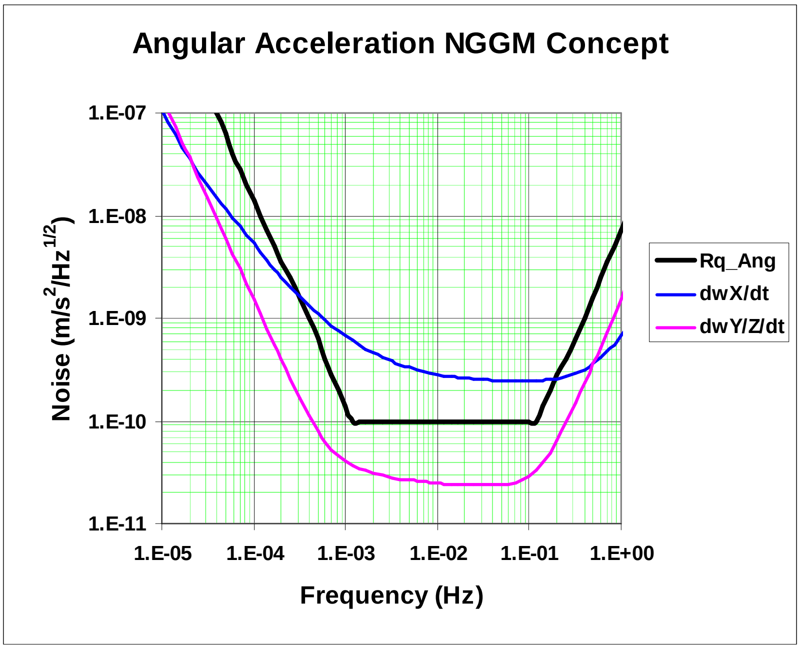

Figure 59: Noise of the angular acceleration for the NGGM acceleration instrument

5.2.3. Scale factor noise

Figure 60 presents the scale factor noise along the ultra-sensitive axis for the NGGM accelerometer. The contributors are deduced from those of GRADIO accelerometer, with some improvements for the temperature stability and for the noise of the reference voltage of the ADC2.

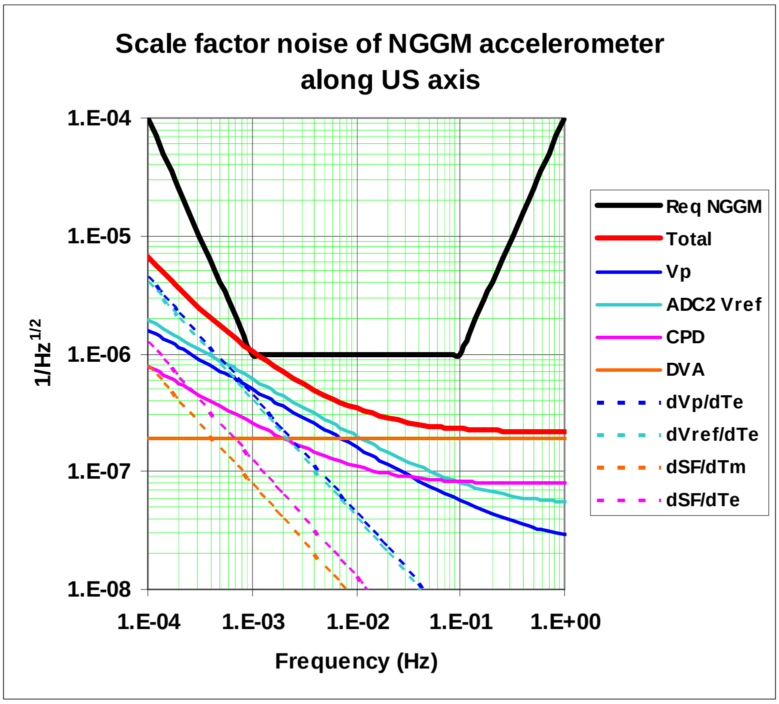

Figure 60: Scale factor noise along the ultra-sensitive axis of the NGGM accelerometer

5.2.4. *Bias and range*

The biases along the 3 spacecraft axes are the ones of the ultra-sensitive axis, 1.2 10^{-7} m/s^2.
The measurement range along the ultra-sensitive axis is 6.3 10^{-6} m/s^2, with a controlled range along the same axis is 3.1 10^{-5} m/s^2.

5.2.5. *Temperature stability requirements*

The temperature stability requirements are deduced from the required level of linear acceleration noise (for the ASH temperature) and scale factor noise (for the FEEU temperature):

- The temperature of the ASH shall be stable with a level of: $T = 40\,mK/\sqrt{Hz} \times \frac{1mHz}{f}$;
- The temperature gradient of the ASH shall have a stability of $T = 4\,mK/\sqrt{Hz} \times \frac{1mHz}{f}$;
- The temperature of the FEEU shall have a stability of $T = 40\,mK/\sqrt{Hz} \times \frac{1mHz}{f}$.

5.2.6. *Mass and power consumption budgets*

For the mass and power consumption of the acceleration instrument, two different hypotheses have been considered, one with an analog control loop, like in GRACE mission, one with a digital control loop, like in GOCE mission. In case of SuperSTAR accelerometer of the GRACE mission, the front-end electronics is fixed around the mechanical sensor.

Table 1 presents the mass budget and Table 2 the power consumption for the both hypotheses. the mass and power consumption are the ones of the SuperSTAR and GRADIO accelerometers.

Table 1: Mass of the NGGM acceleration instrument

	Analog control loop		Digitial control loop	
ASH	7.6 kg x 4 =	30.4 kg	5.2 kg x 4 =	20.8 kg
FEEU			6.3 kg x 2 =	12.6 kg
GAIEU/ICU	3.7 kg x 4 =	14.8 kg	6.6 kg x 1 =	6.6 kg
Total		**45.2 kg**		**40.0 kg**

Table 2: Power consumption of the NGGM acceleration instrument

	Analog control loop		Digitial control loop	
FEEU	2.1 W x 4 =	8.4 W	15 W x 2 =	30.0 W
GAIEU/ICU	7.1 W x 4 =	28.4 W	16.5 W x 1 =	33.0 W
Total		**36.8 W**		**63.0 W**

For the interface control (ICU) of the analog control loop, the budget is based on the ICU of the GRACE accelerometer which supply only one accelerometer. It should be possible to reduce the weight and power consumption with common functions, like for the DC/DC converters and an unique unit.

For the GAIEU of the digital control loop, the budget corresponds to the one of the GOCE mission where the GAIEU supplies 6 accelerometers. It should be possible to reduce a little the budget.

The advantages of the analog control loop are the lower power consumption and the lower level of noise. The advantages of the digital control loop are the flexibility of the definition of the parameters of the control loop, the capability of reconfigure the detectors and the possibility to calibrate and correct the quadratic factor easily.

6. REFERENCE INSTRUMENT CALIBRATION APPROACH

The differential scale factor of the accelerometers can be calibrated through the comparison of the accelerometer outputs when the spacecraft is shacked along the 3 axes. In order to not be sensitive to the uncertainty on the thrusters, it is possible to control the shake with common acceleration outputs of the accelerometers. In that case, the calibration gives the ratio of the differential scale factor with respect to the common scale factor.

For the calibration of the common scale factor, it is necessary to have an external reference. It could be given by the star tracker which can be calibrated on-ground. In that case, the differential linear accelerations presented in §5.2.2 are compared to the star tracker measurement during a shake of the spacecraft around its 3 axes. At the same time, it is possible also to calibrate the common scale factor of angular outputs of the accelerometer with comparison with the star tracker and the differential scale factor of the angular outputs by comparison between the accelerometers.

It is also possible to use the distance measurement instrument as an external reference of the linear motion of the spacecraft along the inline axis.

The common and differential misalignments of the linear acceleration outputs could be calibrated during the shake of the spacecraft along and around its axes.

7. MATHEMATICAL MODEL OF THE ACCELEROMETER

[To be completed]

8. ANNEX 1 : BIAS CALIBRATION

A good performance in low-frequency could be obtained either with an absolute accelerometer, as it is promised by the atomic interferometer accelerometer, or by calibrating the bias in orbit. Indeed, the low-frequency noise of an accelerometer is often related to a drift of the bias. By calibrating regularly this bias, it is possible to improve the performance at low frequency.

It is for example done on the Shuttle with the accelerometer OARE. It is a 3 axis electrostatic accelerometers, with a cylindrical proof-mass with a disc at its middle (see Figure 61, on the left). Electrodes inside the cylinder control the translation and rotation perpendicular to the cylinder axis and annular electrodes in regards of the disc control the translation along the cylinder axis. As the proof-mass is not connected, its charge varies in orbit and a bias calibration system is associated to the accelerometer. It is a double gimbals which allows by turning regularly the accelerometer to calibrate the bias (see Figure 61, on the right).

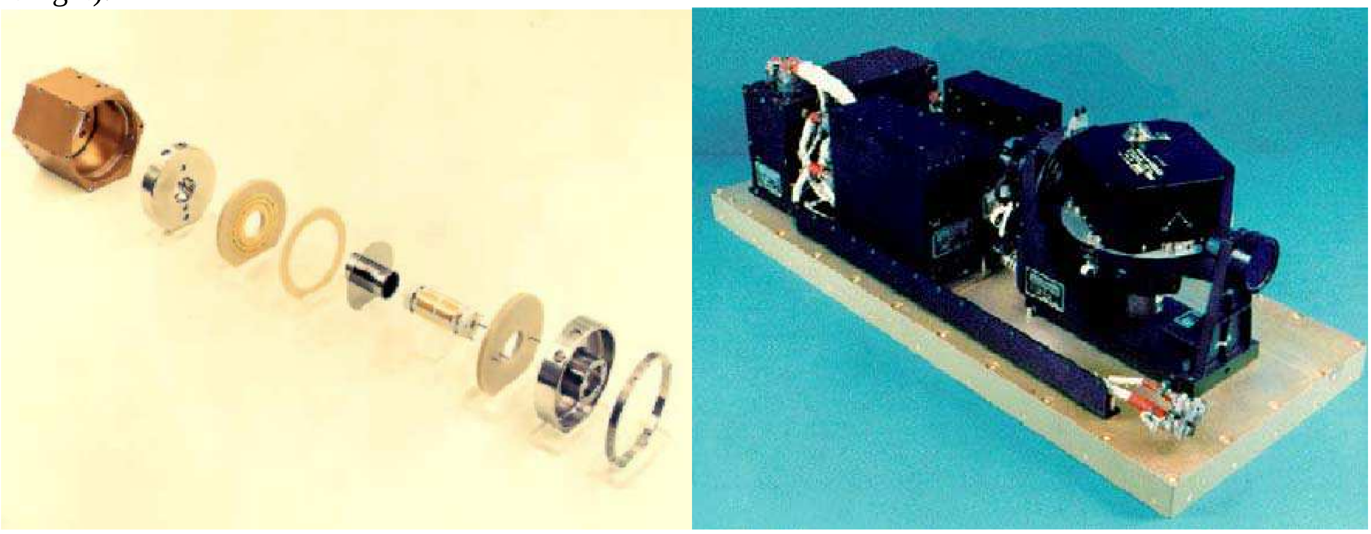

Figure 61: Accelerometer OARE on the Shuttle : exploded view on left and bias calibration system on right

The principle of the bias calibration is simple and can be described by Figure 62. With a turn of 180° of the accelerometer, it is possible to disentangle the external acceleration, independent of the orientation of the accelerometer, from the accelerometer bias, linked to the accelerometer reference frame.

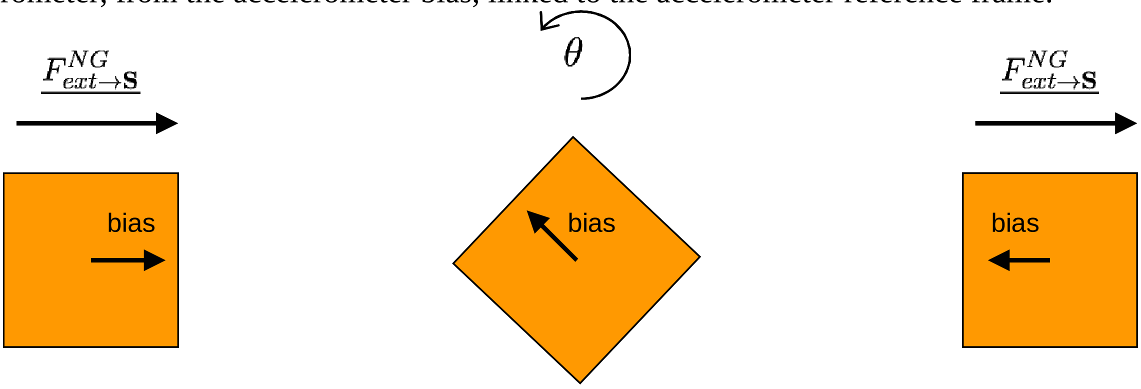

Figure 62: Principle of the bias calibration

Evidently, it is not possible by this method to distinguish between the drag and the spacecraft self-gravity for example. But the main contributors of the bias being due to the accelerometer itself can be calibrated.

In practice, for one rotation around the axis z, it is possible to calibrate the bias of the linear acceleration measurement along the axes y and z. The equations of measurements are presented in Figure 63: for N instants of measurement, there is 2N measurements, and 4 N unknowns, the 2N values of the external acceleration and the 2N bias along each direction. The choice of a modulation signal θ allows to orthogonalise the bias and the external acceleration and to access, by demodulation or average to each of them.

$$\boxed{m_x} = \boxed{n_x} + (1+\delta k_x)\left[\mu\left(\boxed{F_x^{NG}}\cos(\theta) + \boxed{F_y^{NG}}\sin(\theta)\right) + F_x^{gold}\right] + b_x$$

$$\boxed{m_y} = \boxed{n_y} + (1+\delta k_y)\left[\mu\left(-\boxed{F_x^{NG}}\sin(\theta) + \boxed{F_y^{NG}}\cos(\theta)\right) + F_x^{gold}\right] + b_y$$

Measures Noise

Bias:

electronic + gold wire

2N measures

4N unknowns

Figure 63: Equation of measurements of the acceleration outputs in the plane perpendicular to the rotation axis

This principle has been verified at ONERA by simulation on an interplanetary trajectory towards Jupiter for Jupiter Ganymede Orbiter (Figure 64)..

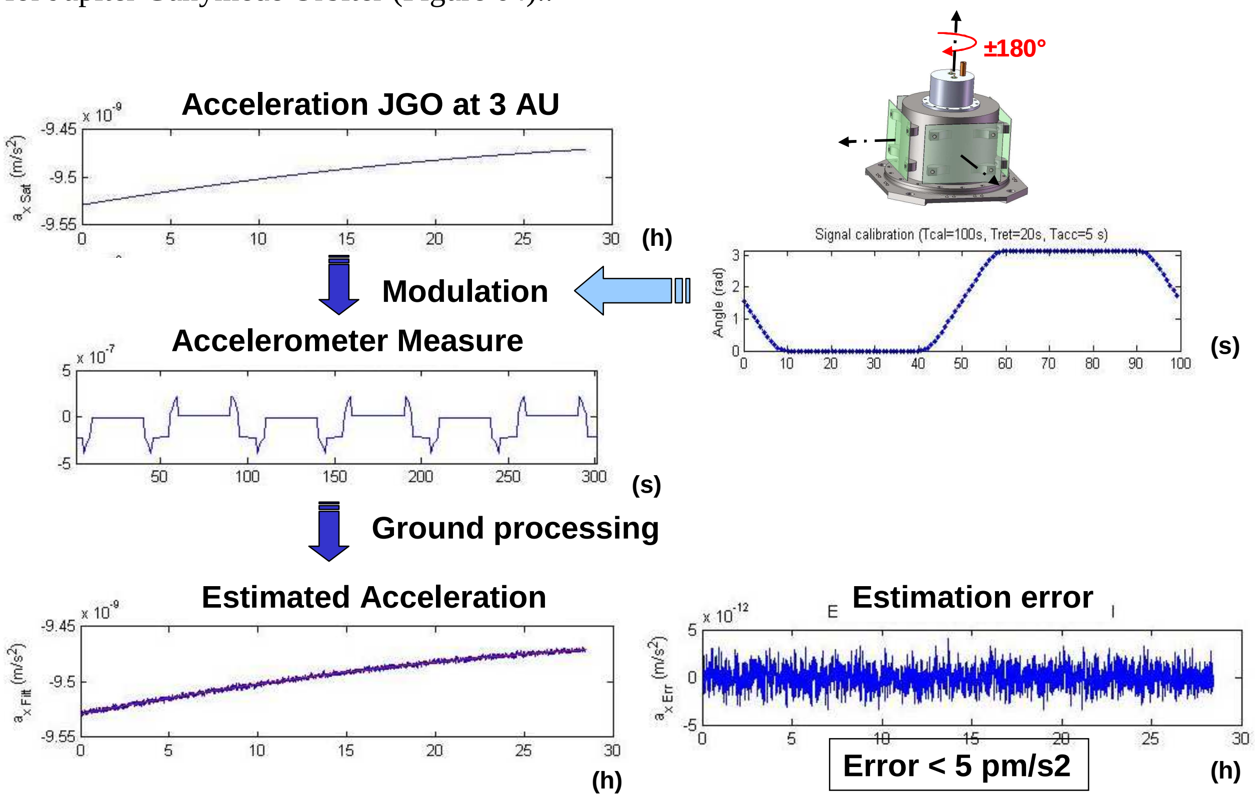

Figure 64: Verification of the bias calibration principle by simulation

The modulation signal was a square signal with a period of 100 s. An off-centring of the accelerometer with respect to the rotation axis has been added, explaining the peak at each turn. Nevertheless, it was possible to estimate the external acceleration with accuracy better than 5 10^{-12} m/s^2, despite a bias of about 10^{-6} m/s^2.

This principle has also been verified experimentally, with a Q-Flex accelerometer and Newport rotating stage (Figure 65).

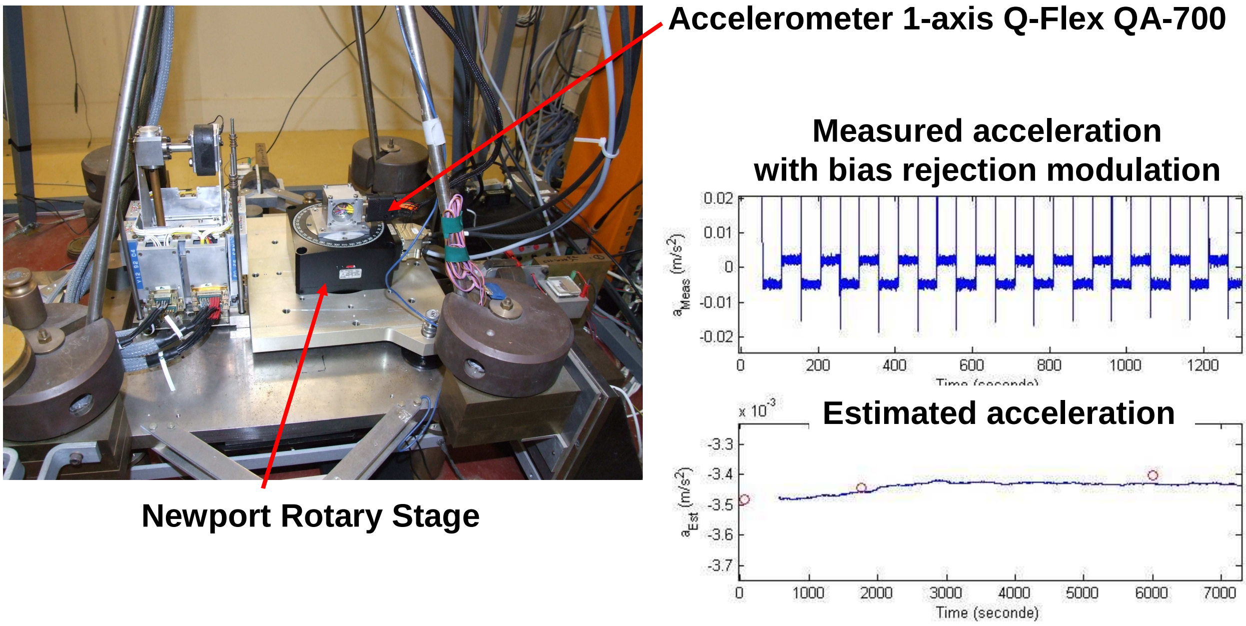

Figure 65: On-ground verification of the bias calibration principle : setup on the left and measured and estimated acceleration on the right

Due to the quick rotation of the Newport stage, the measured acceleration has an huge peak at each turn. Nevertheless, it was possible to process the data, thanks to a masking method and to retrieve an estimation of the external acceleration (due to the projection of the gravity). The red circle presents the estimation by comparing only one period of turn (difference of measurement at 0° and 180°) and the blue curve presents a frequential method, where the measurement is demodulated at the frequency of the calibration signal.

9. ANNEX 2: TEMPERATURE ANALYSIS

9.1. Temperature sensitivity of the GRADIO accelerometer

The impact of the temperature stability in the accelerometer outputs is linked to different parameters:

- the temperature stability at the interface of the accelerometer,
- the time response of the accelerometer,
- the thermal sensitivity of the accelerometer.

Figure 66 presents for the GRADIO accelerometer of the GOCE mission the thermal stability at the interface of the accelerometer (temperature at FEEU interface, temperature at ASH interface and temperature gradient at ASH interface), the thermal stability inside the FEEU and ASH deduced from the one at interface thanks to the time response of the mechanical parts (30 mn for the electrode plates and 41 h for the proof-mass).

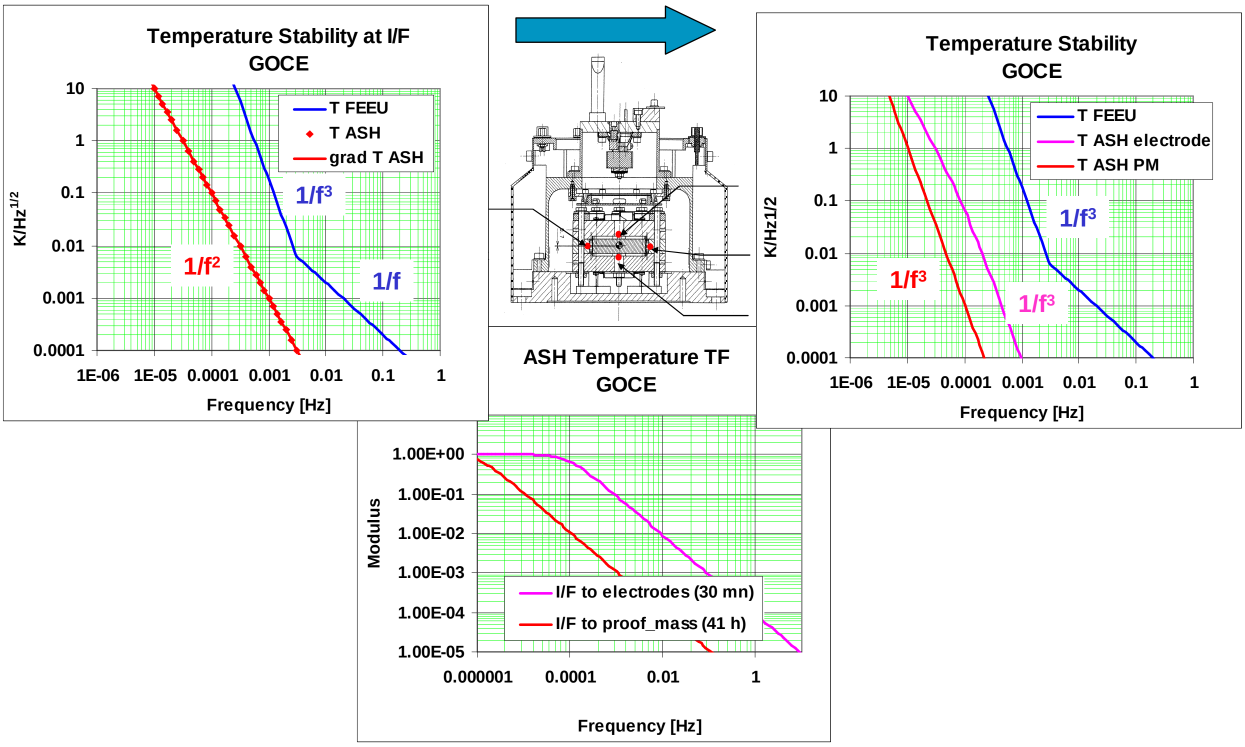

Figure 66: Temperature stability at interface (left top) and inside the accelerometer core (right top) with the corresponding transfer functions (middle bottom)

The effect of these temperature stabilities on the bias thermal drift is presented in Figure 67 for the temperature stability around the mechanical sensor (ASH) and in Figure 68 for the temperature stability around the electronics unit (FEEU). The main contributor is the radiometer effect due to the gradient of temperature between opposite faces of the proof-mass, but it appears also that the temperature stability of the electronics has a great part in the global stability at low frequency : it comes from the thermal stability of the detector bias or the readout bias, but also by the coupling of some mechanical parameters (like the dissymmetry of the electrode surface or the contact potential difference) with the thermal sensitivity of the applied voltages on the proof-mass or the electrodes.

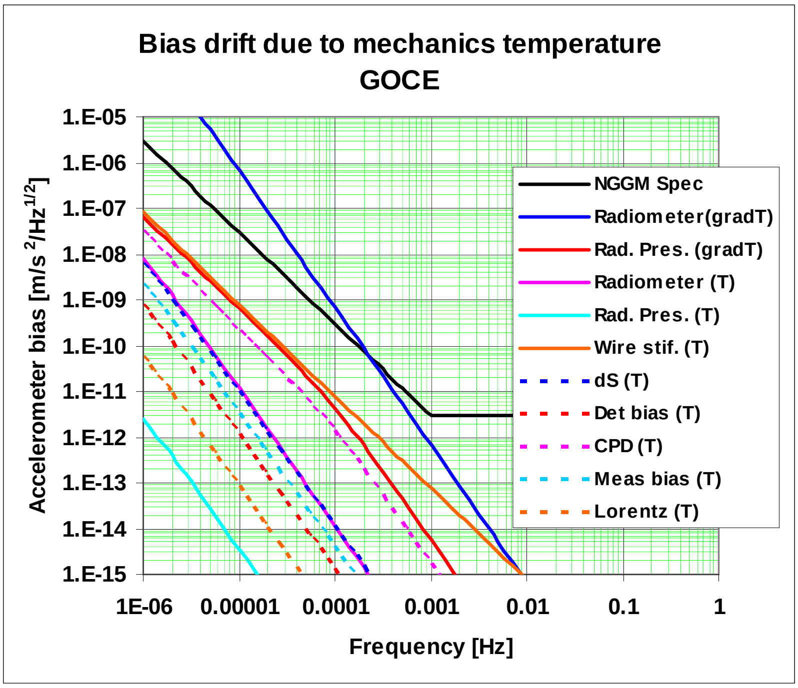

Figure 67: Bias thermal drift due to the mechanics temperature of the GRADIO accelerometer on GOCE mission, along the ultra-sensitive axis

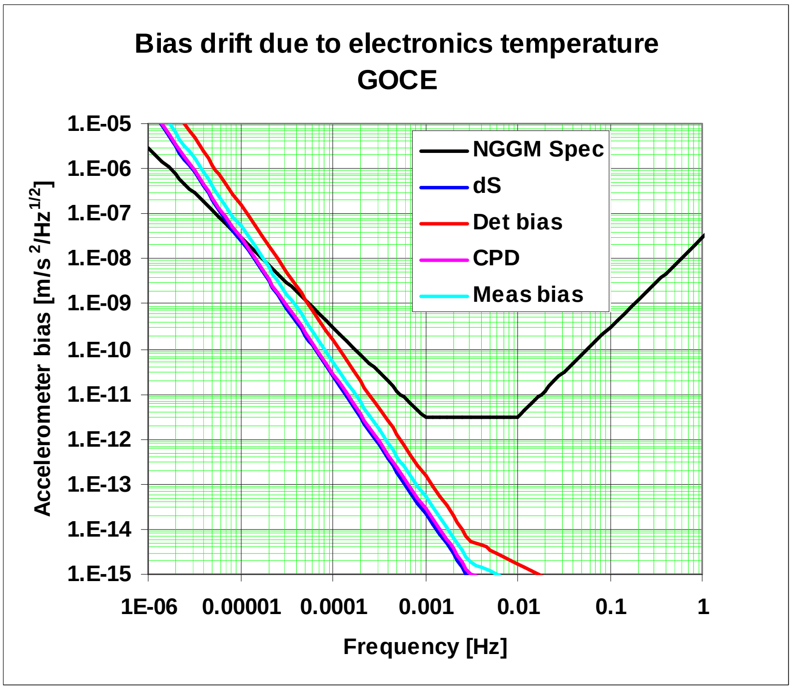

Figure 68: Bias thermal drift due to the electronics temperature stability of the GRADIO accelerometer of the GOCE mission, along the ultra-sensitive axis

9.2. In-flight measured temperature in GOCE mission

The house-keeping data of the GOCE mission includes the monitoring temperature around the gradiometer canister and inside the electronics.

Figure 69 presents the evolution of the monitoring temperature of the gradiometer canister in October 2009.

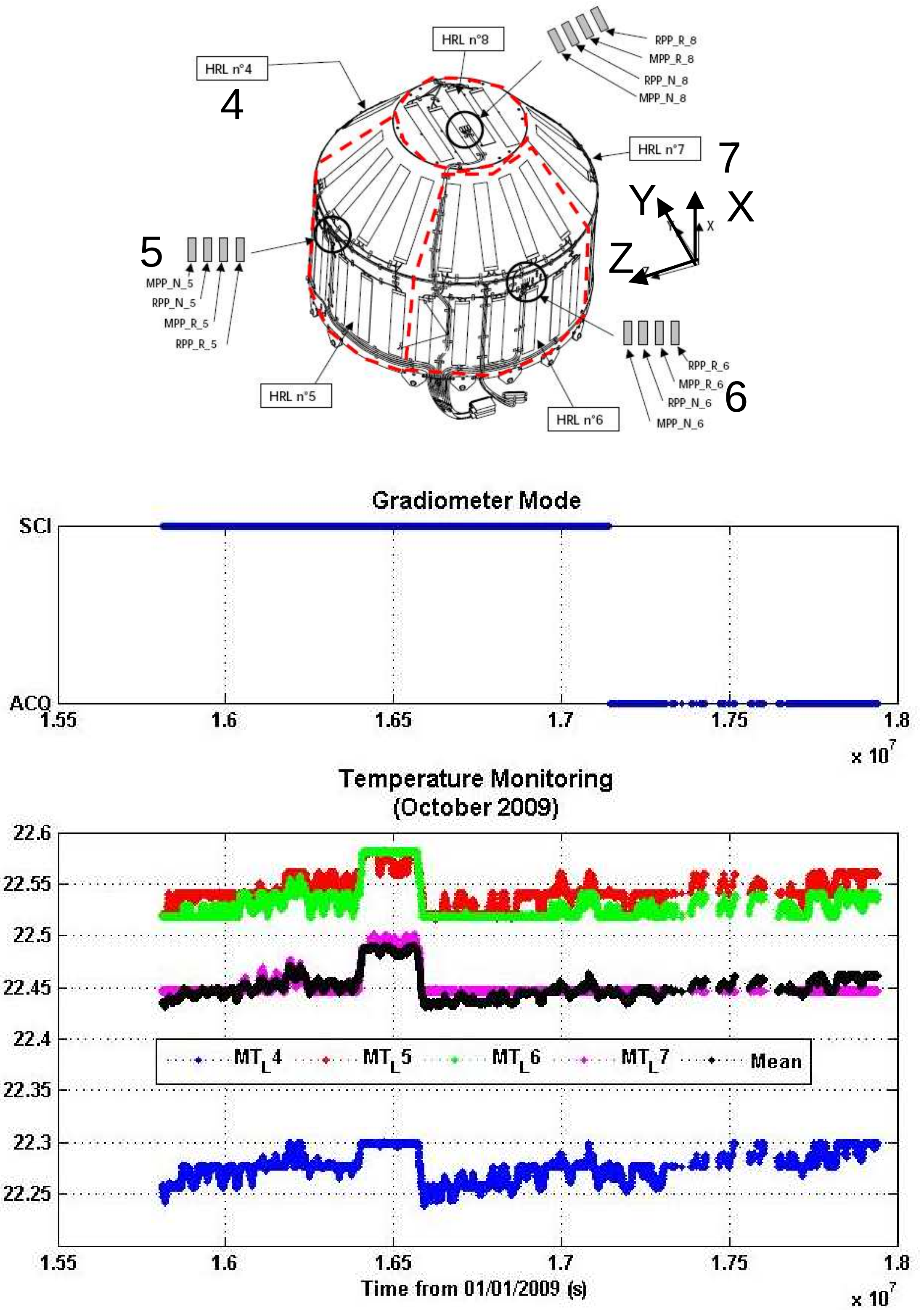

Figure 69: Localisation of the monitoring temperature sensors on the gradiometer canister (top), the gradiometer mode (middle) and the evolution of the temperature (bottom)

Figure 70 presents the deduced spectral density of the mean temperature at the centre of the gradiometer canister, computed as the mean of the 4 temperature sensors located at the periphery of the canister. It is compared to the specification at the ASH interface. It is important to note that between the external face of the canister and the interface with the ASH, it is necessary to take into account a transfer function which is not known but will improve the temperature stability at ASH interface. Above 10 mHz, the level of noise is due to the monitoring noise.

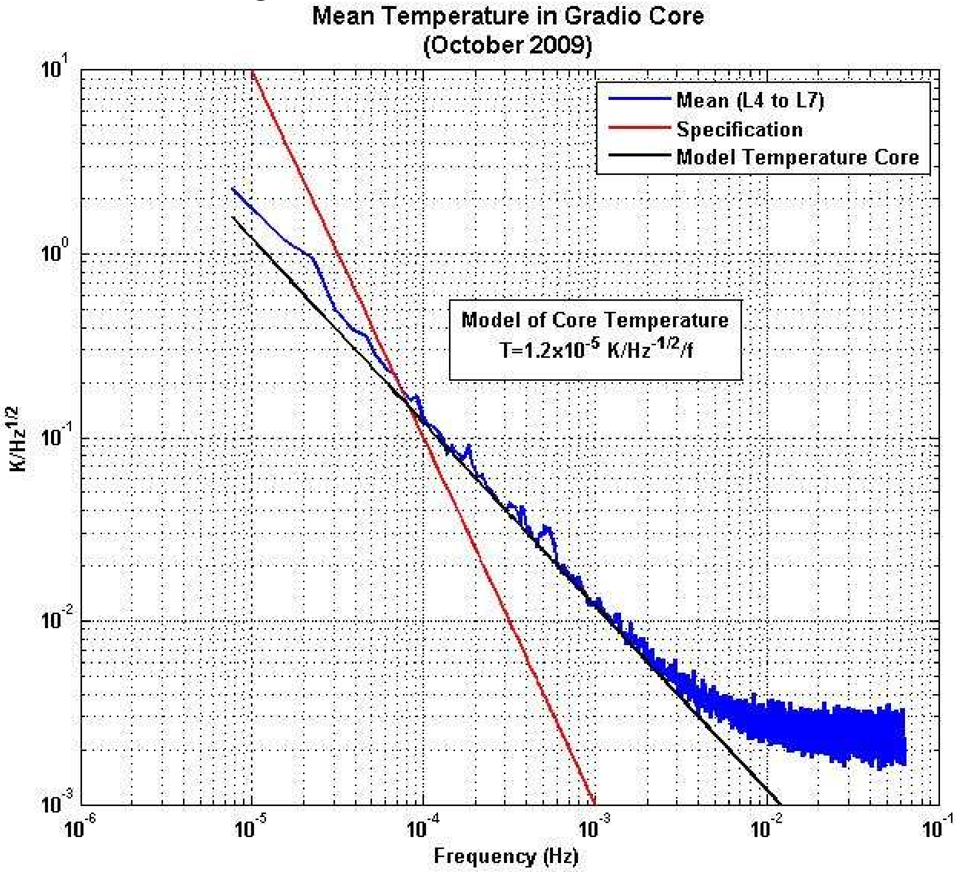

Figure 70: spectral density of the mean temperature of the canister in October 2009 (blue), with respect to the specified temperature stability at AH interface (red)

Nevertheless, it appears that the temperature stability in 1/f with a better stability at low frequency. At 1 mHz, the level is 12 mK/Hz$^{1/2}$. It could be interesting to perform such analysis on a longer period and to try to deduce the transfer function between temperature sensor and ASH interface.

Figure 71 presents the evolution of the temperature monitoring inside the FEEU 1+ for the detector boards (containing the detector, action and measurement functions) and the controller board (containing the generation of the detection and polarisation voltages). The limited accuracy of the ADC for monitoring explains the quantified level of the temperature.

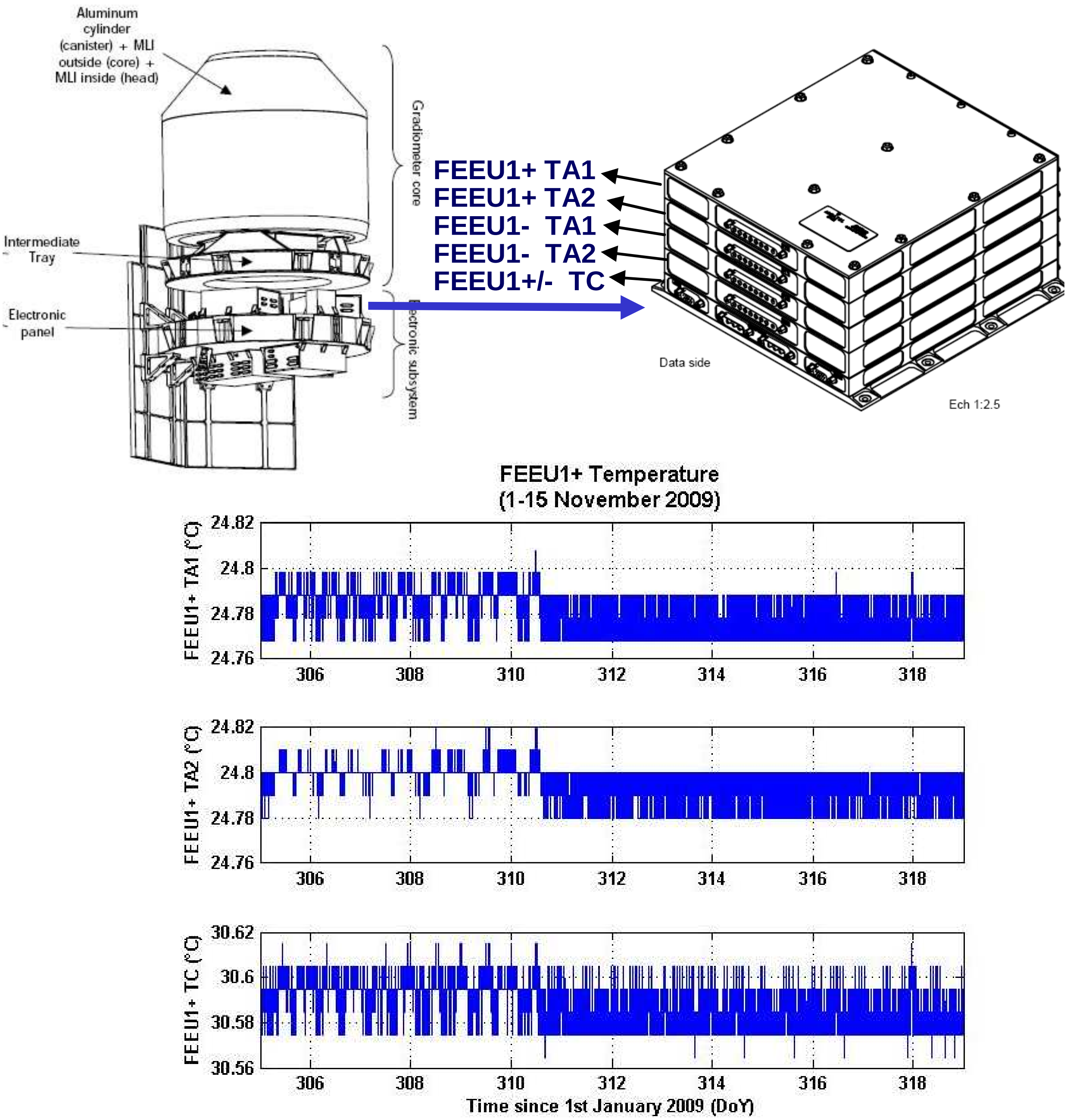

Figure 71: Localisation of the temperature sensor inside the FEEU (top) and evolution of the temperature for the semi-FEEU 1+, for the first detector board (TA1) the second detector board (TA2) and the controller board (TC)

Figure 72 presents the spectral density of the monitoring temperatures. The level above 2 mHz is due to the bad monitoring of the temperature. Nevertheless, it appears clearly that the temperature stability is better than the specification at low frequency, with a slope in 1/f. Some harmonics at the orbital frequency and its multiple are present. An analysis on a longer period would be interesting, in particular to verify this low-frequency stability and the capability to measure the variation of the temperature (with the objective to correct this variation in the accelerometer outputs).

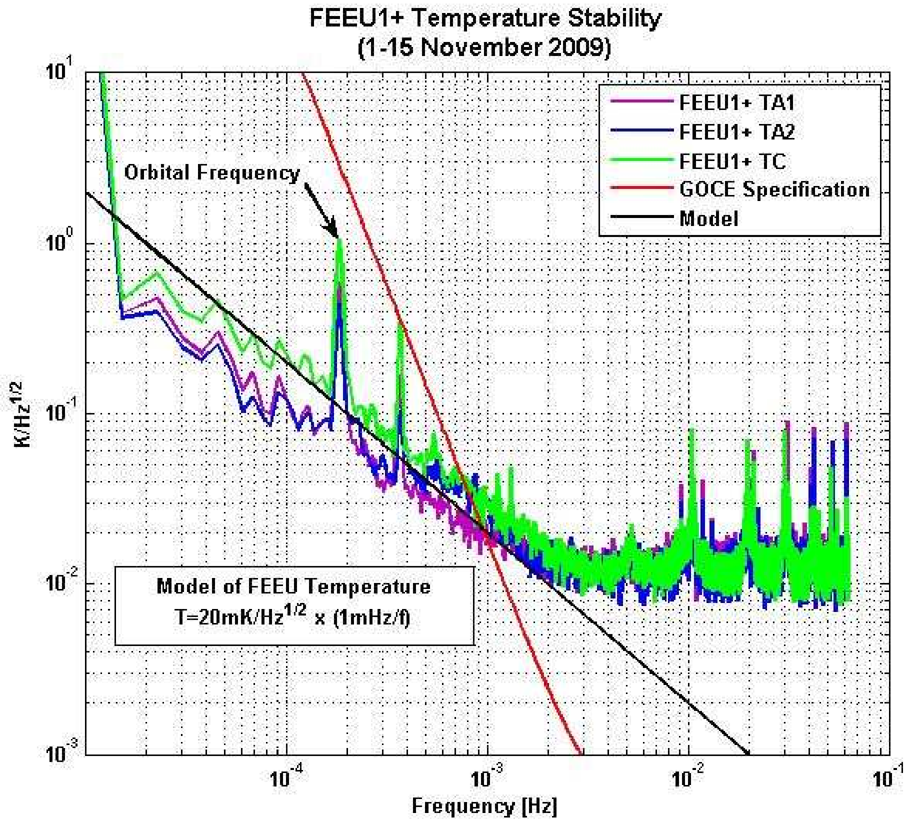

Figure 72: Spectral density of the FEEU temperature monitoring and comparison with the specification at the interface